UNIVERSITY OF CALIFORNIA
RIVERSIDE

Materials Development and Spin Transport Study of Magnetic Insulator Based Heterostructures

A Dissertation submitted in partial satisfaction
of the requirements for the degree of

Doctor of Philosophy

in

Physics

by

Chi Tang

March 2017

Dissertation Committee:
Dr. Jing Shi, Chairperson
Dr. Jory Yarmoff
Dr. Harry W. K. Tom

The Dissertation of Chi Tang is approved:

Committee Chairperson

University of California, Riverside

Acknowledgements

Pursuing Ph. D degree is a journey to self-actualization. No pains, no gains. At this moment, I am grateful to the life in UC Riverside that gives me a precious memory. The accomplishment of Ph. D is the most valuable and exciting moment for me.

I would like to express deep gratitude to my supervisor Prof. Jing Shi first for his guidance, encouragement and gracious support throughout the six years in my Ph. D study, for his expertise in the academic field that motivated me with great passion and for his valuable comments and suggestions to elevate myself from a graduate student to a polished scientific researcher. He also provides me endless help in my life and opportunities to enter dream institutions. Thank for you very much for the mentorship, Prof. Shi.

I also want to thank my committee members, Prof. Jory Yarmoff and Prof. Harry. W. K. Tom for their insightful comments and suggestions on my research projects. I would like to deeply thank Prof. Javier Garay and Prof. Roger Lake for their time being my oral committee members. Please also allow me to express my sincere appreciation to Glenda Barraza and Dorothea. Northcutt in SHINES center for their patience and generosity in helping me deal with numerous shipping, receiving, reimbursements and other matters to make the collaborative projects proceed smoothly. I would like to thank Derek Beving and all the other faculty members and staff in the Department of Physics and Astronomy at UC Riverside, for their support during my Ph. D research. I would also like to thank Dong Yan, Dexter Humphrey, Nissim Amos and other staff in the Center for Nanoscale Science and Engineering for the help with the nano fabrication.

I would like to sincerely acknowledge my labmates for their assistance, helpful discussions and precious friendship. They are Peng Wei, Xinfei Liu, Tao Lin, Ray Sachs, Zhiyong Wang, Hamad Alyahyaei, Zilong Jiang, Yadong Xu, Zhisheng Lin, Mohammed Aldosary, Bowen Yang, Junxue Li, Zhong Shi, Victor Ortiz, Yawen Liu, Mark Lohmann and Benjamin Madon. I would like to thank my colleagues Kyle Chan, Pathi Sellappan, Aleksey Volodchenkov, Chad Warren, Bin Cheng, Yong Wu, Cheng Pan, Peng Wang, Tengfei Miao, Weimin Zhou, Changtao Hou, Yi Wu, Yanmeng Shi, Shaolong Chen, Supeng Ge, Shanshan Su, Yizhou Liu and many other people that I cannot list all here in UCR for their kind help with my research projects and friendship.

Furthermore, I want to deeply thank Prof. Chia-Ling Chien and Danru Qu from JHU, Prof. Elaine Li and Xin Ma from UT Austin, Prof. Cui-zu Chang from PSU, Prof. Jagadeesh S. Moodera from MIT, Prof. Kang Wang, Guoqiang Yu and Qiming Shao from UCLA, Prof. Mingzhong Wu and Houcheng Chang from CSU, Prof. Tingyong Chen from ASU and all the other my collaborators from different research institutions for their support in the research and friendship in life.

Last but not least, I want to express my deep love and heartfelt gratitude to my parents Mr. Xianwen Tang, Mrs. Xueqin Zhang, my sister Miss Meng Zhang and my wife Mrs. Dan Gao for their love, trust, understanding and encouragement. Without the support from them, I cannot finish this big challenge in my life. Love you all!

ABSTRACT OF THE DISSERTATION

Materials Development and Spin Transport Study of Magnetic Insulator Based Heterostructures

by

Chi Tang

Doctor of Philosophy, Graduate Program in Physics
University of California, Riverside, March 2017
Dr. Jing Shi, Chairperson

The subfield of magnetic insulator (MI) based spintronics is playing a substantial role in modern solid state physics research. Spin current in the MI is propagated in spin wave with a much longer decay length than spin-polarized carriers in conducting ferromagnet. In the MI-based hetereostructures, the adjacent non-magnetic materials can be magnetized in proximity of MI. Therefore, it is a promising system to study exotic transport phenomena such as quantum Anomalous Hall effect in topological insulator and graphene. Rare-earth Iron garnet (ReIG), a class of magnetic insulators with large electronic bandgap and high Curie temperature, stands out among various magnetic insulator materials and have attracted a great deal of attention in recent magnetic insulator based spintronics research.

The first chapter of this dissertation gives a brief introduction to the spintronics research by introducing some essential concepts in the spintronics field and the most recent spin transport phenomena.

The second chapter of this dissertation summarizes my work in the materials development of ReIG ferrimagnetic insulators, including exquisite control of high quality ultra-flat yttrium iron garnet (YIG) thin films with extremely low magnetic damping and engineering of strain induced robust perpendicular magnetic anisotropy in thulium iron garnet (TIG) and Bi-doped YIG films.

The last chapter of this dissertation shows a systematic study in various ReIG based heterostructures, mainly divided into groups: ReIG (YIG & TIG)/heavy metal bilayers (Pd & Pt) and ReIG (YIG & TIG)/Dirac systems (graphene & topological insulator). The magneto-transport study disentangles the contribution from a spin current origin and proximity induced magnetism. Furthermore, the demonstration in the proximity coupling induced high-temperature ferromagnetic phase in low-dimensional Dirac systems, i.e. graphene and topological insulator surface states, provides new possibilities in the future spintronics applications. The modulation on the spin dynamics of magnetic insulator layer by topological insulator surface states is investigated at last, further confirming the superb properties of such magnetic insulator based spintronics systems.

Contents

List of Figures

List of Tables

Chapter 1

Introduction to Magnetic Insulator Based Spintronics

1.1. Spintronics Overview

The strong correlation between electron charge and spin triggers the blossom of condensed matter physics research especially in spintronics in the last two decades. Spintronics, or spin electronics, involves the interplay between the charge and spin degrees of freedom in various solid state systems(*1*, *2*). It emerged from the discoveries of spin-dependent electron transport phenomena in metals and semiconductors, which is not only of lasting fundamental physics research interest over time, but also has advanced the information technology such as low-power memory and high-speed, high-density disk-drives. The two degrees' freedom of electrons enable solid state devices to store and transmit info more efficiently.(*1*).

In analogy to charge current, spin current is defined as a flow of spin angular momentum. By creating non-equilibrium spatially varying spin population, a spin current can be generated by several means, including electrical and optical spin injection, ferromagnetic resonance and thermal excitation methods. In ferromagnetic metal or semiconductors, charge current drives spin-polarized electrons to generate spin current that transmits spin angular momentum. However, it is always accompanied by Joule heating which dissipates energy. An alternative way is to generate pure spin current in magnetic insulators without any charge current causing the dissipation of energy. Such a

pure spin current is carried by collective motion of magnetic moments coupled by dipolar or exchange interaction, namely spin waves, leading to a much longer propagation distance than spin-polarized charge current in metals and semiconductors(*3*).

Significant advances have been achieved during the past decade in the insulator-based spintronics, including novel strategies of spin current generation, manipulation, detection, and remarkable discoveries of proximity-induced magneto-transport phenomena in magnetic insulator-based heterostructures. In this chapter I will cover some basic background material and recently discovered phenomena in the field of magnetic insulator based spintronics.

1.2. Hall Family

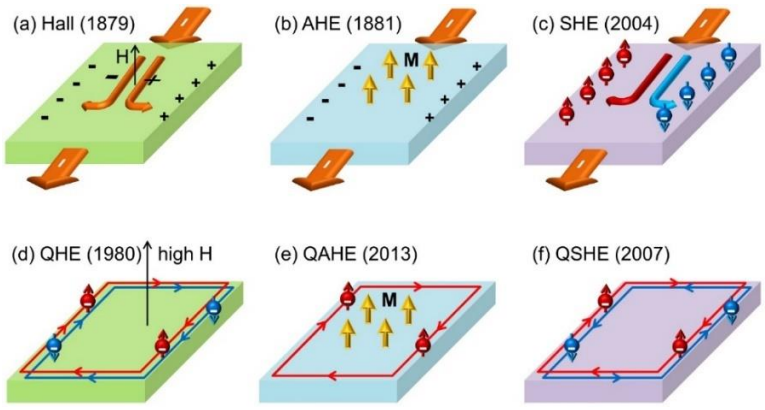

Figure 1-1. Hall family. (a) Ordinary Hall effect discovered in 1879. (b) Anomalous Hall effect (AHE) discovered in 1881. (c) Spin Hall effect (SHE) discovered in 2004. (d) Quantum Hall effect (QHE) discovered in 1980. (e) Quantum Anomalous Hall effect (QAHE) discovered in 2013. (f) Quantum spin Hall effect (QSHE) discovered in 2007. *H* and *M* is the external magnetic field and the magnetization of the material, respectively. Adapted from C. -Z. Chang, J Phys-Condens Mat **28**, (2016).

The Hall effects have played critical roles in the history of solid state physics. In particular, the Hall effects reveal how electrons and spins behave under the circumstance of symmetry breaking and spin-orbit interaction. The complete Hall scenario is summarized in Figure 1-1.

1.2.1. Hall Effect and Quantum Hall Effect

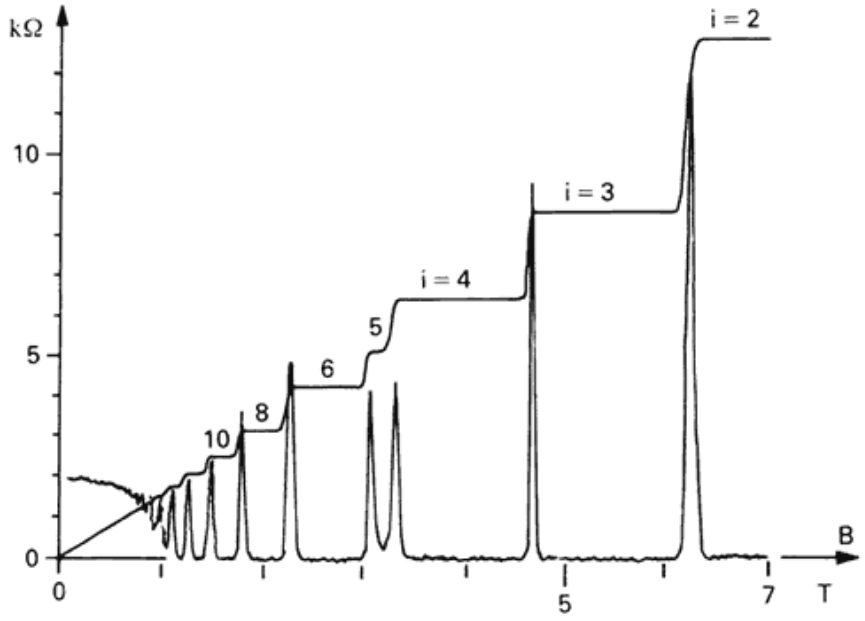

Figure 1-2. The integer Quantum Hall effect. The Hall resistance changes stepwise and takes on the quantized values of Klitzing constant h/e^2. The longitudinal resistance disappears when the Hall resistances reached at plateaus.

In 1879, Edwin H. Hall made an extraordinary discovery that a transverse electric potential is developed, called the Hall voltage, as a consequence of the Lorentz force when a conductor is placed in a magnetic field. This discovery, namely the (ordinary) Hall effect(*4*), provides an elegant tool to identity the carrier type and measure the carrier concentrations of the conducting materials and therefore has been widely used in solid

state electronics. The integer quantum Hall effect (QHE), the quantum regime of the Hall effect, was discovered in 1980 by von Klitzing in the Si/SiO_2 field-effect transistor subjected to low temperatures and strong magnetic fields(*5*).

In two-dimensional electronic systems, the classical electrons follow circular cyclotron orbits when subjected to an external magnetic field. When treated quantum mechanically, these orbits are quantized and the energy levels of these quantized orbits take on discrete values, known as the Landau levels. When the Fermi level falls between two neighboring Landau levels, the bulk carriers are localized but the electrons can propagate through the edge of the samples. Consequently, the Hall resistances form well-defined plateaus and the longitudinal resistance vanishes ideally. It is worthy to mention that a distinctive half-integer QHE was observed in a novel two-dimensional electronic system, i.e. graphene, a monolayer of carbon atoms packed into an honeycomb crystal structure, with massless Dirac fermions(*6, 7*). The unique properties of graphene have brought about a revolution in many disciplines such as quantum electrodynamics, condense matter physics, materials science and engineering, etc.

1.2.2. Anomalous Hall Effect and Quantum Anomalous Hall Effect

When the ferromagnetic materials placed in the external magnetic field, in addition to the ordinary Hall effect, there is another contribution to the Hall response which is approximately proportional to the magnetization of the ferromagnets, known as the anomalous Hall effect (AHE)(*8*). On the theoretical front, the adoption of the Berry-

phase concepts has linked the AHE with the topological nature of the Hall currents. In conventional ferromagnets, three main mechanisms can give rise to an AHE(*8*):

- Intrinsic deflection: As an intrinsic mechanism, Electrons acquire an anomalous velocity perpendicular to the electric field related to their Berry's phase or the Berry curvature.
- Side jump: As an extrinsic mechanism, the electron velocity is deflected in opposite directions by the opposite electric fields experience upon approaching and leaving an impurity.
- Skew scattering: As an extrinsic mechanism, asymmetric scattering occurs due to the effective spin-orbit coupling of the electron associated with an impurity.

While the AHE was discovered next year after the observation of the ordinary Hall effect, quantum anomalous Hall effect (QAHE), predicted by F. Haldane in a two-dimensional lattice model in 1988(*9*), was experimentally realized by Cui-Zu Chang *et al*. in a magnetically doped topological insulator (TI) system 130 years after the discovery of AHE(*10, 11*). The broken time reversal symmetry by ferromagnetism and large spin orbit coupling (SOC) open a nontrivial topological band gap in the TI surface states and leads to the quantized anomalous Hall resistance when the Fermi level is located within the band gap. The temperature to realize the QAHE in this system is extremely low, usually on the order of 10 *mK*, three orders of magnitude lower than the Curie temperature of the ferromagnet. In principle, QAHE is ultimately limited by the Curie temperature T_c of the ferromagnetic phase of magnetic TI. An alternative approach to greatly enhance the T_c is

by proximity coupling TI to a magnetic insulator with high T_c, which will be further discussed in the following chapter.

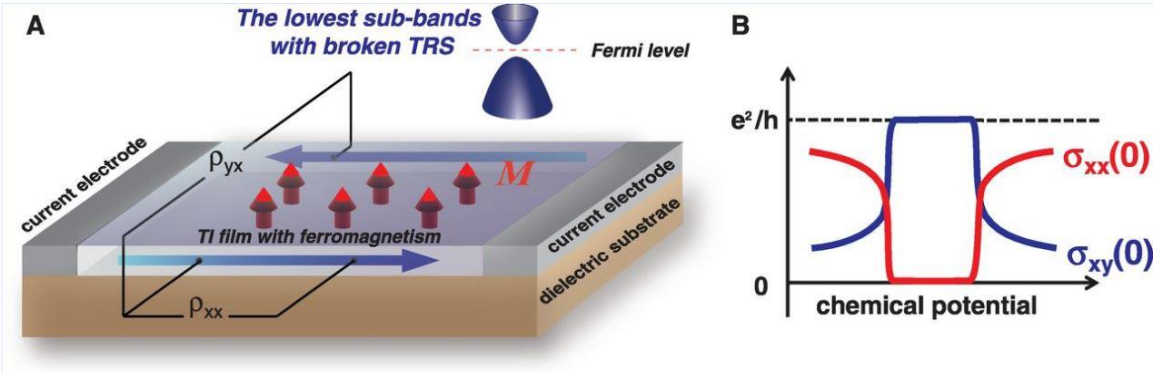

Figure 1-3. The illustration of quantum anomalous Hall effect. A) Principle of QAHE in a TI thin film with ferromagnetic ordering. The magnetization breaks the time reversal symmetry and thus opens up a gap in the Dirac surface states of the topological insulator. B) The anomalous Hall resistance shows a plateau of e^2/h and longitudinal conductance ideally vanishes when the Fermi level falls within the bandgap of TI surface states.

1.2.3. Spin Hall Effect and Quantum Spin Hall Effect

In the Spin Hall effect (SHE), an electrical current passing through a material with large SOC can generate a transverse pure spin current with spin polarization perpendicular to the plane defined by the charge current and spin current (*8, 12*), which was first predicted by M. I. Dyakonov and V. I. Perel in 1971(*13*) and experimentally detected in thin films of n- type GaAs and InGaAs with the use of the Kerr rotation microscopy(*14*). The reciprocal process of SHE, namely inverse spin Hall effect (ISHE), generates a transverse charge potential by passing a pure spin current through a high-SOC material. The SHE and ISHE have been extensively used in magnetic structures as a direct probe of spin currents.

Quantum spin Hall effect (QSHE) was first theoretically proposed in graphene with sufficient intrinsic SOC by C. L. Kane *et al.* in 2005 where spin-up and spin-down electrons exhibit QHE with an opposite chiralities (*15*) and observed in the HgTe/CdTe quantum well structure(*16*) by L. M. Molenkamp *et al.* one year after the prediction of S. C. Zhang *et al*. in this structure(*17*).

Bulk carriers dominate in the unquantized Hall effects, including ordinary Hall effect, AHE and SHE, and encounter back-scattering with the dissipation of energy. When entering the quantum regime in two-dimensional electronic states, the bulk carriers are entirely localized and the edge states carry either spin-polarized current or non-polarized charge current, depending on the intrinsic properties of the systems. Both spin-up and -down branches participate in the QHE and QSHE with different chiralities while only one branch of helical edge transport contributes to the QAHE with time reversal symmetry broken by the ferromagnetic ordering.

1.3. Magnetic Insulator Based Spintronics

Spintronics focuses on the research of spin-dependent transport in solid states materials and devices. Early pioneering works include spin injection from a ferromagnet into a nonmagnetic material(*18*) and giant magnetoresistance effect(*19, 20*), for which the Nobel Prize in Physics was awarded in 2007 to Albert Fert and Peter Grünberg because of their independent discovery of the GMR effect. The past spintronics research heavily relies on the magnetic field control of spin-dependent transport in ferromagnetic

conductors. The drawback of such systems is the energy dissipation associated with the Joule heating in the conducting circuits, which limits the feature size and transistor speed of processor and memory chips. In the past few years, magnetic insulator based spintronics emerged and provided new opportunities in the low-power design of spintronic devices.

1.3.1. Spin Caloritronics

Thermoelectric effects reflect the interplay of heat and charge degree of freedom in condensed matter physics. Motivated by the strategy of coupling spin currents with heat, the recently invigorated spin caloritronics research has focused on the non-equilibrium thermodynamics of spin, charge and heat transport in magnetic structures(*21*). Spin current can be generated by a temperature gradient across a ferromagnet which is known as spin Seebeck effect (SSE), as shown in Figure 1-4.

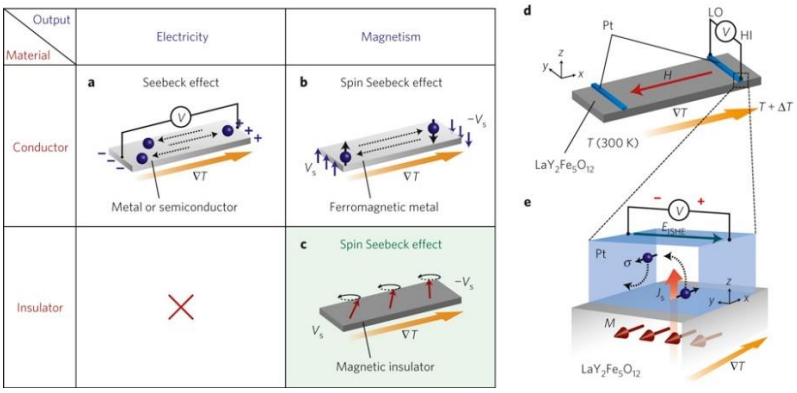

Figure 1-4. The illustration of spin Seebeck effect. a-c) When temperature gradient is applied to a material, an electric voltage is generated in a conductor and a spin current is also generated in ferromagnetic material by creating flow of spin angular momentum. d) Detection of generated spin current by utilizing the inverse spin Hall effect in Pt. e) Device set-up. Adapted from K. Uchida *et al*., Nat. Mater. 9, 894 (2010).

The SSE was first observed in NiFe/Pt bilayers by K. Uchida *et al.* (*22*) in 2008 and then in magnetic semiconductor GaMnAs(*23*) and magnetic insulator $LaY_2Fe_5O_{12}$(*24*) based hybrid bilayers. In the initial transverse geometry of SSE, a thermal gradient in ferromagnetic (FM) layers generates different amount of flow in opposite spin channels due to different scattering rates and densities and therefore leads to a different spatial distribution of spin-up and -down electrons along the temperature gradient. Thin layers of heavy metal Pt detect the electrical voltages from the ISHE with different sign at the two sides of the ferromagnetic metal owing to the accumulation of electrons with opposite spin polarization. Even though the early experiment in the transverse geometry was refuted by other researchers due to the contamination by the anomalous Nernst effect in the presence of an unavoidable perpendicular temperature gradient(*25*) and magnetic proximity effect(*26*), and unreasonable long spin propagation length in the FM layer, the later demonstration of spin Seebeck effect in longitudinal geometry has unambiguously proved the existence of spin current generation by thermal gradient free from proximity induced Nernst effect(*27*). Note that the longitudinal spin Seebeck effect (LSSE) provides a novel strategy to efficiently generate a pure spin current in magnetic structures, especially magnetic insulators and therefore greatly promotes the development of spin caloritronics research.

Spin caloritronic dynamics mainly focuses on the thermoelectric generation of magneto-electronic effects(*21*). Thanks to the reciprocal Onsager relation, explorations on the spin-dependent thermal coefficients (Seebeck(*24*), Peltier(*28*), etc.), thermal mean-free-path(*29*) and thermal spin-transfer torque(*30, 31*) have made considerable advances.

Spin caloritronics has gained momentum in recent years since it couples heat with both spin and charge degrees of freedom in spintronic systems. Magnetic insulator has played an essential role in assisting the development in the relatively young field as it has the advantage of pure spin wave spin current with long spin wave length as a consequence of collective spin wave modes(*3*) compared to FM conductors. The rapid materials development of magnetic insulator nanoscale thin films provides a superior platform for the spin caloritronics research, which will be further discussed in following chapters.

1.3.2. Proximity Effect in Heterostructures

Heterostructures constructed from multiple layers with dissimilar properties have been widely explored in contemporary condensed matter physics research. Proximity effect arises from the quantum mechanical wave function overlap at the interfaces. Due to this proximity effect, new phenomena occur by acquiring properties in the adjacent layers without physically doping foreign atoms which unavoidably degrades the sample quality by introducing disorder in the system. This approach has received increasing attention over the past decade.

Proximity effect in superconductivity describes phenomena that occur when a superconductor is placed in contact with a normal non-superconductor(*32*), such as Majorana fermions are predicted to exist when s-wave superconductor is in proximity with a topological insulator(*33*). In the field of spintronics, magnetic proximity effect is first demonstrated by J. Hauser in 1969(*34*) who studied the penetration depth of the spin polarization of a magnetic metal into a nonmagnetic material with a high exchange-

enhanced spin susceptibility and has been confirmed by x-ray magnetic circular dichroism technique on various conducting ferromagnetic surfaces(*35-37*). Recently, the hybrid structures of a strong SOC metal such as Pt and a magnetic insulator exhibit a variety of interesting spin-dependent phenomena and attract considerable attention. Examples include magnetization orientation dependent magnetoresistance effect, which behaves ostensibly like the conventional anisotropic magnetoresistance (AMR) effect in conducting ferromagnets. However, Pt is a paramagnet and the magnetic insulator does not carry any charge current; therefore the bilayer structure is very different from conducting ferromagnets. The observed magnetoresistance behavior in this bilayer structure can only originate from simultaneous action of SHE and ISHE, namely spin Hall magnetoresistance (SMR) or the conventional anisotropic magnetoresistance in Pt but the interface layer of Pt must be magnetized via magnetic proximity effect.

The heterostructure approach also plays a very important role in other low-dimensional systems, particularly magnetic insulator/TI and magnetic insulator/graphene heterostructures. Graphene and TI are both new types of quantum materials with unique electronic properties, in which the two-dimensional electron systems, either the π-electrons of graphene or the surface states of TI, are described by massless Dirac equations. A distinct difference between graphene and TI is the SOC strength. Therefore, by breaking the time reversal symmetry with an induced magnetic order, and if there is strong enough SOC in graphene (TI already has strong SOC), the Dirac spectrum opens a topological gap and consequently gives rise to the quantized anomalous Hall effect with dissipationless electron transport along the sample edge.

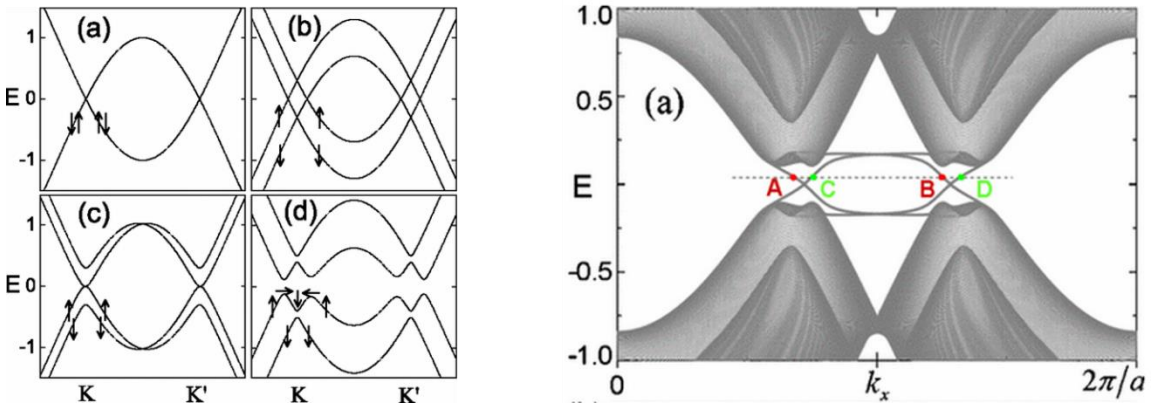

Figure 1-5. The illustration of nontrivial band gap opening in graphene with presence of SOC and exchange interaction. Left**:** a) Pristine state with spin-up and spin-down degenerate; b) when only exchange field is introduced, the spin-up and spin-down bands are vertically shifted; c) with only SOC is present, the spin-up and spin-down states are mixed around the band crossing points; d) when both exchange field and SOC are present, a nontrivial band gap is opened and all the fours bands become nondegenerate. Right: the calculated energy spectrum of zigzag-edged graphene ribbons with specific spin-orbit coupling and exchange coupling parameters. Four different edge states A, B, C, and D are present on the Fermi level. Adapted from Z. Qiao *et al*., Phys. Rev. B 82, 161414(R) (2010).

A conventional way to introduce magnetism in non-magnetic systems is via transition metal doping. A long-range ferromagnetic or antiferromagnetic order originates from the exchange interaction between the magnetic moments carried by the transition metal dopants(*38*). However, raising the Curie temperature T_c requires increasing the doping level, which inevitably lowers the sample quality with the presence of massive disorder, or even destroys the nontrivial Dirac band structure(*39*). An alternative route is to leverage the proximity effect to couple graphene and the TI surface states directly to a high-T_c magnetic insulator without introducing spin disorder. In the following chapters, I will discuss the work of achieved high temperature magnetic phase in the Dirac systems proximity coupled to magnetic insulator, which is the pre-requisite to realize the QAHE. Significant advances in enhancing the SOC in graphene, another pre-requisite of QAHE, have also been recently achieved in a proximity heterostructure by transferring graphene

onto TMD materials(*40, 41*), providing a possible platform for the chiral edge state transport in graphene. The magnetic insulator exchange coupled with graphene and TI opens up new possibilities in topological spintronics.

1.3.3. Interfacial Spin Dynamics in Magnetic Insulator Based Heterostructures

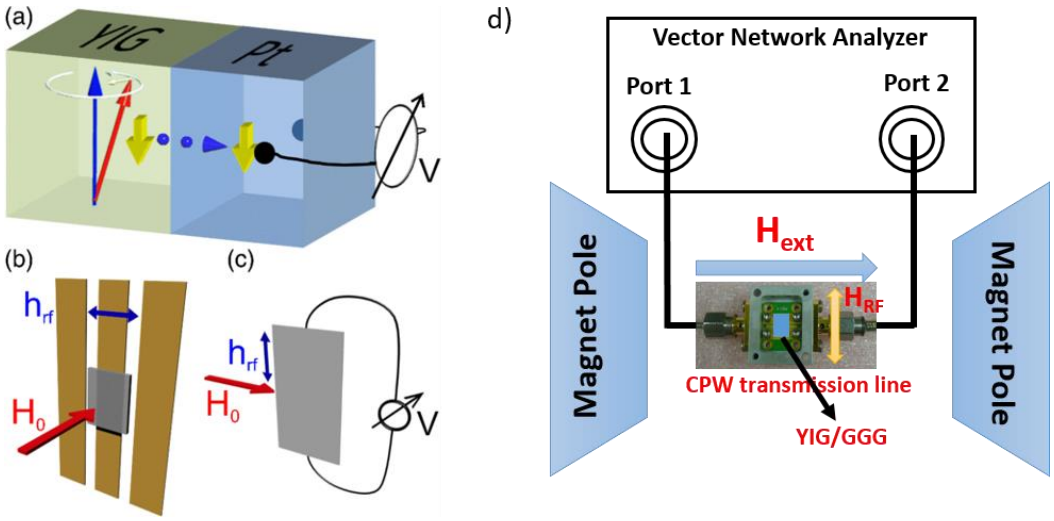

Figure 1-6. The illustration of FMR-driven spin pumping. a) FMR drives spin precession in magnetic insulator layer and the generated net spin angular momentum is transferred to adjacent nonmagnetic material Pt across the interface. The pure spin current in Pt produces a transverse voltage via ISHE. b) Illustration of rf field and external field in FMR. c) Illustration of the electric detection of spin pumping. d) Experimental setup in the broadband FMR experiments. Figures a) – c) are adapted from M. Haertinger *et al.*, Phys. Rev. B 82, 054437 (2015).

In magnetic insulator based heterostructures, conduction electrons cannot pass across the interface into the magnetic insulator layer; but the spin current can still penetrate the interface via the s-d exchange interaction. Spin pumping refers to transfer of spin angular momentum from the uniform magnetization precession motion in a FM layer

to the conduction-electron spin in the neighboring non-magnetic layer (*42*). The spin pumping profoundly affects the dynamics of adjacent magnetic layer, by renormalizing the fundamental parameters, such as the gyromagnetic ratio and the Gilbert damping parameter(*42*). The transferred spin angular momentum generates spin current in the nonmagnetic material and is consequently detected via the transverse voltage generated by ISHE with the presence of high SOC, illustrated in Figure 1-6.

Based on the picture of adiabatic spin pumping, the magnetic property of the magnetic layer, mainly the enhancement of the Gilbert damping constant, has shown to be modulated by the interfacial spin pumping process(*42, 43*). The additional spin pumping damping is characterized by spin-mixing conductance(*42*):

$$\alpha_{sp} = \alpha_{bilayer} - \alpha_{MI} = \frac{g\mu_B}{4\pi M_s} g_{\uparrow\downarrow} \frac{1}{t_{MI}}$$

where g, μ_B, $g_{\uparrow\downarrow}$ and t_{mi} are the Landé-factor, Bohr magneton, spin-mixing conductance, and the thickness of the magnetic layer, respectively. Equivalently, the spin-mixing conductance is proportional to the momentum sum of the imaginary part of the dynamical transverse spin susceptibility Im χ_k^R *(Ω_{rf})(44)*:

$$g_{\uparrow\downarrow} = \frac{2J_{sd}^2 S_0^2 N_{int}}{\hbar^2 N_{ss}} \sum_k \frac{1}{\Omega_{rf}} Im\chi_k^R(\Omega_{rf})$$

where N_{int} being the number of localized spins at the interface of magnetic insulator/nonmagnetic material (MI/NM) heterostructures, N_{ss} being the number of spins in the spin sink, J_{sd} being the s-d exchange coupling, Ω_{rf} being the precession frequency. The spin-mixing conductance characterizes the interfacial spin reflection/transmission

and is related to the spin Hall magnetoresistance at the interface of MI/NM originating from the concerted actions of the direct SHE and ISHE(*45*), which will be addressed in the following chapter.

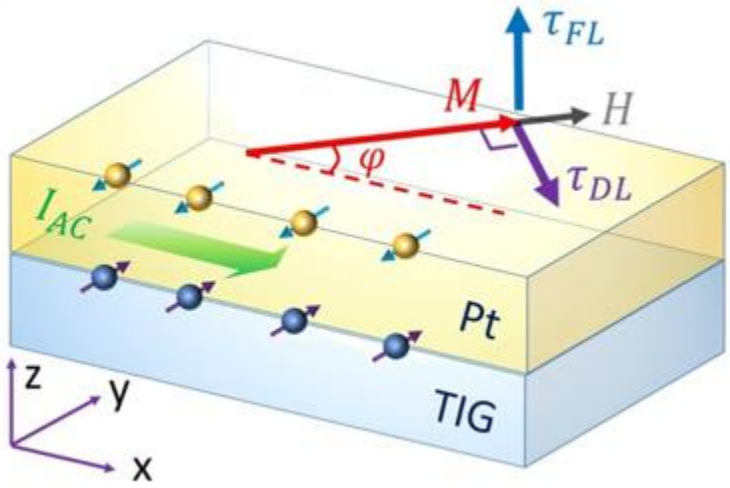

Figure 1-7. The schematic illustration of spin-orbit torque in MI/HM systems. I_{AC} is the rms amplitude of AC current. H and M is the constant in-plane magnetic field and magnetization, φ is angle between the current direction and magnetization. τ_{DL} and τ_{FL} denote the damping-like and field-like torque, respectively.

Another manipulation of magnetization dynamics in ferromagnetic layer/heavy metal (FM/HM) systems is via spin-orbit torque (SOT), which has attracted a great deal of attention from both fundamental and application perspectives. SOT can arise from the pure spin current generated from the charge current primarily flowing in the HM layer via the SHE. In MI/HM heterostructures, however, conduction electrons in HM cannot pass across the interface into the MI layer; but the spin current can still penetrate the interface via the s-d exchange interaction, which gives rise to SOT. On one hand, the pure spin

current impinging on the interface is either be reflected or be transmitted depending on the relative orientations between the spin current polarization $\hat{\boldsymbol{\sigma}}$ and magnetization $\boldsymbol{M}$ in MI. The spin current induced torque on the magnetization of MI, i.e. $\boldsymbol{\tau_{SOT}} = \tau_{DL}\hat{\boldsymbol{m}}\times(\hat{\boldsymbol{m}}\times\hat{\boldsymbol{\sigma}}) + \tau_{FL}(\hat{\boldsymbol{m}}\times\hat{\boldsymbol{\sigma}})$, where τ_{DL} and τ_{FL} are the magnitude of the damping-like torque (DLT) and field-like torque (FLT), respectively. The SOT can be rewritten as $\boldsymbol{\tau_{SOT}} = \hat{\boldsymbol{m}}\times\boldsymbol{H_{DL}} + \hat{\boldsymbol{m}}\times\boldsymbol{H_{FL}}$, where $\boldsymbol{H_{DL}} = \tau_{DL}(\hat{\boldsymbol{m}}\times\hat{\boldsymbol{\sigma}})$ and $\boldsymbol{H_{FL}} = \tau_{FL}\hat{\boldsymbol{\sigma}}$ define the effective fields of DLT and FLT, respectively, illustrated in Figure 1.7. Recently, Li *et al*.(*46*) and Avci *et al*.(*47*) reported SOT induced switching in MI with perpendicular magnetic anisotropy (PMA) by taking advantage of SH-AHE in MI/HM bilayers. It is crucial to determine both damping-like SOT and field-like SOT in order to understand the intrinsic interfacial mechanisms. However, both papers are lack of quantitatively extraction of the field-like SOT. I will present the detailed spin torque study in two bilayer PMA systems, namely TIG/W and TIG/Pt, to further address the deficiency of pure bulk dominating spin current model which neglects the interfacial effects including magnetic proximity effect, Rashba effects, etc.

Chapter 2

Materials Development of Rare Earth Iron Garnet Thin Films

2.1. Introduction

Magnetic insulator (MI) is playing an increasingly important role in spintronics. First, MI is a pure spin current source that can be thermally, resonantly or electrically excited. The spin current in MI is in the form of spin waves that carry linear and angular momentum. The quanta of spin waves are called magnons; therefore, the spin current in MI is sometimes called magnonic spin current. Second, unlike conduction-electron spin currents in metals and semiconductors which are associated with Joule heating and disappear within a very short distance (~ a few nm) called spin diffusion length, if spin current is injected into a MI locally, it can propagate with a much longer distance (many microns) because it is carried by collective motion of spins coupled by exchange interaction and low damping in magnetic insulators. Third, if in proximity with a non-magnetic material with large spin orbit coupling, the exchange interaction provided by MI can spin polarize the electronic states and modify its band structure, consequently leading to exotic transport phenomena. The MI-based heterostructures are unique and useful for studying novel phenomena such as the quantum anomalous Hall effect in topological insulator and graphene. The proximity effect exists in heterostructures of TI/graphene with conducting ferromagnets; however, the magneto-transport properties

such as magnetoresistance and Hall effect are dominated by the conducting ferromagnets. Therefore, magnetic insulators are required for such studies.

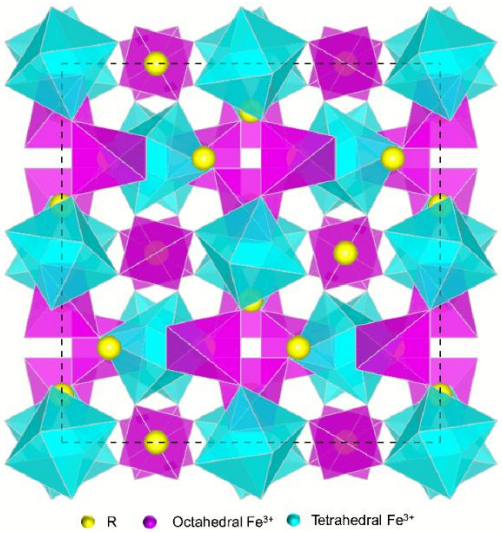

Figure 2-1. The schematic illustration of $R_3Fe_5O_{12}$ unit cell. The Fe^{3+} ions occupy the octahedral and tetrahedral sites while the rare earth ions occupy the dodecahedral sites.

Among a variety of magnetic insulator materials, rare earth iron garnet ($R_3Fe_5O_{12}$ or RIG) family has attracted the most attention for their unique spin dynamic and magneto-optical properties since 1960s. Compared with other magnetic insulators, such as EuS and EuO, RIG family has a high Curie temperature (~550 K) and a large band gap(*48*) (~2.85 eV). RIG, having a formula $\{A_3^{2+}\}[B_2^{3+}](C_3)O_{12}$, belongs to the space group *Ia3d* and contains 8 formula units in the unit cell(*49*). There are three magnetic sublattices in ferromagnetic insulator RIG. Through the superexchange interaction, the moments of the three Fe^{3+} ions in the tetrahedral sites (*d* sites) interact antiferromagnetically with the moments of the two Fe^{3+} ions in octahedral sites (*a* sites).

Additionally, the rare-earth ions in dodecahedral cites (*c* sites) are weakly exchange coupled ferromagnetically to the Fe^{3+} in *a* sites, which experience a strong temperature dependent paramagnetic moment. At the compensation temperature, the total magnetization of *a* sites Fe^{3+} and *c* sites rare earth ions is equal to the magnetization of *d* sites Fe^{3+}, giving rise to a vanishing net magnetic moment of RIG. The unit cell of RIT is illustrated in Figure 2-1.

Yttrium iron garnet ($Y_3Fe_5O_{12}$ or YIG) is the most popular material in RIG family in modern magnetic insulator spintronics study owing to its extremely low Gilbert damping ($\sim 3 \times 10^{-5}$). YIG is an ideal Néel ferrimagnet with no magnetic moment contributed from Y^{3+}. Therefore, YIG has no compensation temperature remaining magnetic below $T_c \sim 550$ K. Because there are three Fe^{3+} in d sites and two Fe^{3+} in a sites, the resultant magnetic moment per formula unit is 5.0 μ_B in principle, consistent with the reported experimental values varying from 4.72 μ_B to 5.01 $\mu_{B(49)}$. The absence of compensation temperature, associated with its other excellent magnetic properties like low magnetic damping, makes YIG the material of choice or a preferred material in modern spintronics research.

The RIG-based heterostructures have been shown to give rise to emerging novel spin transport phenomena, such as induced ferromagnetism in nonmagnetic material via magnetic proximity effect (MPE), thermal generation of pure spin current via SSE, the spin current modulated magnetoresistance in nonmagnetic materials via SMR etc. Therefore, the materials development of high quality nanometer-thick MI thin films becomes very important in the nanoscale spintronics research.

In this chapter, I will first introduce the exquisite control growth control of nanometer thick YIG thin films grown on perfectly lattice matched substrate gadolinium gallium garnet (GGG) substrate using pulsed laser deposition (PLD) technique(*50*) in section 2.2. Successful engineering of high quality platinum/YIG inverted structure for spin current transport(*51*) is in section 2.3. Finally, the interfacial lattice mismatch induced strain tunable the magnetic anisotropy in Bi:YIG by decreasing the film thickness and in $Tm_3Fe_5O_{12}$ by intentionally choosing substituted GGG (SGGG) or $Nd_3Ga_5O_{12}$ (NGG) with larger lattice constant than TIG is discussed in section 2.4.

2.2. Exquisite Control and Magnetic Properties of YIG Thin Films

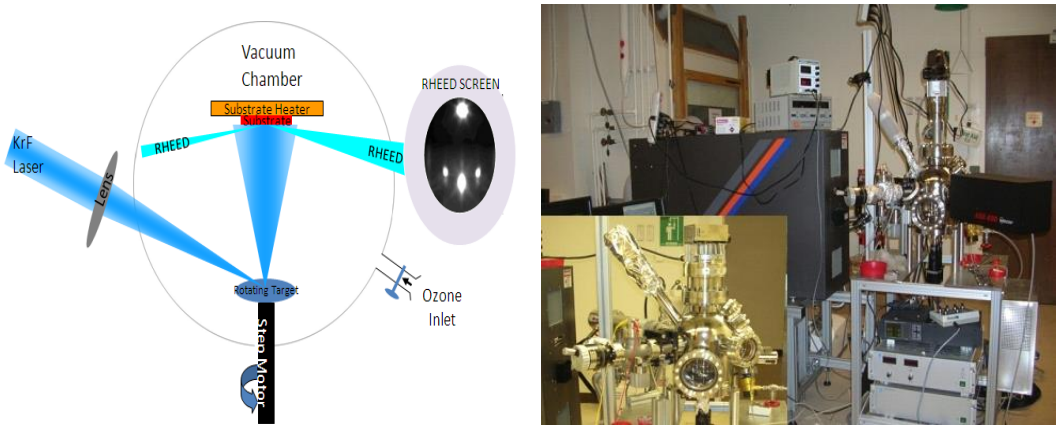

Figure 2-2. PLD deposition system. Left: Schematic illustration of different components in the PLD system. Right: Real image of our PLD set up.

Unlike in bulk crystal applications, thin film devices are influenced by interactions across the interface; therefore, the surface properties (e.g. morphology and magnetism) are extremely important. PLD is a common technique for oxide thin film

growth, as shown in Figure 2-2 with different components included in the schematic illustration. However, systematic studies of YIG growth and correlation between structural and magnetic properties are relatively scarce. In this section, we demonstrate an exquisite control of (110)-oriented YIG film growth with PLD. By achieving the layer-by-layer growth, ultra-smooth atomic terraces are obtained. We show that the YIG films have in-plane uniaxial anisotropy and extremely low Gilbert damping.

YIG powder purchased from Alfa Aesar is densified via the current activated pressure assisted densification (CAPAD) processing technique at 950 $^{\circ}$C with an applied load of 100 MPa for 5 mins. The final relative density of the target is over 85%, and the crystal structure of YIG target is confirmed by x-ray diffraction. The commercially available GGG (110) substrates are rinsed sequentially with acetone, isopropyl alcohol, DI water and then annealed in oxygen at 1000 $^{\circ}$C for 6 hours. As discussed in details later, because of this substrate treatment, atomically terraced GGG surface emerges, enabling the subsequent ultra-flat terraced YIG film growth. The substrates are *in situ* baked with a base pressure around 5 x 10^{-7} Torr at ~200 $^{\circ}$C for 5 hours. Before deposition, the substrates are then annealed at ~750 $^{\circ}$C under a 1.5 mTorr oxygen pressure with 12 wt% ozone for 30 mins. During the pre-deposition annealing, the reflection high-energy electron diffraction (RHEED) spots become sharper and brighter, and the intensity saturates after 30 mins annealing. Then, under the same condition of oxygen and temperature as the pre-deposition annealing, the KrF excimer laser pulses of 248 nm in wavelength with power of 150 mJ strike the target at a repetition frequency of

1 Hz. The differentially pumped RHEED is kept on to monitor the growth of YIG layers *in situ*.

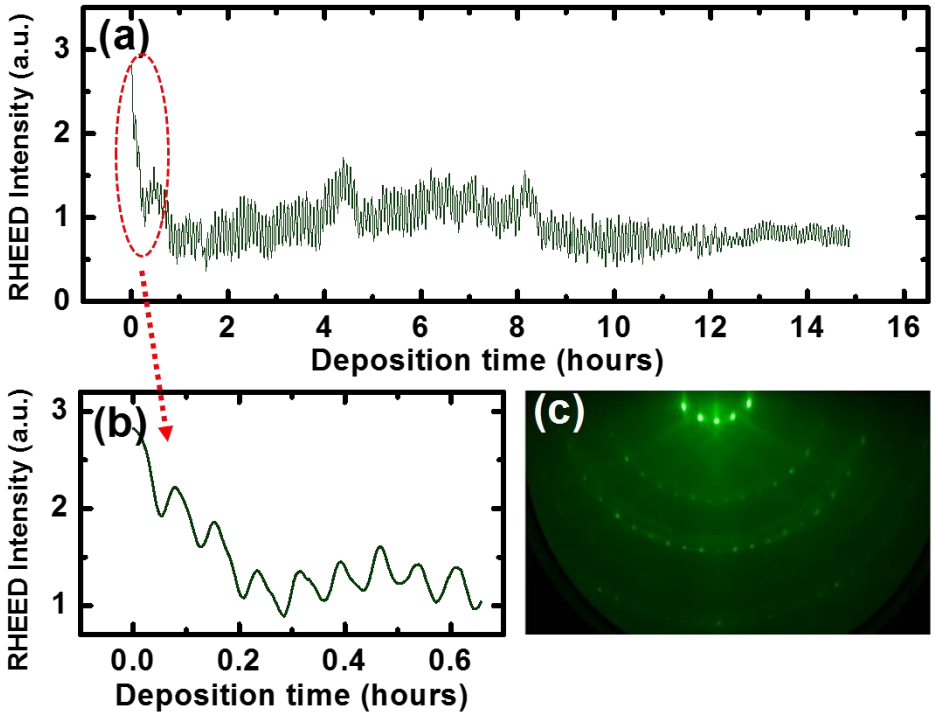

Figure 2-3. *In situ* RHEED oscillations of YIG growth and RHEED patterns of as-grown YIG films. (a) 227 layers (100 nm) thick YIG film of continuous layer by layer RHEED oscillations observed during the growth on (110) GGG substrate using pulsed laser deposition technique. (b) Zoom-in data of RHEED oscillations for a chosen time slot. (c) RHEED pattern of YIG film showing single crystalline structure of YIG after deposition.

As shown in Figure 2-3 (a), 227 continuous RHEED intensity oscillations are observed before the termination of growth, showing excellent layer-by-layer epitaxial growth of YIG. The oscillation period of 300 s represents growth of one atomic layer along the (110) direction of the cubic cell of GGG with the lattice constant of 12.383 Å. The layer-by-layer growth obtained with such a low repetition rate is below the threshold

found in a previously report(*52*). The film thickness is calculated to be ~100 nm which is further confirmed by atomic force microscopy (AFM) and a Dektak profilometer, and the film growth rate is 0.09 nm/min. Figure 2-3 (b) shows a few zoom-in RHEED oscillations. Figure 2-3 (c) is the RHEED pattern of the as-grown YIG film which shows the identical cubic crystalline structure to that of GGG with negligible lattice mismatch. The Kikuchi lines from the diffraction of diffusely scattered electrons(*53*) are also clearly resolved, confirming that the YIG film is of high crystallinity.

Atomically flat substrate surface is essential to obtaining high-quality growth of epitaxial film on top. The surface quality is monitored by atomic terrace formation upon treatment. A wide range of annealing temperatures (from 400 to 1300 $^{\circ}$C) has been explored to study the effect of annealing and the results are summarized in Figure 2-4 (a-c). Figure 2-4 (a) shows the surface morphology of a purchased GGG substrate right after cleaning but without annealing. The root-mean-square (RMS) roughness is 0.51 nm. After annealed in oxygen at 1000 $^{\circ}$C for 6 hours, atomic terraces emerge as shown in Figure 2-4 (b). Similar results were previously found on annealed STO substrates(*54*). In the meantime, the RMS roughness is greatly reduced down to 0.15 nm. However, when the annealing temperature is increased to 1100 $^{\circ}$C for the same amount of time, pits and cracks appear on

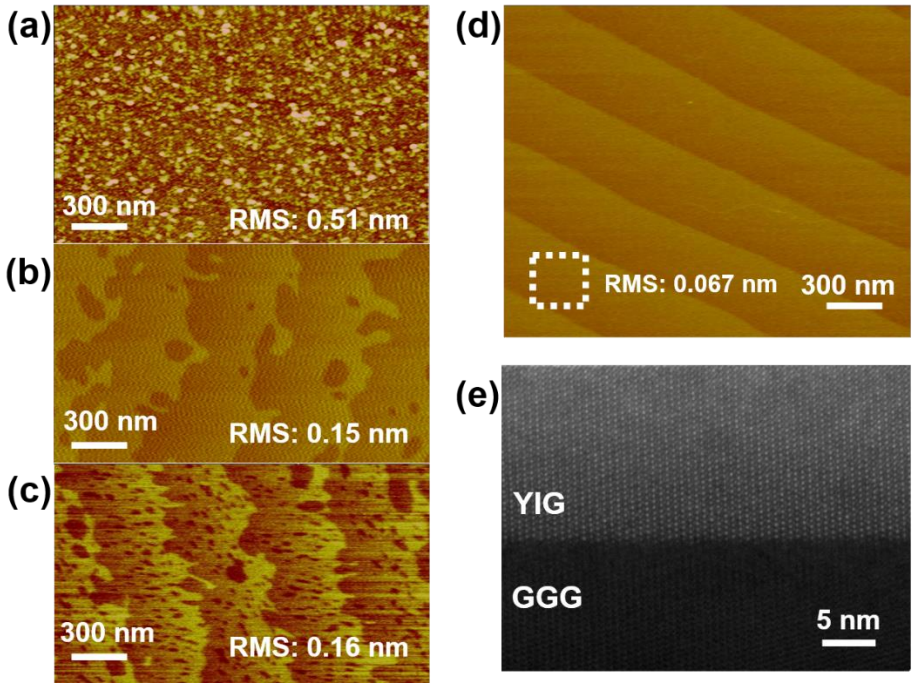

Figure 2-4. The structural properties of YIG thin films. (a) AFM surface morphology of GGG substrates after different surface treatments. Top: original purchased GGG substrates after ultra-sonicated in acetone and isopropanol for surface cleaning. (b) Annealed GGG substrates at 1000 $^{\circ}$C in O_2 environment for 6 hours. (c) Annealed GGG substrates at 1100 $^{\circ}$C in O_2 environment for 6 hours. (d) AFM surface morphology of 30 nm thick YIG film on (110) GGG substrates. (e) TEM image of 30 nm thick YIG thin film on (110) GGG substrate.

the entire substrate, even though the RMS roughness is only increased slightly. Figures 2-4 (a-c) display the dramatic effect of annealing on the GGG substrates. Annealing temperature needs to be sufficiently high to promote atomic mobility to reduce roughness but sufficiently low to keep the stoichiometry (preventing volatilization of ions) in the film. The optimized temperature, 1000 $^{\circ}$C is 0.63 of the melting T_m. At this temperature one would expect volume diffusion to be active. It is likely that 1100 $^{\circ}$C (T/T_m = 0.69) causes too much long-range diffusion or volatilization. For comparison, Figure 2-4 (d) is the surface profile for a 30 nm thick YIG film. Extremely smooth atomic terraces with roughness 0.067 nm are evidently resulted, due to the layer-by-layer growth

mode that preserves the excellent initial surface morphology. We emphasize that it is the first time to observe such long RHEED oscillations and atomically smooth terraces with the lowest surface roughness in the YIG film growth. Figure 2-4 (e) shows a transmission electron microscopy (TEM) image of the 30 nm YIG film grown on GGG (110), indicating a sharp interface with negligible mismatch between YIG and GGG. Atomically resolved YIG layers show the epitaxy, consistent with the previous RHEED results.

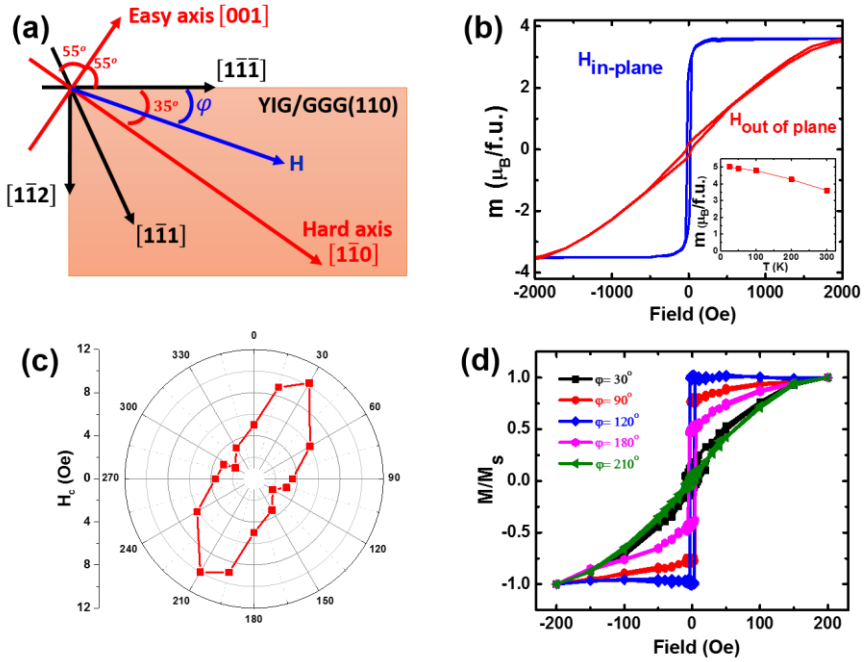

Figure 2-5. The magnetic properties of YIG thin films. (a) Coordinate system of YIG film plane with the orientations of crystalline directions. (b) Magnetic hysteresis loop measurements of 30 nm thick YIG film on (110) GGG with field out of plane (red) and in film plane (blue) at 300K. Inset: A temperature dependence of saturation magnetization in unit of μ_B per formula unit. (c) Azimuth angle dependence of coercive field. (d) In-plane angle rotation of magnetic hysteresis loops showing in-plane two-fold symmetry of (110) oriented YIG film.

YIG hysteresis loops are measured using a vibrating sample magnetometer (VSM) with both out-of-plane and in-plane field orientations, as shown in Figure 2-5. Figure 2-5(a) is a top view of the YIG sample marked with main crystallographic

orientations. The two edges of (110)-orientated GGG substrate are confirmed to be along $[1\bar{1}\bar{1}]$ and $[1\bar{1}2]$. $[1\bar{1}1]$, another member of the $\langle 111\rangle$ family, lies at an angle of 70° with respect to the $[1\bar{1}\bar{1}]$ edge. YIG films grown on GGG have the easy axis lying in the film plane shown by Figure 2-5(b), due to the dominance of shape anisotropy(*55*). The saturation moment is found to be 3.5 μ_B per formula unit at room temperature and reaches approximately 5 μ_B at 10 K. Aside from the strong in-plane anisotropy, the (110)-oriented YIG film shows two-fold symmetry in the film plane, as indicated in Figure 2-5(c) and (d). The azimuth angle φ is measured between the external field H and the $[1\bar{1}\bar{1}]$ edge. Figure 2-5(d) is the in-plane magnetic hysteresis loops for a few selected φ angles, showing an in-plane easy axis oriented at φ=30° and an in-plane hard axis along the orthogonal direction, i.e. φ=120°. The azimuth angular dependence of the coercive field is illustrated in Figure 2-5(c), showing clear in-plane uniaxial symmetry. The observed in-plane uniaxial anisotropy is obviously related to the crystalline structure of the (110)-oriented YIG film. In bulk YIG, $\langle 111\rangle$ and $\langle 1\bar{1}0\rangle$ are the easiest and hardest axes, respectively(*56*). In the film plane of (110)-oriented YIG, there are two equivalent axes from the $\langle 111\rangle$ family, and the $[001]$ axis lies in between these two axes about 55° from each. As a consequence, [001] becomes the in-plane easy axis, and $[1\bar{1}0]$, about 35° from the $[1\bar{1}\bar{1}]$ edge and perpendicular to $[1\bar{1}0]$, becomes the in-plane hard axis, which corresponds well to φ =30° found in experiments. The torque measurements on flux-grown magnetic garnets also exhibit similar noncubic anisotropy, which was interpreted in terms of a growth induced pair-ordering model(*56*).

To further characterize the magnetic anisotropy, ferromagnetic resonance (FMR) measurements are carried out either using a Bruker 9.6 GHz EMX EPR spectrometer or a broad-band coplanar waveguide setup with a vector network analyzer to measure the transmission signal. In a real ferromagnetic system, Landau Lifshitz Gilbert (LLG) equation considers the magnetization dynamics in the following way:

$$\frac{d\vec{M}}{dt} = -\mu_0\gamma\vec{M}\times\vec{H}_{ext} + \frac{\alpha}{M_s}\left(\vec{M}\times\frac{d\vec{M}}{dt}\right)$$

where $\vec{M}$ is the magnetization, μ_0 is the vacuum magnetic permeability, γ is the gyromagnetic ratio, $\vec{H}_{ext}$ is the external magnetic field, M_s is the saturation magnetization and α is the Gilbert damping constant. A varying magnetic field h_{rf} perpendicular to the external magnetic field with frequency f leads to a precession of magnetization about the equilibrium direction. A maximum of energy absorption would occur if the radio frequency (RF) equals to the precession frequency. The FMR technique provides a delicate way to extract the intrinsic magnetic information of the materials, such as the Gilbert damping constant and magnetic anisotropy. The Gilbert damping constant follows:

$$\Delta H = \frac{\alpha f}{\gamma} + \Delta H_0$$

where ΔH is the linewidth of the FMR signal and ΔH_0 is denoted as the inhomogeneity linewidth broadening. The magnetic anisotropy can be accurately acquired from the polar angle dependent FMR study(*57, 58*) by extracting effective demagnetizing magnetization

$4\pi M_{eff} = 4\pi M_s - H_\perp$, where $4\pi M_s$ and $H_\perp$ are the shape anisotropy and out-of-plane magnetic anisotropy, respectively.

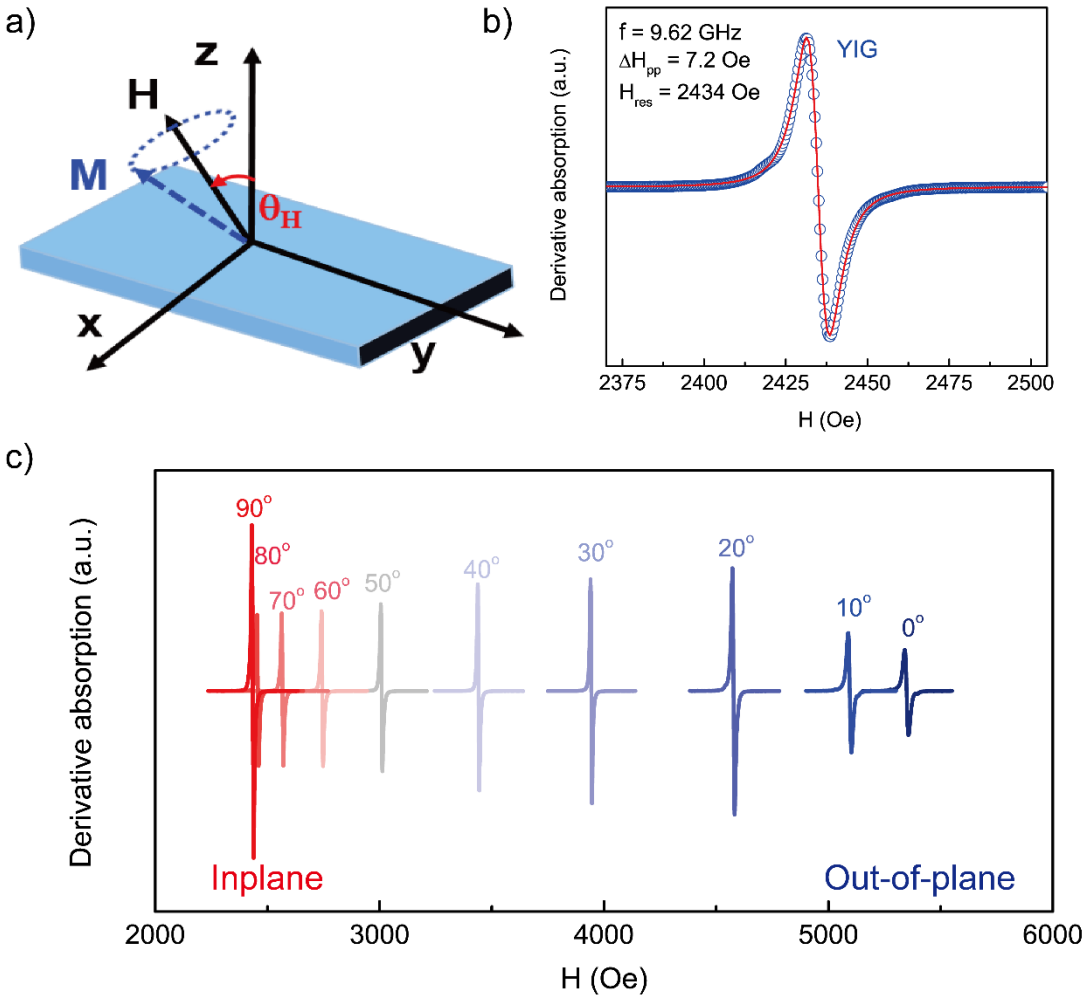

Figure 2-6. Ferromagnetic resonance spectra of nanometer thick YIG thin films. a) Schematic illustration of measurement set up. The magnetic field H is applied with the angle θ_H with respect to the normal direction associating with a precession of magnetization about the static field H. b) The in-plane cavity FMR absorption peak at frequency of 9.62 GHz for 10 nm bare YIG film with resonance field H_{res} about 2434 Oe and peak-to-peak linewidth ΔH_{pp} about 7.2 Oe, indicating a high quality low magnetic damping YIG film. c) The polar angle θ_H dependent FMR spectra with magnetic field rotation from inplane ($\theta_H = 90^o$) to out-of-plane direction ($\theta_H = 90^o$).

Figure 2-6 shows a typical FMR spectrum of a 10 nm thick bare YIG film, with set up illustrated in Figure 2-6(a). Figure 2-6(b) shows the FMR signal with an in-plane magnetic field. The FMR derivative absorption signal shows a single Lorentzian feature with the peak-to-peak linewidth ΔH_{pp} of 7.2 Oe at the resonance field H_{res} = 2434 Oe. When FMR is performed with different polar angles θ_H's (defined in Figure 2-6(a)), the single Lorentzian shape of FMR spectra remains from the magnetic field in-plane to out-of-plane geometry. The single Lorentzian absorption with such a narrow linewidth indicates high uniformity of the bare YIG films. The exquiste control over the YIG quality serve as the baseline for future spin transport study on YIG based heterostructures.

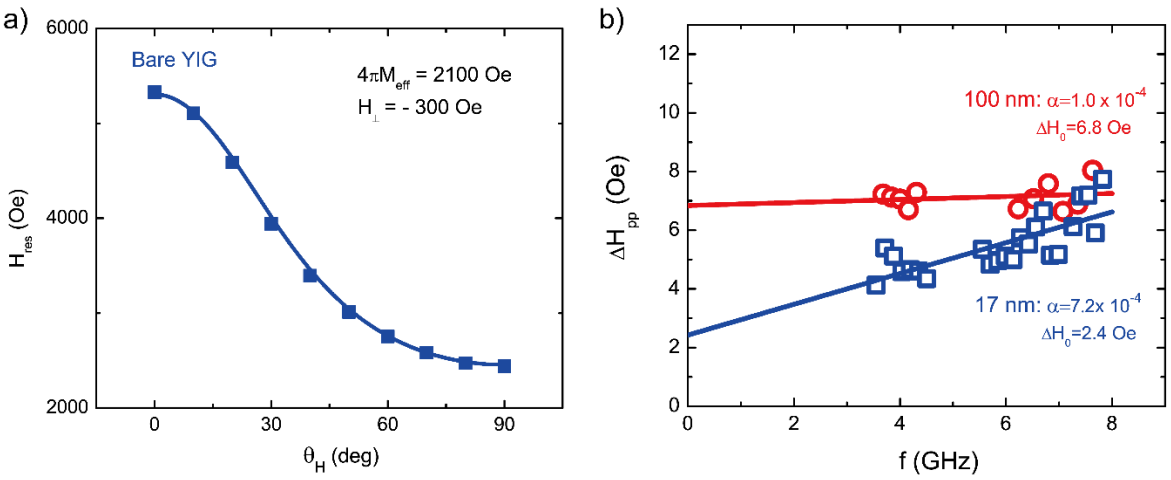

Figure 2-7. The magnetic anisotropy and Gilbert damping constants of YIG thin films from the FMR measurement. a) The polar angle dependent of magnetic resonance field H_{res}, indicating a dominance of in-plane magnetic anisotropy with out-of-plane uniaxial field $H_{\perp}$ about -300 O. b) The Gilbert damping constants of 100 nm YIG films is as low as 1.0×10^{-4} while the 17 nm YIG film has a slight larger Gilbert damping constant reaching 7.2×10^{-4}.

As shown in Figure 2-7(a), the magnetic anisotropy can be extracted from fitting the polar angle dependent magnetic resonance field H_{res}(*57, 58*). The effective magnetization $4\pi M_{eff}$ is 2100 Oe, slighter larger than the saturation magnetization of YIG film 1800 Oe, indicating a dominance of in-plane magnetic anisotropy consistent with the VSM measurement. The magnitude of the uniaxial magnetic anisotropy field is 300 Oe with a negative sign suggesting preference of magnetization lying in the film plane. We obtain the intrinsic Gilbert damping constant α from the slope and the inhomogeneity linewidth broadening ΔH_0 from the intercept of the frequency dependence of FMR linewidth. The damping constant α for 100 nm thick YIG is ~ 1.0×10^{-4}, among the best reported values of nm-thick YIG films(*50*), and with a moderate ΔH_0 = 6.8 Oe. The 17 nm YIG sample has a slightly larger value of $\alpha = 7.2 \times 10^{-4}$ and a smaller ΔH_0 = 2.4 Oe. FMR measurements are also extended to a higher frequency range using the Ku band shorted waveguide, and the Gilbert damping is determined to be from 7.0×10^{-4} to 1.0×10^{-3}, for YIG films with different thicknesses (15-30 nm), consistent with the VNA measurements. The increased Gilbert damping in thin films compared with that of the bulk (~3×10^{-5}) can be understood as a result of interface-defect associated two-magnon scattering(*59*) in ultrathin films. The increased damping in nanometer-thick YIG films significantly shortens the spin wave propagation length down to tens of μm compared to the mm scale of bulk YIG.

In summary, we have demonstrated an exquisite control of YIG film growth using PLD. Single crystal YIG films have been epitaxially grown layer by layer up to 227 atomic layers continuously. Under the optimized sample treatment and growth, atomic

terraces emerge in (110)-YIG films over a large range of thicknesses, thanks to the layer-by-layer growth mode. (110)-YIG films show well-defined uniaxial in-plane anisotropy. The extremely low damping constant from FMR measurements confirms the superb quality of YIG films resulted from the distinct growth mode.

2.3. Platinum/YIG Inverted Structures

In this section, high quality 30-80 nm thick YIG films are grown by PLD on a 5 nm thick sputtered Pt atop GGG (110). Upon post-growth rapid thermal annealing, single crystal YIG (110) emerges as if it were epitaxially grown on GGG (110) despite the presence of the intermediate Pt film. The YIG surface shows atomic steps with the RMS roughness of 0.12 nm on flat terraces. Both Pt/YIG and GGG/Pt interfaces are atomically sharp. The resulting YIG (110) films show clear in-plane uniaxial magnetic anisotropy with a well-defined easy axis along <001> and a peak-to-peak ferromagnetic resonance linewidth of 7.5 Oe at 9.32 GHz, similar to YIG epitaxially grown on GGG. Both spin Hall magnetoresistance and longitudinal spin Seebeck effects in the inverted bilayers indicate excellent Pt/YIG interface quality.

To form YIG based bilayers for spin transport such as YIG/Pt, a thin polycrystalline metal layer is typically deposited on top of YIG by sputtering, which results in reasonably good inter-faces for spin current transport. For some studies such as the magnon-mediated current drag(*60*), sandwiches of metal/YIG/metal are required, in which YIG needs to be both magnetic and electrically insulating. However, high-quality bilayers of the reverse order, i.e., YIG on metal, are very difficult to be fabricated. A

main challenge is that the YIG growth requires high temperatures and an oxygen environment which can cause significant inter-diffusion, oxidation of the metal layer, etc., and consequently lead to poor structural and electrical properties in both metal and YIG layers. Combined with low-temperature growth which suppresses the inter-diffusion, subsequent rapid thermal annealing (RTA) and optimization of other growth parameters result in well-defined magnetism, atomically sharp Pt/YIG interface, and atomically flat YIG surface. In addition, despite the intermediate Pt layer that has a drastically different crystal structure from the garnets, the top YIG layer shows desired structural and magnetic properties as if it were epitaxially grown on GGG (110).

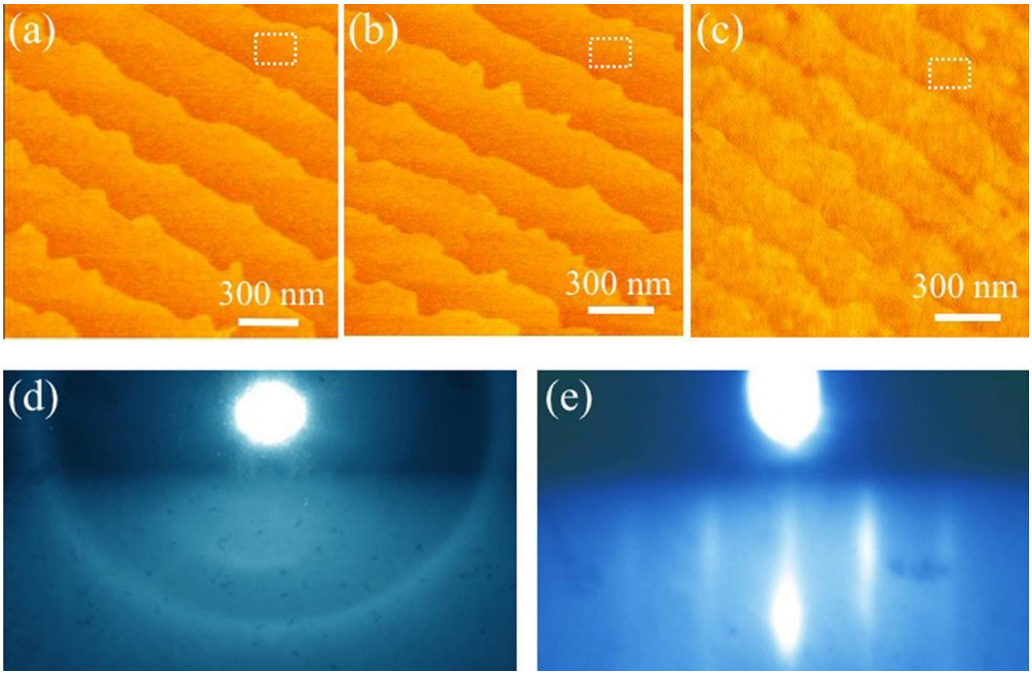

Figure 2-8. Surface characterization of YIG thin film grown on GGG (110)/Pt (5 nm). a)-c) 2 × 2 μm^2 AFM scans of GGG (110) substrate, GGG (110)/Pt (5 nm) and GGG/Pt (5 nm)/YIG (40 nm), respectively. RHEED patterns of as grown (d) and annealed (e) GGG (110)/Pt (5 nm)/YIG (40 nm).

Standard substrate treatment of GGG are performed prior to Pt sputtering and YIG growth. AFM is carried out to track the surface morphology of the substrates and films during the whole process. Figure 2-8(a) shows the $2 \times 2\ \mu m^2$ AFM scan of an annealed GGG (110) substrate. Flat atomic terraces are clearly present, consistent with previous study. The RMS roughness on the terrace is ~ 0.74 Å. Then the substrate is transferred into a sputtering chamber with a base pressure of 5×10^{-8} Torr for Pt deposition. DC magnetron sputtering is used with the Ar pressure of 5 mTorr and power of 37.5 W. The sputtering deposition rate is 0.76 Å/s, and sample holder rotation speed is 10 rpm. After the 5 nm thick Pt deposition, the surface of the Pt film is found to maintain the atomic terraces of the GGG (110) substrate, except that the RMS roughness on the Pt terraces is increased to 1.05 Å as shown in Figure 2-8(b). It is rather surprising that the 5 nm Pt layer doesn't smear out the terraces separated by atomic distances given that the sputtering deposition is not particularly directional. Strikingly, terraces are still present even in 20 nm thick Pt. The PLD growth shares the same set of parameters except the growth temperature is kept at moderate temperature ~ 450 °C to prevent the oxidization of metal layer. After deposition, the YIG films are ex situ annealed at 850 °C for 200 s using RTA under a steady flow of pure oxygen. After RTA, the surface morphology is examined by AFM again. Figure 2-8(c) shows the atomically terraced surface of a 40 nm thick YIG film with RMS of 1.24 Å on the terrace. In this study, the thickness of YIG ranges from 30 to 80 nm and all samples exhibit clear atomic terraces. Even though YIG annealed at such as high temperature, with the short annealing time, the flat and smooth YIG surface is maintained. To track the structural properties of YIG, we use RHEED to

characterize the YIG surface at every step of the process. Figure 2-8(d) shows the RHEED pattern of the as-grown YIG surface. It clearly indicates the absence of any crystalline order. After the *ex situ* RTA, the sample is introduced back to the PLD chamber for RHEED measurements again. A streaky and sharp RHEED pattern is recovered as displayed in Figure 2-8(e) which suggests a highly crystalline order. This result is particularly interesting since it shows the characteristic RHEED pattern of YIG grown on GGG(*50*).

To further confirm its crystalline structure, x-ray diffraction (XRD) using the Cu Ka_1 line has been carried out over a wide angle range (2θ from 10° to 90°) on the GGG/Pt/YIG sample discussed in Figure 2-9(a). Because of the close match in lattice constants between YIG and GGG substrate, weak YIG peaks are completely overlapped with strong peaks of GGG so that they are indistinguishable. Three main Bragg peaks of YIG and GGG are observed: 220, 440, and 660, which suggests the (110) growth orientation of both YIG and GGG. No individual weak YIG peaks can be found. It is striking that the YIG film adopts the crystallographic orientation of GGG despite the intermediate Pt layer. By comparing with the spectra of YIG grown directly on GGG, we can identify a new peak ($2\theta \sim 10^\circ$) which is better seen in the zoom-in view in the inset of Figure 2-9(b). We determine this as the 111 peak of the 5 nm thick Pt film that suggests the (111) texture of the Pt layer. It is not clear whether the (111) texture in the intermediate Pt layer is required for YIG to develop the same crystallographic orientation as that of the GGG substrate.

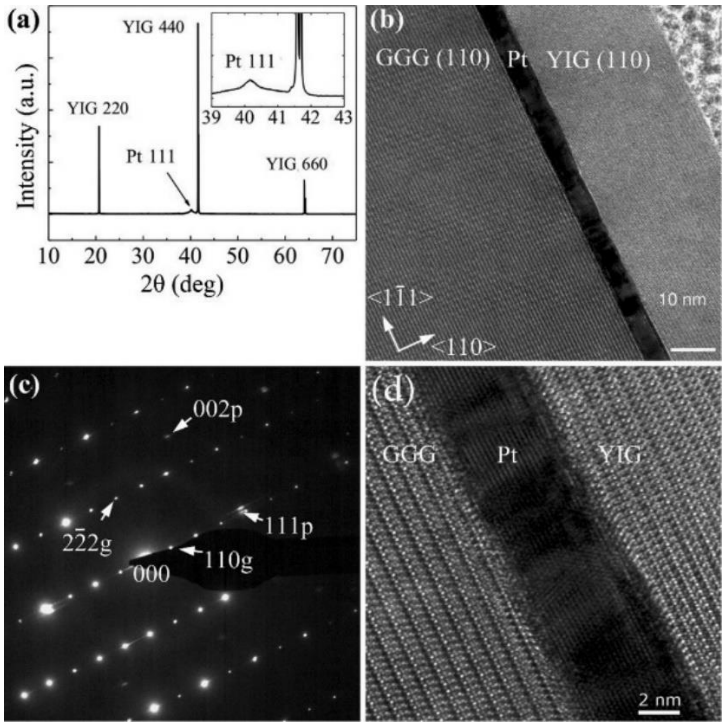

Figure 2-9. Structure characterization of GGG/Pt/YIG heterostructure. (a) XRD of YIG film grown on GGG (110)/Pt (5 nm). Inset: zoom-in plot of Pt 111 peak. (b) TEM image of GGG (110)/Pt (5 nm)/YIG (110) (40 nm) heterostructure. The $\langle 1\bar{1}1\rangle$ and $\langle 110\rangle$ directions in GGG are shown for reference. (c) Selected area electron diffraction pattern along $[\bar{1}12]$ zone axis in GGG obtained from an area containing all three layers showing diffraction spots of YIG, GGG and Pt. The garnet reflections are labeled with subscript 'g' and Pt ones with 'p'. (d) HRTEM lattice image along (110) planes in both YIG and GGG are parallel to the interface with the Pt film, and the latter is composed of nanometer size crystalline domains oriented with their (111) lattice planes parallel to the interface as well. Slight bending and disruption of the (111) lattice fringes between adjacent Pt domains are visualized.

The locking of the (110) orientation in both YIG and GGG is further investigated by the high-resolution transmis-sion electron microscopy (HRTEM) in real space. Figure 2-9(b) first reveals sharp and clean interfaces of Pt/YIG and GGG/Pt. No amorphous phase or inclusions are visible at these two interfaces. Furthermore, the (110) atomic planes of YIG and GGG are parallel to each other and show very closely matched inter-planar spacing. Despite the Pt layer in between, the crystallographic orientation of YIG is

not interrupted as if it were epitaxially grown on GGG directly. In the selected area electron diffraction pattern shown in Figure 2-9(c), taken along the ⟨112⟩ zone axis in garnet from an area that includes all three phases, YIG and GGG diffraction spots overlap with each other, consistent with the XRD results. There is minor splitting of the 110 type reflections from the two garnet phases due to a slight rotation of the two garnet lattices of less than 0.5°. Surprisingly, the diffraction spots from the 5 nm Pt layer show a single crystal pattern with minor streaking parallel to 111 in Pt. The diffuse char-acter of the Pt reflections suggests that Pt is essentially a single crystal consisting of small structural domains with minor misalignments. The contrast variation in different regions of Pt shown in Figure 2-9(b) is consistent with such small structural domain misalignments in Pt crystal grain orientations. Furthermore, the 111 reciprocal vector of Pt and the 110 reciprocal vector of GGG/YIG are both perpendicular to the interfaces, indicating that the (111) Pt layers are parallel to the (110) layers of both GGG and YIG. Figure 2-9(d) is a HRTEM image with high magnification of the three layers, further revealing sharp interfaces.

To investigate the magnetic properties of the GGG/Pt/YIG inverted heterostructure, VSM and FMR measurements are carried out at room temperature. As-grown YIG films do not show any well-defined crystalline structure as indicated by the RHEED pattern. Meanwhile, the VSM measurements do not show any detectable magnetization signal. Upon RTA, single crystal YIG becomes magnetic as shown by the hysteresis loops in Figure 2-10(a) for magnetic fields parallel and perpendicular to the sample plane.

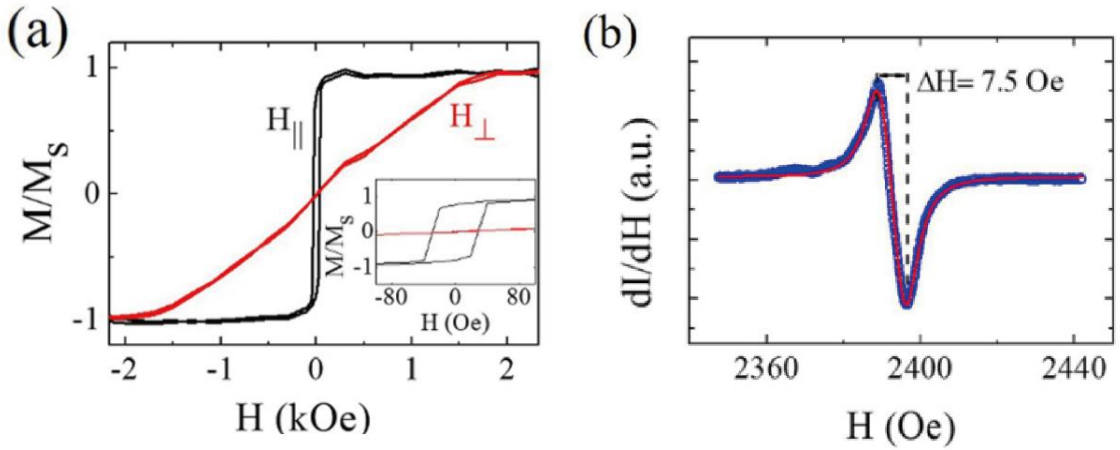

Figure 2-10. The magnetic properties of YIG film grown on GGG (110)/Pt (5 nm). (a) The magnetic hysteresis loop of YIG films with magnetic field applied in-plane and out-of-plane. Inset: in-plane hysteresis loop at low fields. (b) FMR absorption derivative spectrum of GGG/Pt/YIG at an excitation frequency of 9.32 GHz. Lorentzian fit (red line) shows a single peak with a peak-to-peak linewidth of 7.5 Oe, indicating a uniformity of high quality YIG films grown on Pt layer.

GGG's paramagnetic contribution has been removed by subtracting the linear background from the raw data. The easy axis of all YIG films with different thick-nesses lies in the film plane due to the dominant shape anisotropy. The coercivity falls in the range of 15–30 Oe for different thicknesses, which is larger than the typical value (0.2–5 Oe) for YIG films grown on lattice-matched GGG. The inset of Figure 2-10(a) shows a coercive field of 29 Oe for a 40 nm thick YIG film. The saturation magnetic field in the perpendicular direction is 1800 Oe, which corresponds well to $4\pi M_s$ for bulk YIG crystals (1780 Oe). FMR derivative absorption spectral of the inverted GGG/Pt/YIG at 9.32 GHz is shown in Figure 2-10(b). Form the Lorentzian fit, the peak-to-peak linewidth ΔH_{pp} is 7.5 Oe and the resonance field H_{res} is 2392 Oe. These values are comparable with the values for YIG epitaxially grown on GGG. The presence of Pt may bring additional damping from the interface spin pumping(*42, 43*) and therefore leads to a slight broadening of FMR linewidth.

The development of high quality single crystal YIG thin films grown on sputtered thin Pt film paves the way for the further investigation in magnon drag phenomenon in Pt/YIG/Pt trilayer structure(*60*). The excellent interface qualities has also been confirmed by observing the spin Hall magnetoresistance behavior and the spin Seebeck effect(*51*).

2.4. Robust Perpendicular Magnetic Anisotropy in Magnetic Insulator

2.4.1. Magnetic Anisotropy

The magnetic anisotropy and magnetostriction are the two basic phenomena which are present in each ferromagnetic material. The magnetic anisotropy aligns the magnetization to certain crystallographic directions. The magnetic moment of ferromagnetic materials will tend to align with an easy axis, which is an energetically favorable direction of spontaneous magnetization. In particular, in the demagnetized state, different configurations of the magnetization state can be observed(*49*). Different kinds of magnetic anisotropy can be distinguished according to their origins:

- Shape anisotropy: Certain distribution of magnetic charges, originating from the shape of magnetic specimen, produces a demagnetizing magnetic field with direction antiparallel to the magnetization.
- Magneto-crystalline anisotropy: Crystalline structures introduces preferential orientations of magnetization.

- Stress-induced anisotropy: The influence of strain affects the preferred directions of magnetization via the magnetoelastic effects.
- Others: Growth-induced anisotropy or exchange anisotropy(*49*).

2.4.2. Magnetostriction Induced PMA in Pure RIG

In modern magnetic insulator spintronics research, generating perpendicular magnetic anisotropy is of great importance in resolving critical physics conundrums and providing new functionalities in novel heterostructures. Most reported YIG epitaxial film has employed GGG substrates for their perfect lattice match and presents dominance of in-plane magnetic anisotropy. H. Wang *et al.*(*57*) has demonstrated a systematic strain tuning of magnetocrystalline anisotropy in epitaxial YIG films grown on lattice-mismatched $Y_3Al_5O_{12}$ (YAG) substrates. Although previous studies(*61, 62*) on YIG films indicated the existence of finite PMA due to stain, a systematic study of engineering robust PMA in garnet system is still lacking.

Here we leverage the lattice-mismatch induced strain in epitaxially grown films to generate a perpendicular surface anisotropy field $H_\perp$. When the surface anisotropy is sufficiently strong to overcome the shape anisotropy, a squared hysteresis loop is resulted. Along the <111> orientation of cubic crystals(*63*),

$$H_\perp = \frac{-4K_1 - 9\lambda_{111}\sigma_{||}}{3M_s}$$

where K_1, λ_{111}, $\sigma_{||}$, and M_s stand for the 1st-order cubic anisotropy, magnetostriction constant, in-plane stress, and saturation magnetization of the film, respectively. The value

of the in-plane stress is extracted from the lattice mismatch induced strain by taking into account the elastic deformation tensor(*64*):

$$\sigma_{\parallel} = 6C_{44}\frac{C_{11} + 2C_{12}}{C_{11} + 2C_{12} + 4C_{44}}\varepsilon_{\parallel}$$

where C_{ij} and $\varepsilon_{\parallel}$ are the elastic stiffness constants and in-plane strain. For rare earth iron garnets family, $C_{11} = 2.68 \times 10^{12}\ erg \cdot\ cm^{-3}$, $C_{12} = 2.68 \times 10^{12}\ erg \cdot\ cm^{-3}$ and $C_{14} = 2.68 \times 10^{12}\ erg \cdot\ cm^{-3}$. Or equivalently, the Young's modulus Y and Poisson's ratio μ gives(*49*):

$$\sigma_{\parallel} = \frac{Y}{1-\mu}\varepsilon_{\parallel}$$

where $= 2.0 \times 10^{12} dyn \cdot\ cm^{-2}$, $\mu = 0.29$.

The in-plane strain can be estimated from the relative difference between the lattice constant for the substrate a_s and film a_f, which gives:

$$\varepsilon_{\parallel} = \frac{a_s - a_f}{a_f}$$

Figure 2-11 shows a simplified picture of lattice deformation of RIG grown on different substrates. The positive in-plane strain $\varepsilon_{\parallel}$ with larger a_s than a_f gives rise to a tensile strain while the negative value of $\varepsilon_{\parallel}$ generates a compressive strain. The out-of-plane magnetic anisotropy field mainly depends on the product of the magnetostriction, either positive or negative for different garnets, and the in-plane strain. In most cases, the first term K_1 is negligible compared to the second term strain induced anisotropy. Robust PMA is obtained when the engineered perpendicular anisotropy field $H_{\perp}$ is larger than the demagnetizing field $4\pi M_s$.

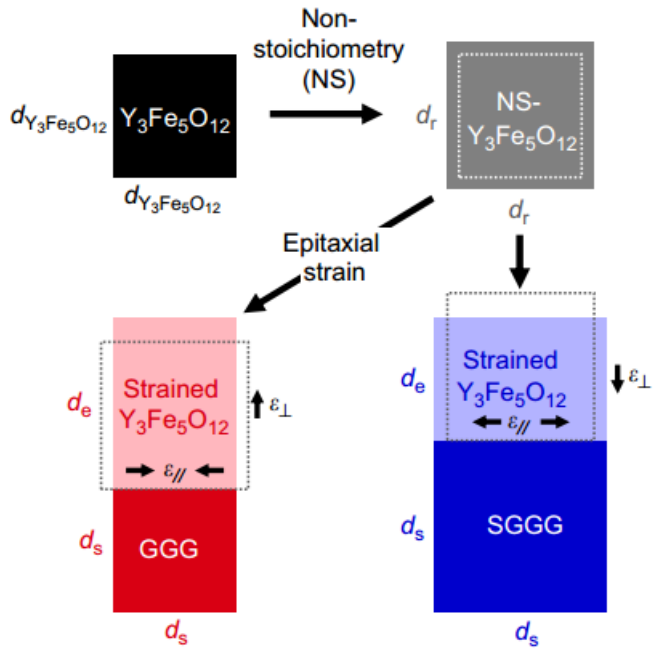

Figure 2-11. Schematic drawings of lattice deformation for YIG films grown on GGG and SGGG substrates. The lattices are depicted by assuming the epitaxial relation as a cube-on-cube structure for simplicity. The lattice mismatch for YIG on GGG and SGGG generates different strains at the interface. Adapted from M. Kubota *et al*. JMMM **339**, 63 (2013).

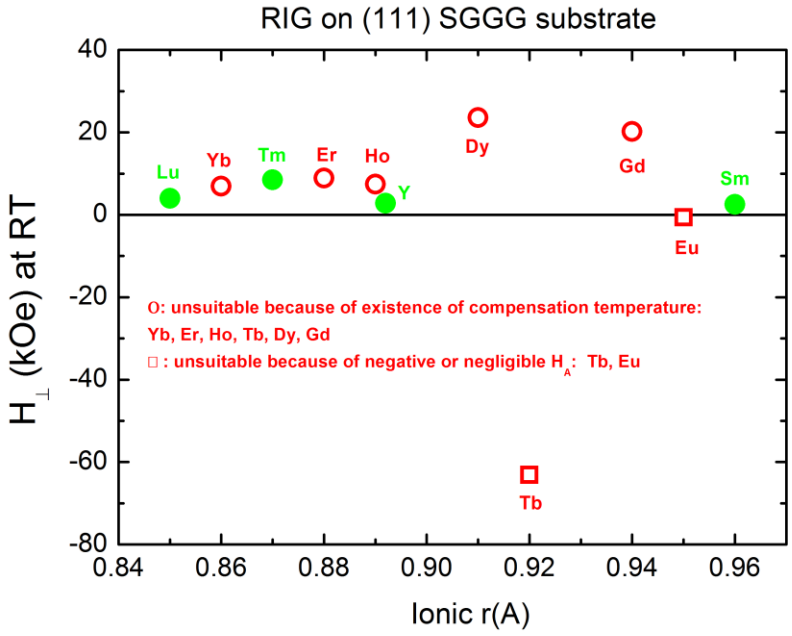

Figure 2-12. The theoretical calculation of the perpendicular magnetic anisotropy for different rare earth iron garnet family members on the (111) oriented SGGG substrates.

We first consider the engineering of robust PMA in the single rare earth element iron garnet without additional doping from other elements. Figure 2-12 explicitly shows the estimated $H_{\perp}$ at room temperature assuming a coherently strained pseudomorphic structure of RIG with single rare earth element on the (111) oriented SGGG for simplicity, without considering the other sources of magnetic anisotropy such as growth-induced magnetic anisotropy. In reality, the actual deformation of lattice structures could be much more complicated than this simplified scenario, resulting from the discrepancy(*58*) in the experimentally obtained and theoretically estimated $H_{\perp}$. We can safely rule out those RIG with negative $H_{\perp}$ which has stronger in-plane magnetic anisotropy. Note the RIG has compensation temperatures, at which the net magnetic moment vanishes. Therefore, those RIGs with compensation temperatures are less suitable for the further development of spintronics devices and have to be filtered out. The left four RIG are $Lu_3Fe_5O_{12}$, $Tm_3Fe_5O_{12}$, $Y_3Fe_5O_{12}$ and $Sm_3Fe_5O_{12}$. Among them, TIG has the largest $H_{\perp}$ resulting from a relative larger magnetostriction coefficient and considerable in-plane strain, and thus, we choose TIG grown on SGGG to maximize the tensile strain at the interface to obtain robust PMA.

	λ_{111} (10^{-6})	lattice constant (Å)	K_1 (10^{-3} erg·cm^{-3})	$4\pi M_s$ (G)	In-plane strain $\varepsilon_{\parallel}$ on GGG	In-plane strain $\varepsilon_{\parallel}$ on SGGG	$H_{\perp}$ on GGG (Oe)	$H_{\perp}$ on SGGG (Oe)
YIG	-2.4	12.376	-6.1	1780	0.06%	1.7%	139	2400
TIG	-5.2	12.324	-5.8	1393	0.48%	2.12%	1972	8485

Table 2-1. Detailed room temperature structural and magnetic parameters used to estimate the perpendicular magnetic anisotropy field in different combinations of magnetic garnets and substrates.

Further comparison of YIG and TIG on two substrates GGG (a = 12.383 Å) and SGGG (a = 12.585 Å) with detailed parameters is listed in Table 2-1. The nearly perfect lattice match between YIG and GGG only produces 0.06% strain at the interface leading to much smaller $H_\perp$ than the other three cases. A natural question coming to our mind is that whether all these three systems SGGG/YIG, GGG/TIG and SGGG/TIG would have robust PMA in the real magnetic films, as predicted by the theoretical calculations. The answer is no. The difficulty to acquire PMA and the degree of PMA robustness vary among the three systems. SGGG/TIG is the most robust PMA system among the three systems and the perpendicular magnetic anisotropy field $H_\perp$ always stays positive, nearly independent of growth environment (oxygen content) and thickness. The rest two need extreme conditionx, such as high oxygen content, to obtain larger $H_\perp$, as indicated by FMR and VSM measurements. The $H_\perp$ of these two systems is significantly smaller than that of SGGG/TIG.

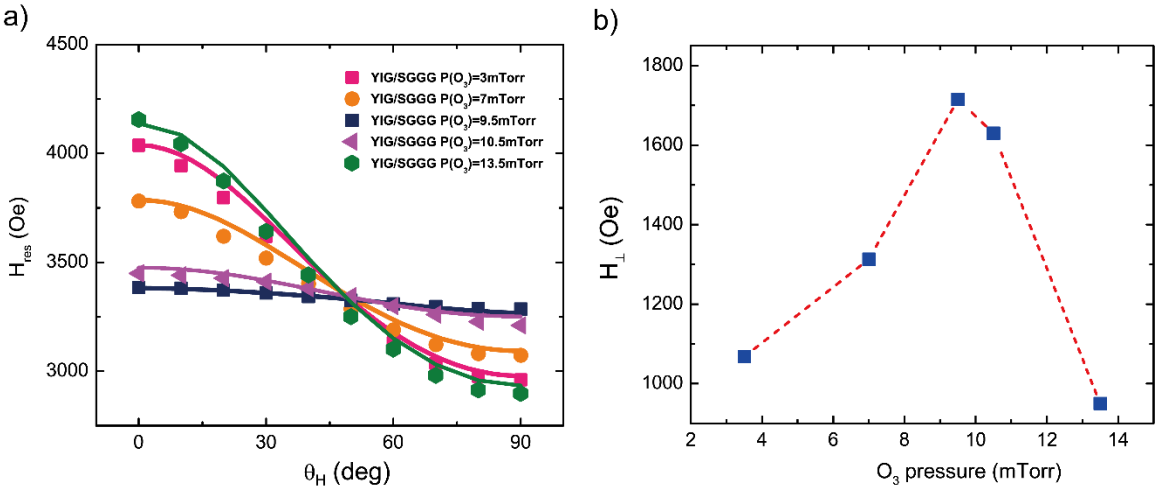

Figure 2-13. The oxygen content (with 12 wt% ozone) dependence of perpendicular magnetic anisotropy of YIG grown on SGGG. (a) The FMR resonance field H_{res} as a function of polar angle θ_H under different oxygen content. (b) The extracted perpendicular magnetic anisotropy field as a function of the oxygen pressure.

Figure 2-13 shows the investigation of PMA in 10 nm YIG thin films grown on SGGG under different oxygen contents (with 1 2 wt% ozone) using PLD deposition. Our standard oxygen content to grow high quality YIG films as shown in previous section is 1.5 - 3 mTorr. However, the extracted $H_{\perp}$ from FMR measurement is around 1078 Oe, smaller than the demagnetizing field $4\pi M_s$ under 3 mTorr oxygen content. With further increasing the oxygen pressure, $H_{\perp}$ first increases until reaching maximum value of 1715 Oe at 9.5 mTorr and then drops at higher oxygen pressure. Nevertheless, the peak value of $H_{\perp}$ in SGGG/YIG is still smaller than $4\pi M_s$ and therefore fails to obtain robust PMA under the growth condition in this study. The discrepancy between experimental and estimated $H_{\perp}$ may originate from the underestimation of the in-plane tensile stress based on the lattice constants of the two bulk crystals. Moreover, the increasing pressure of oxygen increases the roughness of YIG films, making this system less desirable in applications.

The TIG on GGG has the similar situation as YIG on GGG, with weak PMA induced from the interface strain, while TIG on SGGG shows robust PMA, nearly independent of the oxygen content. The PMA of TIG on SGGG persists up to 80 nm (thickest film we have tried), even though thicker films have weaker strain due to the relaxation of the magnetic films. Figure 2-14 shows the detailed structural and robust perpendicular magnetic properties of 10 nm TIG films grown on SGGG.

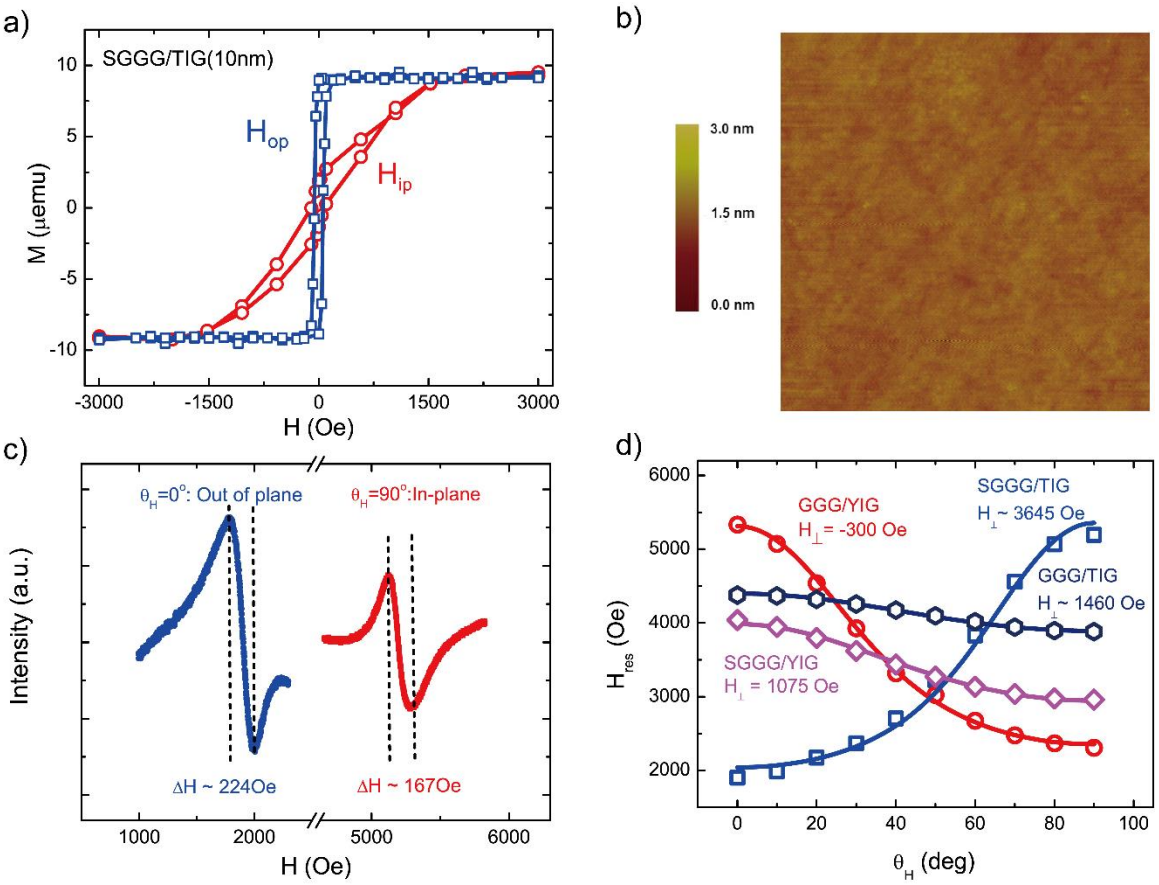

Figure 2-14. The structural and perpendicular magnetic properties of TIG films. (a) Magnetic hysteresis loops of 10 nm TIG film grown on SGGG (111) substrate for both field in-plane (ip) and out-of-plane (op) orientations showing perpendicular magnetic anisotropy. Linear paramagnetic background is removed. Inset: Magnetic hysteresis loops of 10 nm YIG film grown on GGG (111) substrate. (b) AFM surface morphology of TIG film with root mean square roughness of 0.14 nm. (c) FMR spectra of SGGG/TIG (10 nm) with field in-plane and out-of-plane orientations. θ_H is the angle of magnetic field with respect to the film normal. (d) Polar angle θ_H dependence of the resonance field H_{res} for GGG/YIG, SGGG/YIG, GGG/TIG, and SGGG/TIG bilayers. The fitting curves (solid) and the extracted perpendicular anisotropy fields are shown.

We first prepare our TIG PLD targets. Highly homogeneous and dense targets are fabricated through combination of a chemical precursor approach and the current activated and pressure assisted densification method(*65*). We have successfully grown atomically flat, epitaxial TIG thin films on (111)-oriented SGGG substrates by PLD system. The substrates are first cleaned with acetone followed by isopropyl alcohol and

deionized water. Prior to deposition, the substrates were annealed at moderate temperature ~200 $^{\circ}$C overnight in high vacuum at the level of 10^{-7} torr. After gradually increasing the substrate temperature to about 500 $^{\circ}$C and oxygen pressure with 12 wt% ozone to 1.5 mTorr, the KrF excimer laser pulses of 248 nm in wavelength with power of 150 mJ struck the target at a repetition frequency of 1 Hz. The deposition rate is estimated to be 0.5 Å/min. After deposition, the TIG films are rapid thermally annealed at 850 $^{\circ}$C for 5 minutes to get crystallized and acquire magnetism. The post-growth annealed TIG films exhibit strong PMA and ultra-flat surfaces, as shown in Figure 2-14. Figure 2-14(a) displays both in-plane and out-of-plane magnetic hysteresis loops of a typical 10 nm thick TIG film measured by a VSM. The out-of-plane hysteresis loop is squared while the in-plane hysteresis loop shows a hard-axis behavior. The in-plane saturation field H_{sat} is ~ 2000 Oe. From the spontaneous magnetic moment per unit cell (~2.8 μ_B at room temperature(*66*)) and the volume of the unit cell, $4\pi M_s$ is found to be ~1393 G. From $H_{\perp} = H_{sat} + 4\pi M_s$, $H_{\perp}$ is calculated to be 3393 Oe. Figure 2-14(b) is the AFM image of a representative TIG film. The RMS roughness over a 10 μm × 10 μm scanned area is ~ 1.4 Å. All samples with the same film thickness (10 nm) show similar rms roughness.

To further characterize the magnetic anisotropy, FMR study is carried out using a Bruker 9.3 GHz X-band EMX EPR spectrometer. A static magnetic field H is applied at an angle θ_H with respect to the film normal. Figure 2-14(c) displays the FMR spectra of a TIG film with H applied both parallel (θ_H=90°) and perpendicular to the film plane (θ_H=0°). The resonance field H_{res} is 1900 Oe and 5200 Oe, and the peak-to-peak

linewidth ΔH is 224 Oe and 167 Oe for field out-of-plane and in-plane, respectively. ΔH of the TIG thin film is much greater than that of YIG films or YIG crystals, but is comparable with that of TIG bulk single crystals (ΔH = 135 Oe(*67*)), which may be attributed to the intrinsic properties of the materials. Note that the out-of-plane H_{res} is smaller than the in-plane H_{res}, which is a qualitative indicator of PMA. The detailed polar angle dependence of H_{res} is summarized in Figure 2-14(d) for GGG/YIG, SGGG/YIG, GGG/TIG, and SGGG/TIG with different levels of tensile strain. The effective demagnetization field $4\pi M_{\mathrm{eff}} = 4\pi M_{\mathrm{s}} - H_{\perp}$ is extracted by fitting the resonance equation to the angular dependence of H_{res} and then $H_{\perp}$ is calculated to be -232 Oe, 1078 Oe, 1460 Oe, and 3645 Oe for GGG/YIG, SGGG/YIG, GGG/TIG, and SGGG/TIG, respectively. The $H_{\perp}$ value (3645 Oe) is the highest for SGGG/TIG which agrees well with what is obtained from magnetometer. In GGG/YIG, negative $H_{\perp}$ indicates in-plane anisotropy. The increasing trend of $H_{\perp}$ is correlated well with the increasing interface tensile strain, manifesting strain tunable PMA in rare earth iron garnet films. Future investigation on the mageneto-transport study on TIG based heterostructures will be discussed in the following chapters.

2.4.3. Strain Tunable PMA in Bi Doped YIG Films

In addition to the robust PMA in TIG films grown on tensile stressed SGGG substrates, we have also studied the strain tunable magnetic anisotropy effect in Bi doped YIG films(*65*), in which system the PMA is weaker but achievable by reducing the thickness of the magnetic films before getting relaxed. In $Bi_xY_{1-x}Fe_3O_{12}$ films(*68*), in the

regime where the Bi doping is light, it is found that an increasing Bi content *x*, results in a larger perpendicular lattice constant based on a homogeneous elastic compression because of the small lattice mismatch. However, in the regime of heavy doping of Bi ($x \geq 1.5$), the stress is accommodated by dislocations especially at elevated growth temperatures. Due to the thermal expansion difference between the film and substrate as the film is cooled back to room temperature, stress is built up at the interface at room temperature (region 2 in ref. 70**)**. The strained lattice constant, in such heavily Bi doped YIG is $a_{\perp} = a_o - \frac{2\mu}{1-\mu}\left(\alpha_f a_o - \alpha_s a_s\right)\Delta T$, where α_f and α_s are thermal expansion coefficient for the films and substrates, respectively and ΔT is the difference between growth and room temperature. In this case, the films are subjected to a tensile strain, owing to the larger coefficient for the $Bi_xY_{1-x}Fe_3O_{12}$ films ($\alpha_f > (10.4 + 0.83x)\times10^{-6}/$ ℃) than that of substrates ($\alpha_f(YAG) = 7.2\times10^{-6}/℃$). Therefore, in the large Bi-doping regime such as the x = 1.5 stoichiometry chosen here, it is promising to generate PMA in Bi:YIG films grown on YAG, thanks to the larger tensile strain.

High quality, ultraflat Bi:YIG thin films were grown on (111) oriented YAG substrates by PLD system using the CAPAD processed Bi:YIG targets, under similar condition as TIG films on SGGG. As shown in Figure 2-15(a), AFM analysis indicates atomically flat films with low roughness (~0.5 nm) and no pin holes were found on films. XRD of the 7 nm thick Bi:YIG thin film grown on YAG substrate shows the major YAG single crystal peak as expected, in addition to the Bi:YIG (444) peak, as indicated by Figure 2-15(b). In addition, the analysis reveals that the films contain no secondary phases.

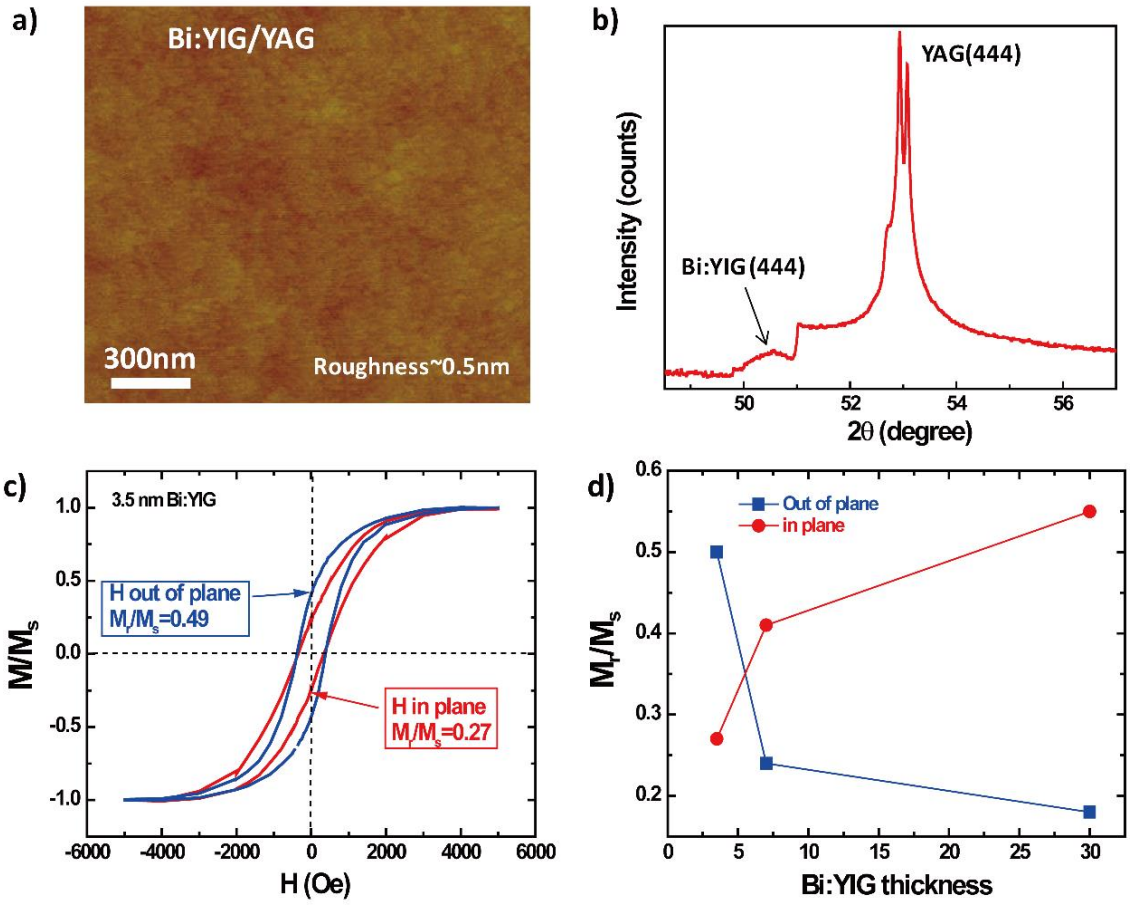

Figure 2-15. The structural and perpendicular magnetic properties of thin Bi:YIG films on YAG. (a) AFM surface profile for $Bi_{1.5}Y_{1.5}Fe_3O_{12}$ YIG film with a root-mean-square roughness about 0.5 nm across a 2 μm × 2 μm scan area. b) XRD pattern of the same Bi doped YIG films grown on YAG (111). c) Normalized magnetic hysteresis loops for both field out-of-plane and in-plane geometries of 3.5 nm $Bi_{1.5}Y_{1.5}Fe_3O_{12}$ film grown on (111) oriented YAG after removing the diamagnetic background of the substrates. Inset: Normalized magnetic hysteresis loops for both out-of-plane and in-plane geometries of undoped YIG films grown on (111) oriented YAG after removing the diamagnetic background of the substrates showing a strong in-plane anisotropy. d) The thickness dependence of the squareness for $Bi_{1.5}Y_{1.5}Fe_3O_{12}$ films on YAG for both in-plane and out-of-plane indicating the enhancement of perpendicular magnetic anisotropy for thinner films.

Magnetic properties of the Bi:YIG films are then measured using VSM and a Superconducting Quantum Interference Device (SQUID). Figure 2-15(c) shows the normalized magnetic hysteresis loop of 3.5 nm $Bi_{1.5}Y_{1.5}Fe_3O_{12}$ film grown on (111) oriented YAG for both field out of plane and in-plane geometries after removing the

diamagnetic background of the substrates. In contrast to the dominance of in-plane square loop of YIG films, the out-of-plane curve is comparable to the in-plane curve, clearly indicating an increase in PMA of the Bi:YIG film. In order to further confirm that increase in PMA is an interfacial induced effect, we conducted a thickness dependence study. Figure 2-15(d) shows the Bi:YIG thickness dependence of the squareness of magnetic hysteresis loops defined as the ratio of remanence M_r over saturation magnetization M_s for both in-plane and out of plane. A strong enhancement of the squareness for out of plane and suppression of squareness for in-plane when Bi:YIG films become thinner suggests the increase of PMA is caused by the interfacial strain. The perpendicular magnetic anisotropy increases with a decrease in film thickness and overwhelms the shape anisotropy at a thickness of 3.5 nm.

In summary we have developed an exquisite control of high quality rare earth iron garnets ferromagnetic insulator thin films with ultra-smooth surface and superb magnetic properties. Robust perpendicular magnetic anisotropy is successfully engineered in TIG films grown on SGGG. The Bi:YIG shows systematic strain tunable PMA by reducing the film thickness. The materials development of high quality magnetic insulators laid solid foundation for the future magnetic insulator based spintronics research.

Chapter 3

Spin Transport of Magnetic Insulator Based Heterostructures

3.1. Introduction

The heterostructures of a strong SOC system proximity coupled with a magnetic insulator exhibit a variety of interesting spin current related phenomena, such as spin pumping, SSE, SMR, MPE, SOT, etc. The unique properties of magnetic insulator, such as YIG, including long spin wave propagation length, less energy dissipation free from Joule heating by charge carriers and zero current shunting as a perfect insulator, leads to a perfect candidate for harvesting energy more efficiently in nanoscale spintronics devices.

There are two essential issues that will be addressed in this chapter. The first one is the interfacial exchange coupling between the magnetic insulator and non-magnetic high SOC material that introduces magnetism without adding additional disorders. The heterostructure approach to introduce ferromagnetic ordering into non-magnetic material is of great significance in the fundamental spintronics research. For example, this approach is demonstrated to drastically raise the Curie temperature T_c of a magnetic insulator and therefore greatly increase the exchange-induced gap, to ultimately to realize QAHE at elevated temperatures, with dissipationless edge transport. The second one is the spin current dominated transport in the magnetic insulator based heterostructures. Generally, spin current can be generated via SHE as a consequence of SOC in the non-magnetic conducting material, which gives rise to the magnetization dynamics in the

magnetic insulator layer by transferring angular momentum at the interface and reciprocally an electrical response is triggered in the conduction layer. Such spin current mediated transport phenomena include SMR, SOT, spin pumping, magnon-mediated drag, etc. The following sections will discuss the two issues in more details.

3.2. Magneto-transport in Iron Garnet/Heavy Metal Bilayers7

3.2.1. Overview of the History

Spin Seebeck effect has demonstrated to generate pure spin current by applying a temperature gradient across a magnetic metal(*22*), semiconductor(*23*) and insulator(*24*). It has attracted a great deal of attention and considered as the beginning of the spin caloritronics discipline, which focuses on the interactions of spins with heat currents and utilizes novel strategies to improve existing thermoelectric effects. However, the SSE in insulators is particularly challenged by a possible MPE(*26*) existing at the magnetic insulator/non-magnetic material interface which causes a possible anomalous Nernst effect (ANE) in the magnetized conductor layer that can generate SSE-like signal. The MPE was first demonstrated in the YIG/Pt bilayer by observing AMR and AHE-like signal(*26*) in 2012 and was soon confirmed in other systems such as YIG/Pd(*69*) and YIG/Ta(*70*). Detailed study of the induced magneto-transport behavior will be discussed later. Strong evidence that shows the SSE originating from spin current and free from the extrinsic ANE(*27*) was provided soon after. By reporting the longitudinal geometry of SSE in YIG/Au and YIG/Cu/Pt where proximity ANE is clearly removed, spin current is

found to be the origin of SSE. Additionally, the SMR(*45, 71*) interprets the magnetoresistance behavior observed in YIG/heavy metal (HM) bilayers as concerted actions of SHE and ISHE at the interface, originating from the absorption of spin current when spin polarization of the spin current is non-collinear with the magnetization of the magnetic insulator. Both mechanisms are proved to exist and are responsible for the emerging novel transport phenomena in the magnetic insulator based heterostructures. Since the discovery of emerging magneto-transport phenomena in the magnetic insulator based heterostructures, the surge of magnetic insulator based spintronics research has started and made an increasingly important impact on the development of fundamental condensed matter physics. Systematical study of the magneto-transport behaviors in iron garnet based heterostructures will be discussed.

3.2.2. Induced Magneto-transport at YIG/Pd Interface

Noble metals such as Pt and Au are preferred spin current generators or detectors due to their strong spin-orbit interaction that results in a large spin Hall effect which is often described by a large spin Hall angle $\theta_{SH} = \sigma_{xy}/\sigma_{xx}$ (*72, 73*). The large room-temperature spin Hall effect quantified by the spin Hall angle is important for spintronics. Motivated by the early debate whether the SSE is possibly caused by a MPE induced extrinsic ANE at the interface of YIG/Pt(*26*) and YIG/Au(*27*). First of all, Pd is a 4d transition metal and has large magnetic susceptibility which favors MPE. It was shown that MPE does exist at ferromagnetic metal/Pd interfaces(*74*). In addition, Pd also has strong spin-orbit interaction and been shown to have a large spin Hall conductivity(*75*).

To address the issue of possible MPE in magnetic insulator-based structures, we choose YIG/Pd as our main material system.

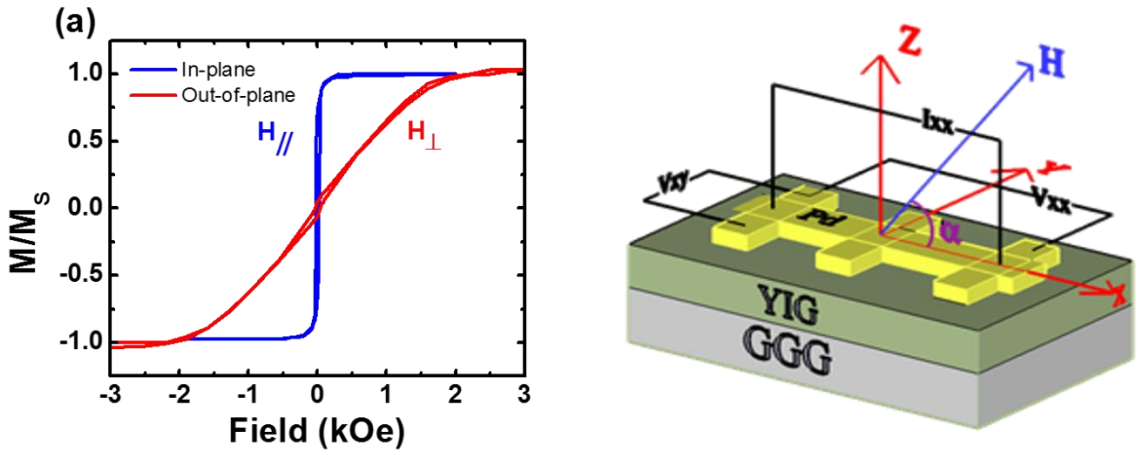

Figure 3-1. The magnetic hysteresis of YIG/Pd and schematic drawing of device setup. (a) Normalized magnetic hysteresis loops at 300 K of YIG film on GGG (111) substrate with an applied field in-plane ($H_{\parallel}$) and out-of-plane ($H_{\perp}$). (b) Schematic diagram of the patterned Hall bar.

YIG films are grown on single crystal GGG substrates using a PLD system under the same recipe described in chapter 2. Typical magnetic hysteresis loops are shown in Figure 3-1(a). The out-of-plane saturation field is ~ 2 kOe, which corresponds well to $4\pi M_s$ = 1780 G for YIG. After YIG films are taken out of the PLD chamber, they are immediately placed in a high-vacuum sputtering chamber where a thin Pd film is deposited. Before deposition, YIG film is lightly sputtered to provide a fresh and clean surface. In this work, we focus on Pd films with a thickness range from 1.5 to 10 nm. Hall bars with the width of 200 μm and length of 1000 μm are patterned using ion milling. The magnetic properties of YIG films are measured with either a vibrating sample magnetometer or Quantum Design's magnetic property measurement system. The magneto-transport measurements are conducted in either a close-cycled refrigerator with

an electromagnet (<1 T) or Quantum Design's physical property measurement system (up to 14 T).

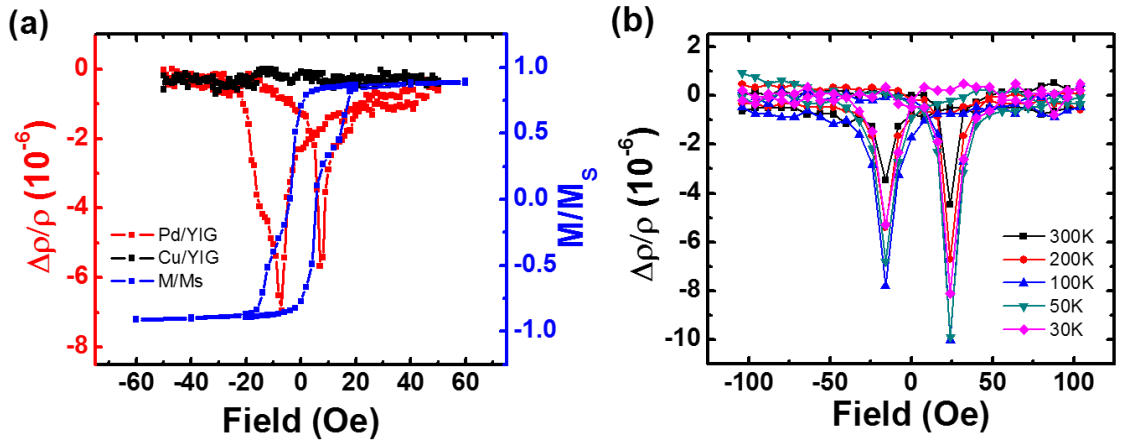

Figure 3-2. The anisotropic magnetoresistance of YIG/Pd. (a) In-plane low-field MR of YIG Pd (2 nm) (red squares), MR of YIG/Cu reference sample (black squares), and in-plane hysteresis loop (blue squares). (b) Temperature dependence of MR ratio of YIG/Pd (2 nm).

As an in-plane magnetic field $H_{//}$ is swept along the Hall bar direction, the magnetoresistance (MR), $\frac{\Delta\rho}{\rho} = \frac{\rho(H)-\rho(0)}{\rho(0)}$, of a YIG/Pd (2 nm) is shown in Figure 3-2(a), along with the magnetization data of YIG. Two negative peaks appear at the coercive fields of YIG. This feature resembles the anisotropic MR effect in ferromagnets. Here the MR peak is only ~ $6\text{x}10^{-6}$, several orders smaller than that of the anisotropic MR in ferromagnetic conductors. MR with similar magnitude was previously reported in Pt/YIG where the YIG films are polycrystalline(*26*). For comparison, a 2 nm thick Cu film deposited on YIG does not show any measurable MR signal. One possible cause of MR in Pd film is that the non-magnetic Pd film acquires a magnetic moment whose direction is dictated by the underlying YIG film, i.e. the Pd interface layer adjacent to YIG acting as if it is magnetic. As shown in Figure 3-2(b), the MR peaks are correlated with the

coercive fields of YIG which do not change significantly with the temperature in this temperature range. However, the MR peak nearly doubles when the temperature is lowered to 30 K, which is consistent with reduced spin-flip scattering.

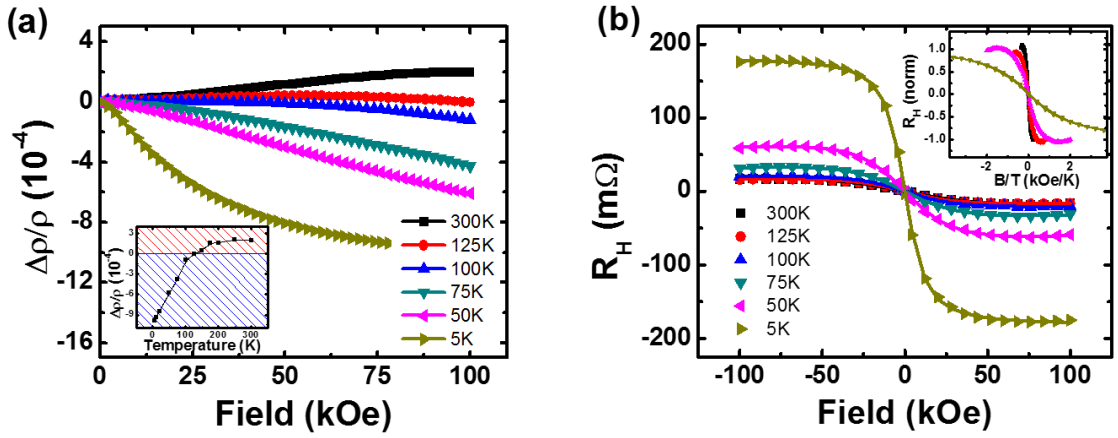

Figure 3-3. The high field anisotropic magnetoresistance and anomalous Hall effect in YIG/Pd at different temperatures. (a) Out-of-plane HFMR at different temperatures. The inset shows MR ratio at H=10 kOe. Red and blue regions represent positive and negative MR ratios respectively. (b) Field dependence of the Hall resistance R_H at different temperatures with linear background removal. Lines are the Brillouin function fits. Inset: Normalized R_H as a function of B/T shows that "gJ" changes as temperature is varied.

We have extended MR measurements to high fields. Figure 3-3(a) shows MR of the same YIG/Pd sample with the field perpendicular to the film, $H_\perp$. Surprisingly, there is a much larger high-field magnetoresistance (HFMR) background that is overwhelmingly larger than the low-field MR signal shown in Figure 3-2. At high temperatures, the positive MR is probably the usual Lorentz force induced effect. As the temperature is lowered, this positive MR diminishes and turns to negative. Negative MR is usually seen in materials with random spins that can be aligned by an external field to cause suppressed scattering. At the lowest temperature, the HFMR ratio reaches ~ -10^{-3}, nearly two orders greater than that of MR at low fields. The comparison between the low-

and high-field MR reveals that in addition to the low-field phenomenon related to the YIG magnetization reversal, there is some spin-dependent process occurring at high fields. When additional spins are aligned with high fields, the MR ratio is consequently enhanced. It is interesting that the temperature dependence of HFMR (inset of Figure 3-3(a)) is markedly different from that of the low-field MR.

In ferromagnetic conductors, superimposed on the ordinary Hall effect that is linear in $H_\perp$, there is a large AHE signal that is proportional to the out-of-plane magnetization component. However, in the low field range (up to ~2 kOe) where the in-plane magnetization is rotated towards the perpendicular direction and therefore there should be an AHE response, we do not observe any definitive magnetization-related AHE signal. As we ramp up $H_\perp$ further, however, an unambiguous non-linear AHE-like signal arises on the linear ordinary Hall background (removed in Figure 3-3(b)). At low temperatures, there is a clear saturation in Hall resistivity at the highest magnetic field. The Hall resistivity reaches ~0.17 Ω at 5 K, equivalent to ~$1\text{x}10^{-3}$ in the Hall angle. Note that the YIG magnetization saturates only with $H_\perp$ ~ 2 kOe, but saturation of the AHE-like signal does not occur until $H_\perp$ > 20 kOe. Therefore, similar to the HFMR effect, the high-field Hall signal also reveals a response of the magnetic moments other than those in the Pd interface layer that are possibly exchange aligned to the YIG magnetization. We fit the Brillouin function, i.e.

$$B_J(x) = \frac{2J+1}{2J}\coth\left(\frac{2J+1}{2J}x\right) - \frac{1}{2J}\coth\left(\frac{1}{2J}x\right);\ x = \frac{g\mu_B JB}{k_B T}$$

to the AHE-like data in Figure 3-3(b). Here T is the temperature, μ_B is the Bohr magneton, and gJ is treated as a fitting parameter. The solid curves in Figure 3-3(b) are the actual Brillouin fits. Clearly, the saturation AHE-like signal steadily increases at low temperatures. The inset shows a plot of the normalized AHE-like signal as a function of B/T, indicating that the effective magnetic moment is not a temperature-independent constant. "gJ" decreases from ~ 200 μ_B at room temperature to ~ 7 μ_B at 5 K. It is known that a Fe impurity can induce a large local moment of in Pd(*76*, *77*); however, its temperature dependence has not yet been reported or understood.

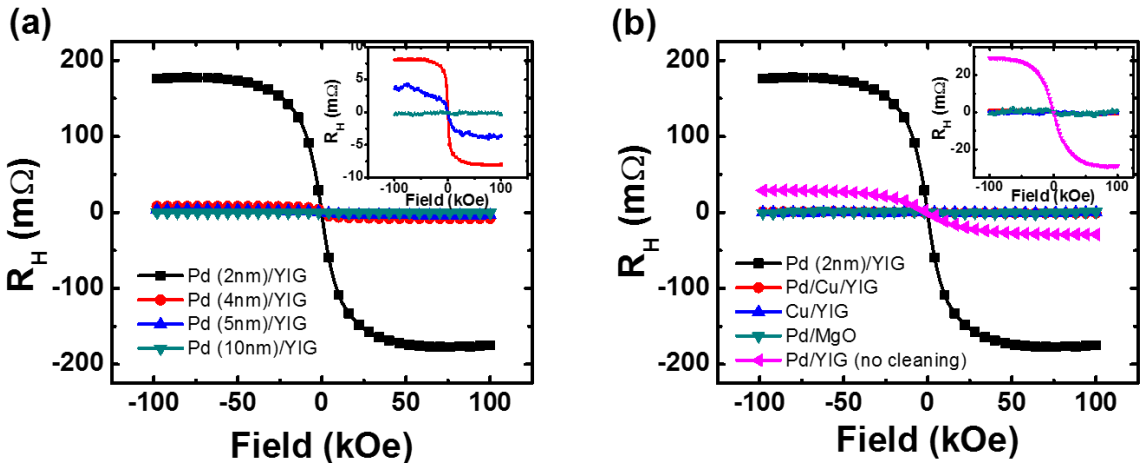

Figure 3-4. The high field anomalous Hall effect for different thicknesses of Pd and other control samples. (a) Pd thickness dependence of the Hall resistance R_H at T=5 K. The inset shows the zoom-in data for Pd thicknesses from 4 to 10 nm. (b) R_H for several reference samples at T=5 K. All metal layers (except the Cu-layer in Pd/Cu/YIG) are 2 nm thick. The inset shows zoom-in data for reference samples.

Figure 3-4(a) shows the Pd thickness dependence of the AHE-like signal in YIG/Pd samples. As the Pd thickness increases, the Hall magnitude sharply decreases. The inset shows the zoom-in plot of the AHE-like data for 4, 5, and 10 nm thick Pd films at room temperature. For 10 nm thick Pd, the Hall signal essentially vanishes. The rapidly

decreasing trend of the AHE-like signal clearly demonstrates the interfacial origin of the magnetic moments that are responsible for the high-field Hall effect. Since the moments are located at the interface and it is the interface layer that produces a Hall signal, when the film thickness is much greater than the interface layer, the measured Hall voltage is quickly reduced due to the parallel resistance of the bulk Pd layer. For the same nominal 2 nm thick Pd on YIG, we have observed AHE with similar magnitude in five different samples.

Figure 3-4(b) further reveals the properties of the interface moments. First of all, Pd needs to be in direct contact with YIG. Pd on MgO does not produce any Hall signal; therefore, the source of the interface moments must be YIG. Second, Cu either has no interface moments or does not produce any Hall signal even if it has interface moments. We cannot distinguish these two possibilities. If the latter is true, a 6 nm thick Cu layer is sufficiently thicker than the mean-free-path so that Pd does not feel any effect from the magnetic moments at the YIG/Cu interface. Third, interface roughness seems to enhance the Hall signal. The sputter cleaned YIG surface is likely rougher than the one without sputter cleaning and the Hall magnitude is a factor of 5 larger in the sample with a rough interface.

The above experimental facts strongly suggest that independent magnetic moments producing the high-field effects originate from the YIG/Pd interface. On the other hand, those moments are not exchange coupled to the YIG spins. In ferromagnetic conductors, the carriers are spin polarized and AHE arises from either extrinsic or intrinsic mechanisms due to spin-orbit interaction. But the existence of an AHE-like

signal does not prove ferromagnetism. In the framework of AHE, the magnitude of AHE, ρ_{xy}, scales with the resistivity, ρ_{xx}, either linearly or quadratically, i.e. $\rho_{xy} \sim \rho_{xx}^{n}$, with n=1 or 2, depending on the microscopic mechanism(*8*). In our YIG/Pd, the resistivity changes only ~ 18% but the AHE-like signal rises by a factor of 10 below 100 K. We do not expect any sharp temperature dependence of the saturation or fully aligned magnetic moments. Therefore, the dramatic rise of measured AHE-like signal at low temperatures argues against the AHE mechanism for spin-polarized carriers as in regular ferromagnets. Similar high-field effects were previously found in noble metal-based dilute magnetic alloys where the local moments can cause a left-right asymmetry to unpolarized electrons(*78-80*). The Hall angle can be as large as 10^{-3} to 10^{-2}. Either the spin-orbit interaction or spin-spin exchange between the local moments and the conduction electrons can result in such a Hall angle. The former is called the skew scattering(*78*) and the latter the "spin effect"(*81*). The "spin effect" causes an enhanced ordinary Hall signal and MR, both of which vary with $<S_z>^2$, and therefore have a zero initial slope at H =0. This disagrees with our observations. Our experimental data in YIG/Pd are consistent with the skew scattering picture in which unpolarized electrons are deflected by local moments via spin-orbit interaction, similar to the noble metal-based dilute magnetic alloys(*82*). We should point out that YIG/Pt samples also exhibit similar characteristic high-field features as observed in YIG/Pd but with larger magnitude in the Hall signals.

3.2.3. Experimental Investigation of Magnetoresistance Effects in YIG/Pd

In the hybrid structures of a magnetic insulators and a heavy metal, the magneto-transport behavior can also originate from the SMR(*45*). According to the SMR mechanisms, the spin current generated by the spin Hall effect in the SOC metal is reflected from the interface, and then converted into a charge voltage by the SOC metal. In a sweeping in-plane magnetic field, SMR behaves like the conventional AMR in ferromagnetic conductors(*83*), a phenomenon arising from a completely different origin. SMR is a pure spin current phenomenon in such bilayer structures; whereas AMR can only originate from the proximity effect induced ferromagnetism in the SOC metal at the interface(*26*). In reality, both possibilities may be present but may not be revealed at room temperature.

By setting the magnetization of YIG to different orientations, one can determine the anisotropic resistivities in all three orthogonal directions of the SOC metal, i.e. longitudinal $\rho_{\parallel}$, transverse ρ_T, and perpendicular $\rho_{\perp}$ resistivities, where $\rho_{\parallel}$ represents the resistivity when the magnetization $\boldsymbol{M}$ is parallel to the current direction, and both ρ_T and $\rho_{\perp}$ are the resistivities when $\boldsymbol{M}$ is perpendicular to the current direction, but for the former, $\boldsymbol{M}$ lies in the film plane and for the latter $\boldsymbol{M}$ is perpendicular to the plane. In ferromagnetic metals, it is often found $\rho_{\parallel} > \rho_T \approx \rho_{\perp}$, which is the conventional AMR. However, in YIG/Pt bilayers, it was found that $\rho_{\parallel} \approx \rho_T \neq \rho_{\perp}$ at room temperature(*45, 84*), a property not consistent with AMR. This raises a question about the nature of this room-temperature magnetoresistance effect.

Both SMR and AMR effects are interface phenomena; consequently, they critically depend on the quality of the interface and SOC metals. For example, since the SMR effect vanishes as the SOC metal thickness exceeds the spin diffusion length (i.e. λ ~ 1.5 nm for Pt at room temperature(*85*)), the thickness variation of the SOC metal needs to be much smaller than this length scale. We have demonstrated the epitaxial growth of atomically flat YIG films with our PLD as well as the deposition of a smooth Pd layer down to 1.5 nm with sputtering which are suitable for this investigation. Furthermore, for chosen Pd thicknesses, we vary the sample temperature so that λ can be tuned continuously across the sample thickness and the effect of spin current is revealed. In addition, if the proximity induced ferromagnetism exists in SOC metals, the AMR effect becomes more pronounced at lower temperatures. AMR originates from different scattering rates between the current parallel to and perpendicular to the magnetization or the ferromagnetic spin directions. At high temperatures, the spin-dependent effect is diluted by spin-independent scattering events such as electron-phonon scattering. Hence, we expect the AMR effect to appear and increase monotonically as the temperatures is decreased.

Magnetoresistance of a YIG/Pd (2 nm) bilayer in an in-plane magnetic field shows low-field peaks (dips) located at the coercive fields of YIG(*69*). This feature is similar to the AMR effect in polycrystalline ferromagnetic materials, but an alternative possibility is SMR. According to the SMR theory(*71*), a charge current flowing along the x-direction as shown in Figure 3-5(a) generates a y-polarized spin current, $\boldsymbol{j}_s$, flowing along the z-direction. Depending on the orientation of $\boldsymbol{M}$ with respect to the spin

direction of $\boldsymbol{j_s}$, the reflected spin current varies in magnitude, which yields an additional ISHE voltage superimposed on the longitudinal voltage signal. It has been shown that the resulting SMR is

$$\frac{\Delta\rho}{\rho} \sim \frac{\Delta\rho_1}{\rho}(1 - m_y^2) \quad (1)$$

$$\frac{\Delta\rho_1}{\rho} = \theta_{SH}^2 \frac{\lambda}{d} \frac{2\lambda G_r tanh^2(\frac{d}{2\lambda})}{\sigma + 2\lambda G_r coth(\frac{d}{2\lambda})}, \quad (2)$$

where m_y is the y-component of the magnetization unit vector, and $\frac{\Delta\rho_1}{\rho}$ depends on λ, metal film thickness d, electrical conductivity of the metal film σ, spin Hall angle θ_{SH}, and the real-part of the spin-mixing conductance G_r, as shown in Eq. 2. Clearly, the in-plane field sweep cannot distinguish AMR from SMR since both depend on the orientation of $\boldsymbol{M}$ in the xy-plane. By rotating $\boldsymbol{M}$ in specific planes, however, it is possible to distinguish these two effects. Figure 3-5(a), if $\boldsymbol{M}$ is rotated in the xz-plane tracked by angle α, SMR should remain constant, since m_y, and therefore, the reflection of $\boldsymbol{j_s}$ is unchanged; any resistance change can be attributed to AMR. On the other hand, if $\boldsymbol{M}$ is rotated in the yz-plane tracked by angle β, AMR should remain constant, since the charge current is always perpendicular to $\boldsymbol{M}$; any resistance change can be attributed to SMR. In these two cases, magnetoresistance reveals different physical mechanisms. If $\boldsymbol{M}$ is rotated in the xy-plane tracked by angle γ, however, both SMR and AMR change simultaneously and therefore the two effects are entangled.

A magnetic field of 10 kOe is sufficiently strong to align and rotate the YIG magnetization $\boldsymbol{M}$ in any direction. Figure 3-5(b) shows a comparison of the relative changes of measured resistivity, $\frac{\Delta\rho}{\rho_0}$, at 100 K and 3 K as a 10 kOe magnetic field is rotated

in three orthogonal planes. For the α- and β-sweeps, 90° is chosen as the reference angle for calculating $\Delta\rho$, i.e. $\Delta\rho = \rho\ (\alpha) - \rho\ (\alpha = 90^{\circ})$ and $\Delta\rho = \rho\ (\beta) - \rho\ (\beta = 90^{\circ})$, since α =90° and β = 90° coincide.

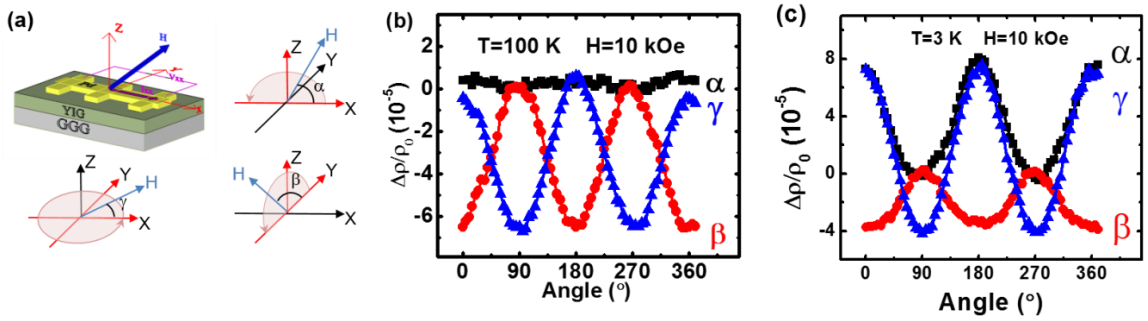

Figure 3-5. The schematic illustration and experimental data of the angle dependent MR measurement. (a) Schematic diagram of the patterned Hall bar and notations for different field rotations. (b) and (c) show typical field rotation magnetoresistance data with H=10 kOe in three orthogonal planes for YIG (30 nm)/Pd (2nm) at 100 K (b) and 3 K (c).

For the γ -sweep, 0° is chosen as the reference. ρ_0 is the resistivity at zero magnetic field. In all sweeps, the resistivity is a periodic function of the rotating angle with a period of 180°. To eliminate any mixed Hall signal that has a period of 360° due to any possible accidental misalignment of the longitudinal resistivity electrodes, we have removed a small background signal with a period of 360°. This background accounts for less than 10% of the total signal in the worst cases. At 100 K, the α -sweep only shows very small amplitude, indicating a negligible AMR effect, i.e. $\rho_{\parallel} = \rho_{\perp}$. The amplitude of the γ -sweep (~6%) corresponds well to that of the β -sweep except that they are out of phase from each other. This is expected from Eq. 1 because the same m_y change is responsible for the SMR in the β -sweep as well as the AMR in the α -sweep. At 3 K, all three sweeps register large amplitudes. This is in stark contrast with the room temperature or 100 K

data which shows a nearly vanishing AMR effect. We also note that the amplitude of the β -sweep is smaller than that at 100 K, indicating a non-monotonic trend. The comparison at these two temperatures suggests different temperature dependence between SMR and AMR.

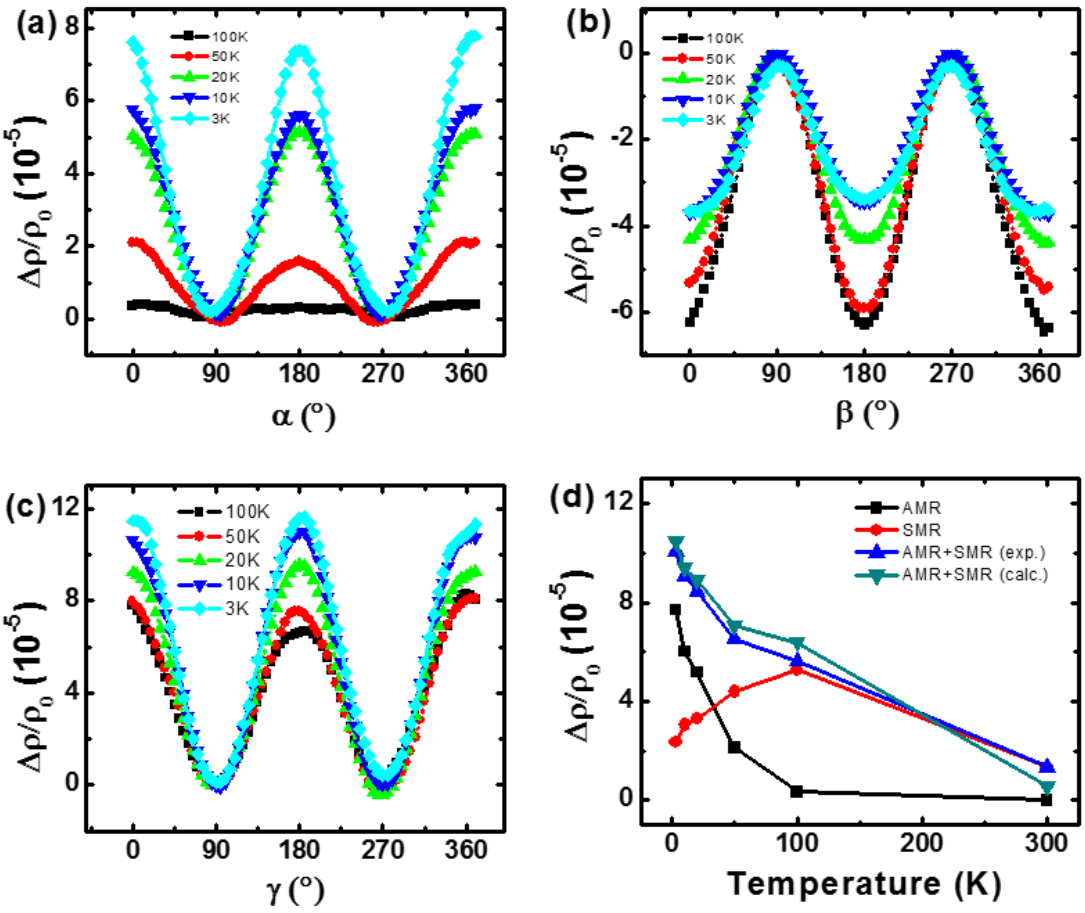

Figure 3-6. The field rotation of MR in xy, yz and xz planes for YIG/Pd bilayers. (a) Magnetoresistance data for YIG (30 nm)/Pd (2nm) with H=10 kOe at different temperatures for xz-sweeps (a); xy-sweeps (b); and yz-sweeps (c). (d) Temperature dependence of the magnetoresistance oscillation amplitude in all three rotational configurations. xz-, yz- and xy -sweeps represent AMR, SMR, and AMR+SMR, respectively. "AMR+SMR (exp.)" is the amplitude of the magnetoresistance oscillations measured in the xy–sweep, and "AMR+SMR (calc.)" is the sum of two amplitudes in the xz- and yz-sweeps.

To find the detailed temperature dependence of these two effects, we have carried out the measurements over a range of temperatures on this 2 nm Pd sample. Figure 3-6(a), 3-6(b), and 3-6(c) show the anisotropic resistivities in all three sweeps. At all temperatures, $\frac{\Delta\rho}{\rho_0}$ oscillations can be well described by,

$$\frac{\Delta\rho}{\rho_0} = \frac{\rho_{\parallel}-\rho_{\perp}}{\rho_0} cos^2\alpha, \frac{\Delta\rho}{\rho_0} = -\frac{\rho_{\perp}-\rho_T}{\rho_0} cos^2\beta, \text{ and } \frac{\Delta\rho}{\rho_0} = \frac{\rho_{\parallel}-\rho_T}{\rho_0} cos^2\gamma. \quad (3)$$

From those data, we immediately have$\rho_{\parallel} > \rho_{\perp} > \rho_T$ at low temperatures. Figure 3-6(d) plots the temperature dependence of the resistance oscillation amplitude for all three sweeps. Clearly, the α- and β-sweeps have distinctly different temperature dependences. Above a certain temperature (~100 K), the amplitude of the α-sweep or AMR is negligibly small. As the temperature is decreased to below 100 K, AMR starts to appear and increases steadily. On contrary, the amplitude of the β-sweep or SMR has a peak at ~ 100 K. The overall temperature dependence of SMR is expected from the SMR theory as will be discussed below. From Eq. 3, it is clear that the amplitude of the γ-sweep should be just the sum of those of the α- and β-sweeps if $\boldsymbol{M}$ rotates as a single-domain magnetization. Indeed, the sum calculated from the two temperature-dependent amplitudes of the α- and β-sweeps agrees well with the amplitude of the γ-sweep measured separately, as shown in Figure 3-6(d).

The unique peak in the β-sweep is consistent with the SMR theory prediction. In Eq. 2, the magnitude of SMR depends on the d/λ ratio. As the temperature is decreased, the spin Hall angle, the electrical conductivity, and the spin mixing conductivity of Pd will likely change somewhat, but we do not expect that they change significantly or in a

non-monotonic way. On the other hand, d/λ can change over a large range as the temperature is varied, which causes the right-hand-side of Eq. 2 to change non-monotonically. In fact, if we assume that SMR is a function of d/λ, as it varies, a SMR peak occurs at d/λ ~0.8 according to Eq. 2, as shown in the inset of Figure 3-19. Although the actual position of the peak may not exactly coincide at this value, a peak in SMR is expected to appear at d~ λ from the following general argument. If the spin diffusion length is much smaller than the film thickness, SMR obviously vanishes. On the other hand, if the spin diffusion length is much greater than the film thickness, then the chemical potential difference between spin-up and –down channels does not vary much across the film thickness, which consequently results in a small spin current and SMR. AMR, on contrary, is expected to increase at low temperatures as discussed earlier. Therefore, the characteristic temperature dependence provides us an important criterion to distinguish SMR from AMR. To demonstrate the thickness effect, we have prepared samples with three different Pd thicknesses: 2, 3, and 4 nm, on YIG films grown under nominally the same conditions. The results are displayed in Figure 3-7. Clearly, the SMR peak position (~ 100 K) of the 2 nm sample agrees with the data shown in Figure 3-18 from the other 2 nm sample. Using the SMR theory prediction, we can estimate the spin diffusion length of Pd at 100 K by $\lambda = 1.25d$, which yields λ ~ 2.5 nm. We note that the detailed peak width differs, which is likely due to the inevitable roughness of Pd. The SMR of the 3 nm sample also shows a well-defined peak that is located at a lower temperature (~ 50 K). This trend is in qualitative agreement with the SMR theory, and it implies that λ is increased to ~ 3.8 nm at 50 K. For the 4 nm sample, the peak is not

captured in the temperature window of our experiments (2 to 300 K). However, the trend for the SMR peak position is in good agreement with the theoretical prediction. We note that the previously determined λ value spreads from 2 to 9 nm at room temperature(*86, 87*) and is as large as 25 nm at 4.2 K(*88*). The discrepancy may arise from the differences in the measurement techniques or in sample conditions.

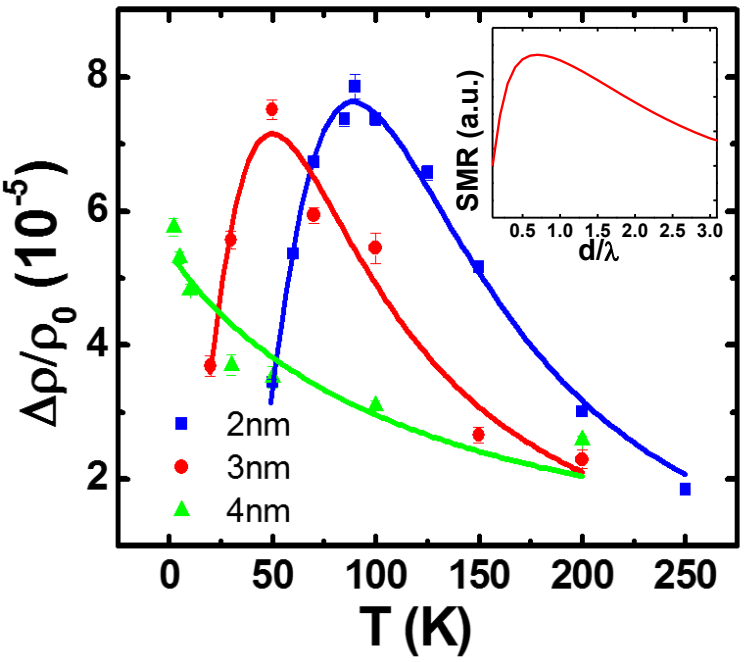

Figure 3-7. SMR measured in the yz -sweep as a function of temperatures for three different Pd layer thicknesses: 2, 3, and 4 nm. Inset: SMR vs. d/λ calculated using Eq. 2.

In summary, unlike SMR, the AMR magnitude is larger at lower temperatures in all samples, which confirms different physical mechanisms behind these two effects. The fact that AMR exists at low temperatures implies the existence of proximity induced ferromagnetism in Pd near the interface. By lowering the temperature, we observe an enhanced AMR as a result of suppressed spin-flip scattering. In the meantime, SMR

shows a peak, which is consistent with the SMR theory. Our results further indicate that both the magnetic proximity effect and the spin current effect coexist in Pd/YIG bilayers systems.

3.2.4. Room Temperature Anomalous Hall Hysteresis in TIG/Pt

In bilayer structures containing a normal metal (NM) layer having strong spin-orbit coupling, such as Pt, Pd, etc., and a YIG layer, magnetoresistance emerges and evolves with temperature(*26, 45, 69, 84, 85, 89*). Associated with many interesting phenomena in YIG/NM bilayers, a hotly debated issue is whether the magnetic proximity effect or the pure spin current effect plays a more important role. Both mechanisms can produce magnetoresistance, namely the AMR, the SMR, and the anomalous Hall-like effects. A proximity-induced ferromagnetic layer in Pt can generate the AHE just as normal ferromagnetic conductors do. However, pure spin current, through the non-zero imaginary part of the spin-mixing conductance, can also give rise to an AHE-like response at the YIG/NM interface[12], but the relative importance of each mechanism has not been systematically addressed.

Experimentally, anomalous Hall-like response has been observed in YIG/NM bilayers such as YIG/Pt and YIG/Pd(*26, 69, 89*). In ferromagnetic conductors, the Hall response contains two parts: the ordinary Hall effect (OHE) which is linear in field, and the AHE which is proportional to the out-of-plane magnetization. Since YIG grown on GGG has easy-plane anisotropy, the AHE signal is non-hysteretic but saturates at high fields. This has been treated as the basis of separating out the AHE contribution. However, such separation can be problematic. First, the observed Hall saturation field is

an order larger than that of the YIG magnetization (~2000 Oe)(*26, 69, 89*). Second, even the sign and magnitude of the OHE background of YIG/NM is far from being understood(*90, 91*). If a ferrimagnetic insulator has PMA, the squared Hall hysteresis loop in bilayers would eliminate the aforementioned problem and therefore help understand the physical origin of the AHE.

In order to resolve the ambiguity of the physics original of AHE in previous magnetic insulator/Pt systems, we choose Pt, which has much larger SOC than Pd, deposited on our magnetic insulator with strong PMA in this study. We have shown the strain-induced robust PMA in TIG grown on a SGGG by in previous chapter. To maintain high-quality interfaces in bilayers, TIG is immediately transferred to a high-vacuum sputtering system for Pt or Cu deposition without being exposed to any resist or organic substance. Before the metal layer deposition, TIG films are lightly cleaned using Ar plasma for 3 minutes. Standard photolithography and Ar inductively coupled plasma etching are performed to pattern the metal layers into Hall-bars with the length of L=300 μm and the width of W =100 μm. Magneto-transport measurements are performed at room temperature either with an electromagnet or with a superconducting magnet in a Physical Property Measurement System. Figure 3-8(a) shows the Hall hysteresis loops for two representative samples: TIG (10 nm)/Pt (1.5 nm) and TIG (10 nm)/Pt (5 nm) along with the Hall signals in two reference samples: SGGG/Pt (2 nm) and TIG/SiO_2 (2 nm)/Pt (2 nm). Three messages are revealed in the figure: 1. the Hall hysteresis in Pt resembles the out-of-plane magnetic hysteresis of the underlying TIG film; 2. a thin SiO_2 layer quenches the Hall hysteresis completely; 3. the thinner the Pt layer is, the larger is the

Hall hysteresis magnitude. In the reference samples, only linear OHE is present. Similar OHE linear background is also present in TIG/Pt samples, but unlike in YIG-based bilayers, there is no ambiguity in separating AHE from the total Hall signal. In samples with different Pt thicknesses but sharing the *same* underlying TIG film, the AHE magnitude steadily decreases as the Pt layer thickness as shown in Figure 3-8(b), suggesting its interfacial nature.

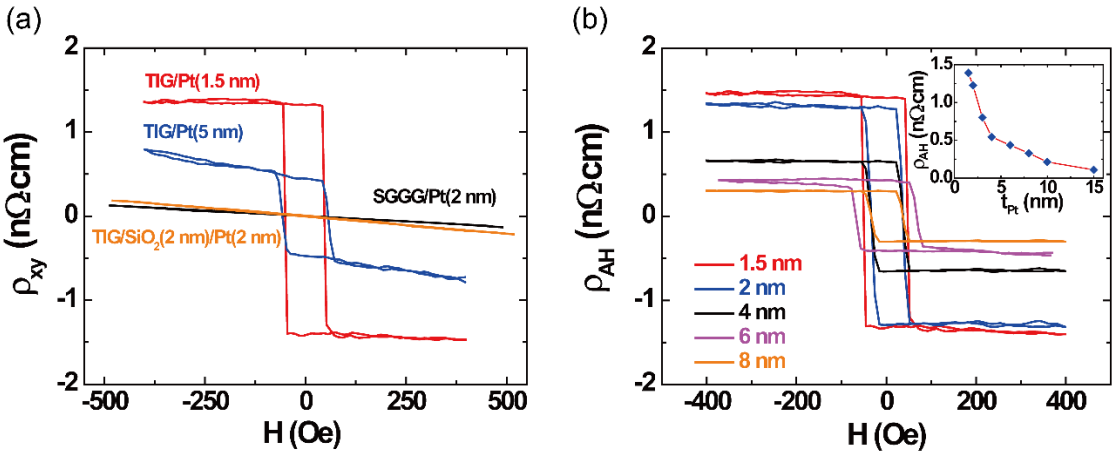

Figure 3-8. The Anomalous Hall effect in TIG/Pt layers. (a) Total Hall resistivity ρ_{xy} for TIG/Pt (1.5 nm), TIG/Pt (5 nm), SGGG/Pt (2 nm), and TIG/SiO_2(2 nm)/Pt (2 nm). (b) The anomalous Hall resistivity for different TIG (10 nm)/Pt samples with different Pt layer thicknesses: 1.5, 2, 4, 6, and 8 nm. Inset: Thickness dependence of the anomalous Hall resistivity.

Two possible mechanisms can give rise to the AHE hysteresis in paramagnetic Pt. First, if the Pt interface layer is magnetized by TIG via proximity coupling, then it behaves effectively as a thin ferromagnetic metal, and consequently the hysteresis can arise from the conventional AHE(*8*). As the Pt thickness increases, the AHE signal from the interface layer is diluted by the increasing paramagnetic portion. The other possible mechanism is the spin Hall-AHE (SH-AHE), a spin current effect(*71*), which originates

from spin precession around the exchange field due to the presence of the magnetic moment. Both SH-AHE and SMR share the same origin, and are theoretically connected to the imaginary and real parts of the same spin-mixing conductance. We have carried out room temperature magnetoresistance measurements with a rotating field 1 T in the same set of samples as used for the Figure 3-8(b) inset. The SMR data show a similar decreasing trend as shown in Figure 3-9 and 3-10. Therefore, both mechanisms seem to be plausible to explain the Pt thickness dependence of the Hall magnitude.

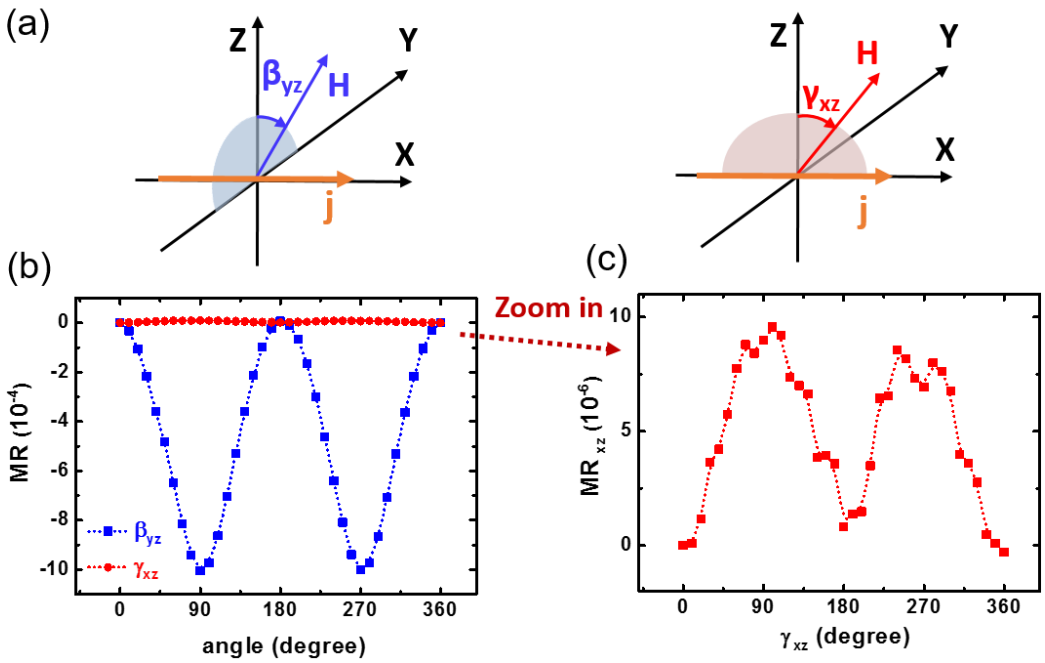

Figure 3-9. Angle rotation magnetoresistance in TIG/Pt bilayers. (a) Illustration of experimental measurement geometry. Magnetoresistance is measured with a magnetic field of a fixed strength but rotating either in the yz- or xz-plane; the corresponding angle is denoted by β_{yz} or γ_{xz}, respectively. (b) ADMR when a 1T field is rotating in yz- and xz- plane for a TIG/Pt (2 nm) sample. (c) Zoom-in ADMR when a 1T field is rotating in xz-plane

To study the effect of spin current in TIG/Pt bilayers, we perform magnetoresistance measurements with a rotating magnetic field which has been done in

many bilayer systems. Figure 3-9(a) shows the standard measurement geometry for such measurements. The applied magnetic field rotates in two different planes, i.e. yz- and xz-planes, described by two angles, β_{yz} and γ_{xz}, while the resistance is measured. In the SMR model, the former is SMR and the latter is AMR. In Figure 3-9(b), both room-temperature angle-dependent magnetoresistance curves are shown for a constant magnetic field strength of 1 T. In Figure 3-9(c), the magnetoresistance with the field rotating in the xz-plane, i.e. AMR, is magnified. It is clear that SMR is much greater than AMR at room temperature. This behavior is quite common in other bilayers. It is not surprising that spin current plays a role in the magneto-transport. However, the much smaller effect in AMR at room temperature does not necessarily mean the absence of the induced magnetism in Pt, which has been proved by the spin pumping(*43*) and XMCD(*92*) in YIG/Pt and the magneto-transport behavior in YIG/NM(*26, 69, 89*) and YIG/IrMn(*93*).

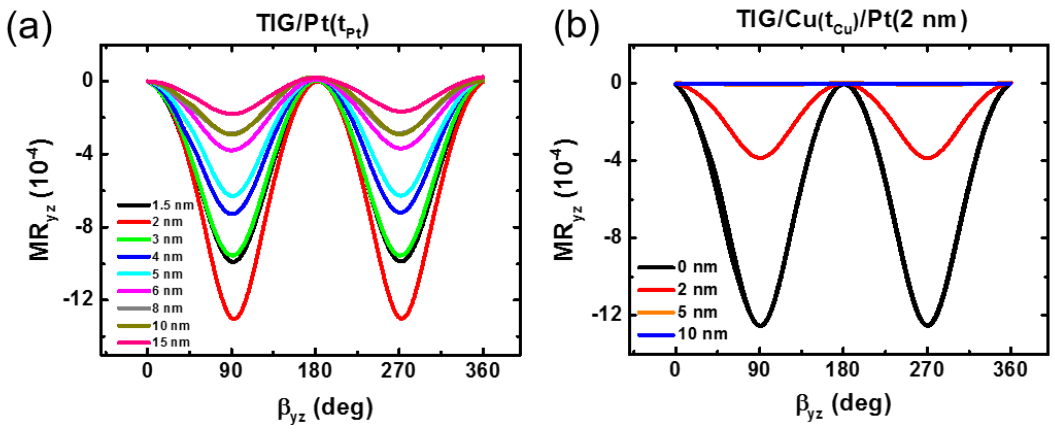

Figure 3-10. Spin Hall magnetoresistance for TIG/Pt and TIG/Cu/Pt. (a) SMR measured with a 1T field rotating in the yz plane in TIG/Pt samples with the Pt thickness varying from 1.5 to 15 nm. (b) SMR in TIG/Cu/Pt samples with different Cu layer thicknesses.

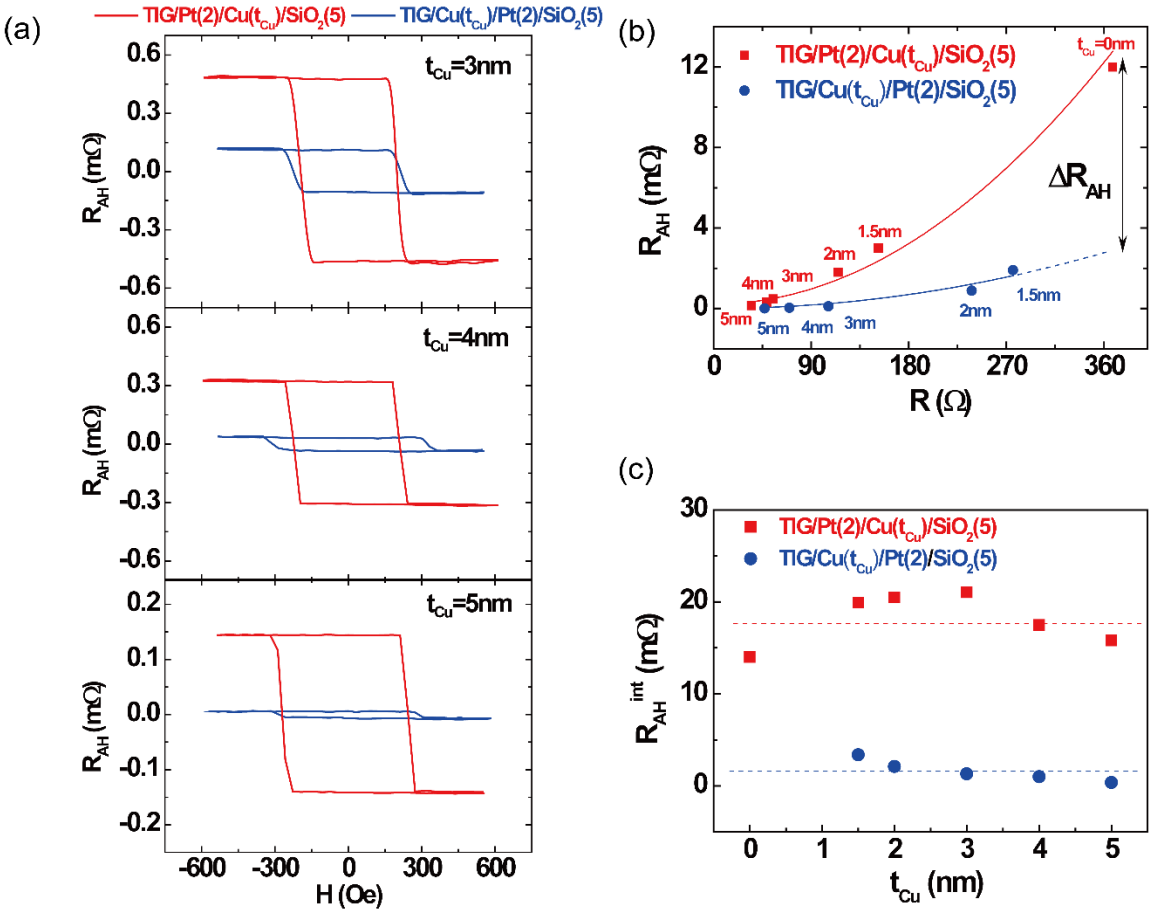

Figure 3-11. The Anomalous Hall effect in TIG/Cu/Pt and TIG/Pt/Cu layers. (a) The anomalous Hall resistance R_{AH} for three representative TIG/Pt (2 nm)/Cu (t_{Cu})/SiO_2 (5 nm) and TIG/Cu (t_{Cu})/Pt (2 nm)/SiO_2 (5 nm) samples with t_{Cu}=3, 4 and 5 nm on a same 10 nm thick TIG film. (b) The anomalous Hall resistance R_{AH} as a function of the longitudinal resistance R for the two sets with all Cu thicknesses, i.e. t_{Cu}=1.5, 2, 3, 4 and 5nm. Solid curves are the fitting based on the shunting model of AHE: $R_{AH} \sim R^2$. (c) Calculated unshunted anomalous Hall resistance R_{AH}^0 as a function of the Cu thickness for the two sample sets.

Since SMR measurements are always accompanied by a current, current shunting effect occurs with a thicker Pt layer (Figure 3-10 (a)) or with an additional Cu layer inserted (Figure 3-10(b)). In the latter case, although Cu has a long spin diffusion length which allows spin current to propagate over a longer distance, SMR effect produced in Pt is quickly diluted by Cu, a better conductor. Therefore, the SMR decay with increasing

Cu does not mean that spin current is attenuated in Cu. Similarly, as discussed in the main text, AHE decays as a Cu layer is inserted due to the same current shunting effect.

In order to further distinguish the two mechanisms of the Hall hysteresis in TIG/Pt, we insert a thin layer of Cu between TIG and Pt. Since Cu has a long spin diffusion length (~350 nm), a few nm thick Cu layer should not suppress the spin current; therefore, no obvious effect is expected on AHE except for current shunting, if the spin current is responsible for the Hall hysteresis. On the other hand, a thin Cu layer should significantly affect the proximity coupling and therefore the AHE magnitude if the induced magnetic interface layer is responsible. To exclude the shunting effect, we prepare two sets of samples: TIG/Pt/Cu/SiO_2 (1) and TIG/Cu/Pt/SiO_2 (2) on the same TIG film, with exactly the same constituent layer thicknesses but the opposite stacking order for the Pt and Cu layers. The SiO_2 capping layer is important to prevent oxidation of the top layer, especially in Set 1 when Cu is at the top. As shown in Figure 3-11(a), upon insertion of a Cu spacer layer immediately above TIG, the absolute magnitude of the Hall hysteresis is quickly suppressed. What is more important, by placing a Cu layer of the same thickness on TIG/Pt instead, the AHE hysteresis is decreased by a lesser amount. Furthermore, a 5 nm Cu layer greatly reduces the Hall hysteresis in Set 2, but the AHE signal clearly remains finite. From AFM imaging, the rms roughness associated with the 2 nm Cu grown on TIG is ~ 0.15 nm (see Figure 3-12); therefore, we rule out the possibility of pinholes in Cu films. The finite Hall hysteresis loop in Set 2 strongly suggests that spin current plays a more important role rather than the proximity coupling when the inserted Cu is thick, since the latter is expected to be short-ranged.

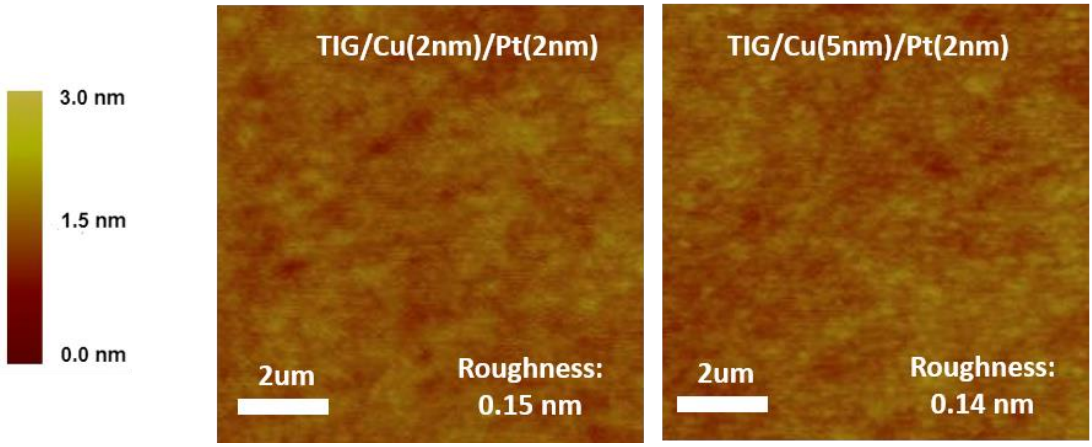

Figure 3-12.AFM imaging of the surface morphology of TIG/Cu/Pt indicating the smooth surface after Cu and Pt deposition. AFM surface profile of TIG (10 nm)/Cu (2 nm)/Pt (2 nm) (left) and TIG (10 nm)/Cu (5 nm)/Pt (2 nm) (right) with rms roughness about 0.15 nm and 0.14 nm over a 10μm × 10μm area, respectively, indicating the films are free of pinholes after Cu and Pt deposition.

We vary the Cu layer thickness from t_{Cu} 1.5 to 5 nm in both TIG/Pt (2 nm)/Cu/SiO_2 and TIG/Cu/Pt (2 nm)/SiO_2 sets. We note that even with the same Cu thickness the resistance of the two samples with the opposite Cu and Pt stacking orders is different. The resistance difference is more pronounced in thin Cu samples. It may be caused by different Cu textures when it is grown on different materials, i.e. TIG or Pt. To better correlate the shunting effect as the Cu layer thickness is varied, we measure the total resistance of the samples. In Figure 3-11(b), we plot the AHE magnitude as a function of the total measured resistance instead of the Cu thickness. As the Cu thickness increases, the resistance of the both sets decrease and at the same time the AHE magnitude decreases due to the shunting effect. However, the TIG/Pt (2 nm)/Cu/SiO_2 AHE curve stays consistently above that of TIG/Cu/Pt (2 nm)/SiO_2. The gap between these two AHE curves reveals the importance of the magnetic proximity coupling. As the

Cu thickness approaches zero in Set 2, i.e. extrapolating the curve for Set 2 to the same resistance value as that of TIG/Pt (2 nm)/SiO_2, the difference between the two curves, ΔR_{AH}^1, should represent the contribution from the proximity effect, as shown in Figure 3-11(b). After separating out the proximity-induced AHE contribution, the remaining AHE signal, ΔR_{AH}^2, is clearly from the spin current effect, i.e. SH-AHE. Below we adopt a simple model to explain the overall Cu layer thickness dependence in both sets. We assume the AHE voltage from the Pt layer to be the voltage source and the presence of the Cu layer merely shunts the current flowing in Pt; therefore, the measured AHE voltage is reduced. The AHE source may contain more than one mechanism. With this simple circuit model, the measured AHE resistance scales with the total sample resistance squared, i.e. $R_{AH} = \left(\frac{R}{R_{Pt}}\right)^2 R_{AH}^0$, here R_{AH}^0 being the AHE resistance from the Pt layer only regardless of its physical origin, R being the total resistance of the samples, and R_{Pt} being the resistance of the Pt layer. Figure 3-11(c) is the R_{AH}^0 vs. t_{Cu} plot. As the Cu thickness varies, R_{AH}^0 is nearly constant for both sample sets. It means that the decreased AHE magnitude in thicker Cu samples can indeed be described by the current shunting effect. When the Pt layer is directly on top of TIG, the constant value is clearly larger than when the Cu layer separates the Pt layer from TIG. The former contains both proximity induced AHE and SH-AHE; therefore, we attribute the difference between the two values to the proximity induced mechanism which apparently dominates the other.

In summary, squared AHE hysteresis loops are observed in TIG/Pt bilayers at room temperature and analyzed in the context of both proximity coupling and spin

current effects. Our experimental results indicate that both effects need to be considered to fully understand the transport phenomena in ferrimagnetic insulator/NM bilayers.

3.2.5. Temperature Dependence of Hall Effects in TIG/Pt

The sharp squared AHE hysteresis loops observed in TIG/Pt bilayers unambiguously reflects the magnetization of underneath magnetic insulator layer TIG, unlike the case of YIG/Pt, where AHE-like signal is being considered saturated at high fields. One unique advantage of such share square shape of AHE hysteresis is its robustness, without any contamination from the two-band nonlinear curvature where an additional nonlinear can exist originating from the co-existence of electron and hole carriers(*94*). The magnitude of AHE resistance can be obtained in a more straightforward way, thanks to the robust perpendicular magnetic anisotropy of TIG film. Two experiments, beneficial from the share squared Hall loops in TIG/HM, will be introduced in the following discussions: the sign reversal of Hall effect in TIG/Pt which demonstrates the modification of the band structure of thin Pt layer via exchange coupling with the magnetic TIG layer and the current-induced switching of magnetization in TIG layer.

As a consequence of the in-plane magnetic anisotropy nature of YIG films, the in-plane magnetoresistance easily captures the magnetization dynamics and thus has been reported in various YIG/HM systems in a wide temperature range. However, there is lack of systematic study of AHE in the magnetic insulator/heavy metal bilayer at different temperatures. It is because that the accurate reading of the AHE in YIG/HM resistance remains challenging. When the field is lowering to the saturation magnetic field H_{sat}, the

magnetization quickly lies in the film plane and moves to the easiest axis. The evolution of the magnetization at small field gives rise to the mixture of the considerable large planar Hall resistance in the AHE(*91*). Such aforementioned problem can be solved in TIG/Pt in which a sharp squared Hall hysteresis loop is developed. The Hall effects in TIG/Pt unequivocally identifies the magnetization and provides empirical evidence to directly probe the nature of the interface magneto-transport in the magnetic insulator/HM bilayer systems.

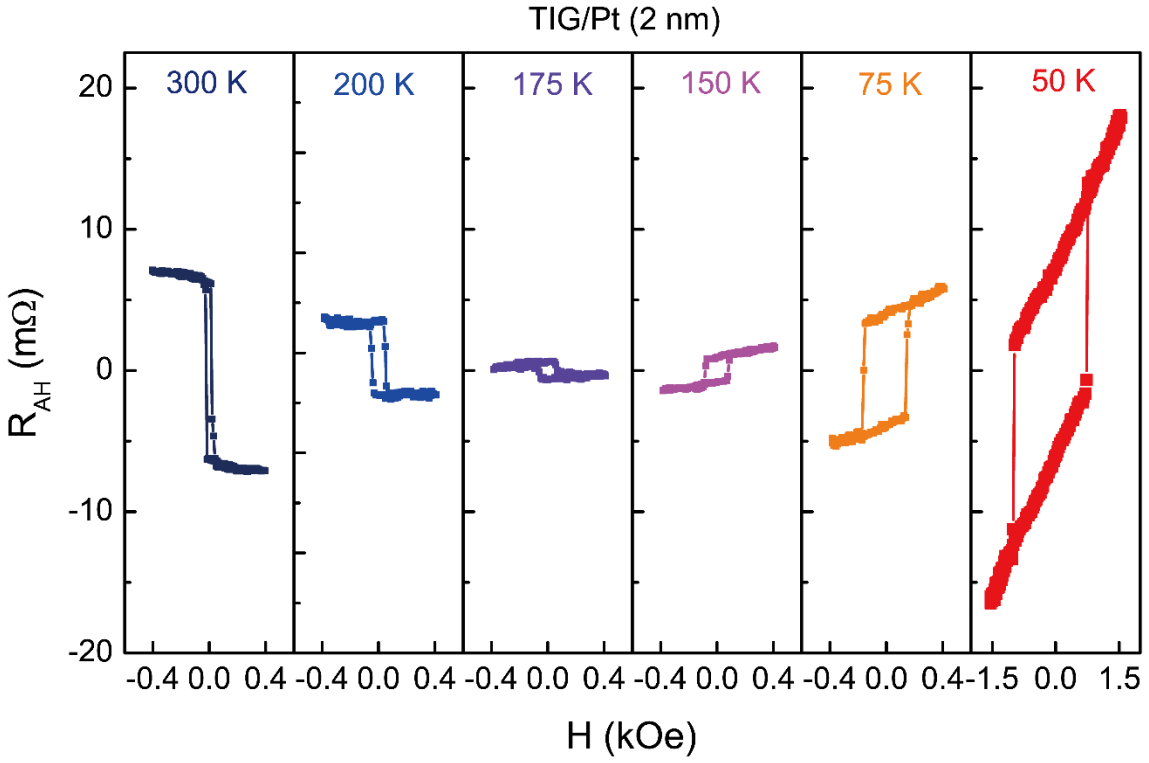

Figure 3-13. Temperature dependence of a chosen thickness of Pt on TIG sample. The anomalous Hall resistance reverse sign between 175 K and 150 K and the ordinary Hall coefficient reverses the sign between 200 K and 175 K.

Figure 3-13 shows the temperature dependence of Hall effects in a TIG/Pt with a chosen Pt thickness of 2 nm. The TIG thickness is kept as a constant 10 nm in this experiment. Surprisingly, both the ordinary Hall effect (OHE) and AHE reverse the sign when temperature is lowering. The sign of OHE coefficient is negative at high temperatures above 175 K, indicating an electron dominating carrier type in Pt as expected. The OHE coefficient reverses its sign when temperature is decreasing to 175 K and then kept as positive throughout the low temperatures below 175 K. The positive OHE coefficient implies the change of carrier types from the electron to hole, originating from a modification of the band structure in Pt layer. Such change of OHE coefficient only occurs for thin Pt which will be discussed later. The square looped AHE superimposed on the linear OHE background also reverses the polarity but in a different manner. If defining the sign of AHE at 300 K as negative, AHE remains negative until the temperature reaches 150 K and maintains the positive polarity, associated with the increasing of the magnitude, when temperature is further decreasing. It has been addressed that both spin current and magnetic proximity effect contribute to the observed AHE while the latter dominates(*58*). The sign reversal in AHE is then either from a modification of Pt band structure via exchange coupling with TIG or a change in the spin current reflection/transmission metrics. According to the SMR model, the magnetoresistance is modulated by the absorption of spin current generated by SHE in Pt depending the relative collinearity between the polarization of spin current and the magnetization of the underlying ferromagnet. Hypothetically speaking, a sign change in the spin current reflection/transmission metrics, i.e. spin mixing conductance, is possible

to induce a sign reversal of the AHE in principle. However, in the scope of SMR(*71*), the carrier type change implied by the sign change of OHE coefficient is not expected based on the pure spin-diffusion approximating in terms of spin mixing conductance in Pt layer. Here we propose that introducing the exchange interaction in the thin heavy metal Pt layer with the presence of high SOC modifies the band structure of thin Pt layer and thus gives rise to the sign reversal of both AHE and OHE, the former strongly relying on the Berry phase and the latter depends on the overall density of states integration. In analogy to the quantum anomalous Hall effect in TI, introducing the exchange interaction breaks the time reversal symmetry in TI and consequently opens a nontrivial band gap at the Dirac surface states with sufficient SOC(*10, 11*). Unlike the Dirac band structure of the TI surface states, the band structure in metal such as Pt is more complicated. However, the above interpretation still applies qualitatively in the sense that the exchange coupling lifts the degeneracy of spin-up and -down states, yielding the net magnetic moment of in the Pt layer characterized by a penetration depth of exchange interaction. Furthermore, the s-d hybridization modifies the band structure of thin Pt layer and possibly leads to a positive OHE coefficient resulting from the negative group velocities at the Fermi level, as previously demonstrated in transition-metal alloys(*95*, *96*).

To further confirm the physical origin of the temperature dependence of AHE and OHE in TIG/Pt, we systematically change the thickness of Pt layers and prepared few control samples including TIG/Cu (2 nm)/Pt (3 nm) to terminate the magnetic proximity effect, NGG/Pt (2 nm) with SOC present only and TIG/Cu (2 nm) with source of magnetism present only. Figure 3-14 illustrate explicitly the temperature dependence of

OHE coefficients and AHE resistivities for all the samples. First, the OHE in the set of samples TIG/Pt (t_{Pt}) with t_{Pt} varying from 1.5 nm to 6 nm have two distinct behaviors, as shown in Figure 3-14(a). The OHE changes sign at different transition temperatures only for t_{Pt} smaller than 6 nm and remains negative sign when t_{Pt} reaches 6 nm. It implies that when the thickness of Pt layer is over a critical thickness (4 nm in this experiment), the overall density of states in the whole Pt have a net positive group velocities and thus leads to a negative Hall coefficient as expected for normal metals. Since the s-d exchange coupling is only effective within a short penetration depth (Ru *et al*. Calculation), we denote that the top layers of Pt films without being affected by the exchange interaction as normal Pt layer. More electron carriers from the normal Pt layer in thicker Pt films participate the transport diluting the contribution from the magnetized Pt layer and leads to a negative OHE coefficient. If we turn off the s-d exchange coupling by replacing TIG with NGG while leaving the SOC on, the OHE coefficients remains negative throughout the whole temperature range, exhibiting sharp contrast with TIG/Pt devices with the same Pt thickness 2 nm. Same scenario is applied to the case when we only switch off the SOC term by replacing Pt with Cu, the OHE coefficients is still negative in the entire temperature range. It confirms that the importance of both exchange coupling and SOC in the modification of thin Pt band structure. Note that inserting 2 nm Cu between TIG and Pt shows the similar behavior as NGG/Pt (2 nm), where the sharp increase of positive OHE coefficient from Pt is gone due to the absence of magnetic proximity effect.

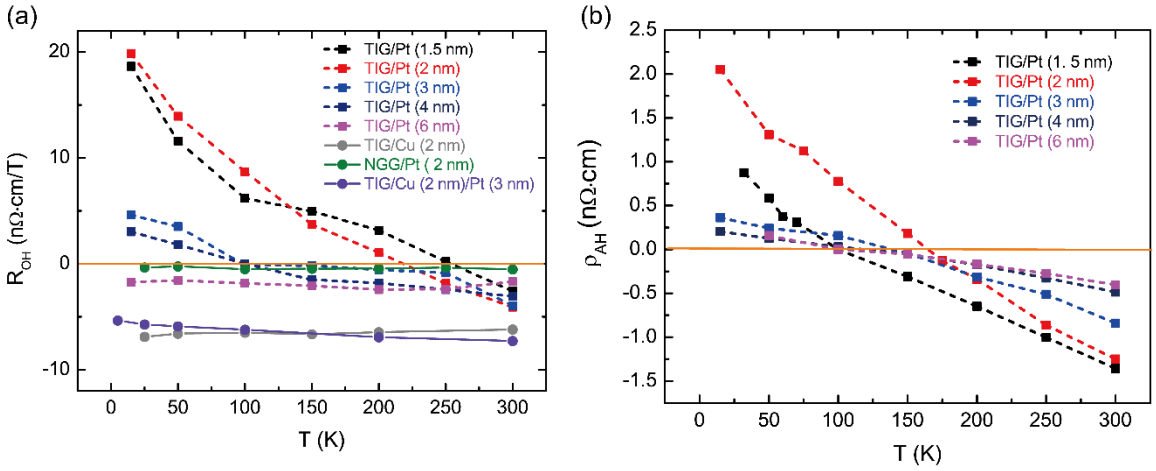

Figure 3-14. The temperature dependence of anomalous Hall resistivity and the ordinary Hall coefficient for different thickness of TIG/Pt and control samples. (a) The temperature dependence of OHE coefficient for TIG/Pt (t_{Pt}) and control samples NGG/Pt (2 nm), TIG/Cu (2 nm), TIG/Cu (2 nm)/Pt (3 nm). (b) The temperature dependence of AHE resistivity of TIG/Pt (t_{Pt}).

As indicated in Figure 3-14(b), the AHE reverses sign for all thickness of Pt layer up to 6 nm, showing slight difference with the sign change in OHE coefficient. It should be emphasized that the sign change transition temperatures $T_{sign\ change}$ for AHE are different from that of OHE coefficient. The intrinsic AHE is related to the electric field to their Berry curvatures (*8*). While the OHE is mainly determined by the total density of states at the Fermi level, the AHE strongly depends on the anomalous velocity generated by the integral over Berry curvature. Both of them rely on the band structure but behave differently when the Fermi level shifts as a consequence of change in temperature. As further summarized in Figure 3-15, the $T_{sign\ change}$ shows a monotonic decreasing trend for OHE which can be interpreted as a dilution of abnormal carriers, which possess a negative group velocity, by the participation of more normal electron carriers from top layers of Pt films, giving rise to absence of sign change in OHE coefficient for thicker Pt films. $T_{sign\ change}$ of AHE shows a non-monotonic behavior in function of Pt thickness.

Since the AHE in Pt at least has two contributions: magnetized Pt induced conventional AHE and Spin-Hall AHE, the temperature dependence of AHE evolves in a more complicated way.

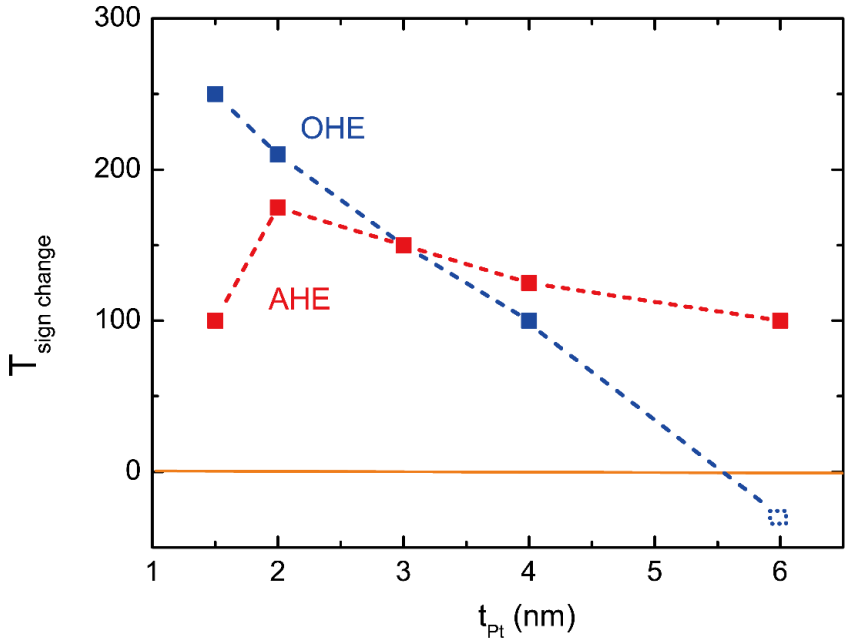

Figure 3-15. The critical sign change temperature for ordinary Hall effect and anomalous Hall effect as a function of thickness of Pt layer on TIG. The blue short dashed box for 6 nm Pt indicates the absence of sign change in OHE.

Despite the complexity in the interface transport in the TIG/Pt bilayers, the observation of sign change in the AHE and OHE by studying the temperature dependence confirms the critical role of magnetic proximity effect in modifying the band structure of the thin Pt layer with a short-range penetration depth. The proximity induced magnetism in non-magnetic material introduces more functionalities and spurs invigorated discoveries in the field of spintronics, such as realizing high temperature ferromagnetic phase in topological insulator, photo-spin-voltaic effect, etc.

3.2.6. Saturation Magnetization Dependent Spin Torque Efficiency in TIG/W

The interplay between heavy metals and magnetic insulators has attracted tremendous attention from both fundamental research and practical applications (*3, 97, 98*). Although efficient manipulation and even switching of magnetization and its dynamics have been achieved in conducting systems through SHE or Rashba-Edelstein effect (*99-104*), the control of the magnetic moment in magnetic insulators remains challenging. One of the challenges is the readout of the magnetic information through transport properties since magnetic insulators are electrically insulating. The recently discovered anomalous Hall resistance (AHR) and SMR, due to spin current effect in magnetic insulator/HM heterostructures, provide unique ways for detecting the magnetization dynamics of magnetic insulators (*45, 105-108*). With the help of the observed SMR, current-driven ferromagnetic resonance in a magnetic insulator was achieved recently (*109, 110*). More recently, current-induced magnetization switching was realized in both $BaFe_{12}O_{19}$/Pt (BaM) and $Tm_3Fe_5O_{12}$ (TIG)/Pt bilayers by probing the AHR (*111, 112*).

However, the observed damping-like spin torque efficiency (ξ_{DL}) in the TIG/Pt that is responsible for switching is still much lower than those in the ferromagnetic metals (FMs)/Pt (*112-114*). Increasing the value of ξ_{DL} is crucial for the future development of spintronic devices based on TIG. In general, $\xi_{\mathrm{DL}} = T_{\mathrm{r}}\theta_{\mathrm{ST}}$. Here, θ_{ST} is the intrinsic spin torque ratio due to either SHE or Rashba-Edelstein effect, which is an intrinsic value and should be a constant for a given material at room temperature. A complex phenomenological spin transparency is defined as $T = T_{\mathrm{r}} + iT_{\mathrm{i}}$ for describing how much spin momentum can be transferred into the ferromagnetic layer, where T_{i} determines the

field-like spin torque efficiency through $\xi_{FL} = T_i\theta_{ST}$. To increase the value of ξ_{DL}, one can either increase θ_{ST} or T_r. So far, β-W is reported to give the largest spin Hall angle, or θ_{ST}, among elemental heavy metals (*115*), which is preferred for maximizing ξ_{DL}. Regarding the spin transparency, various mechanisms, such as spin backflow (*45, 106*) and spin memory loss (*116*), have been explored as the reason causing T_r to be less than 1. Here, we propose that ξ_{DL} also depends quadratically on the saturation magnetization (M_S) when the M_S of thin films is below the corresponding bulk value (*117, 118*). The Landau–Lifshitz–Gilbert equation in the presence of current can be written as

$$M_s t\frac{d\hat{m}}{dt} = -\gamma M_s t\hat{m}\times\left(\vec{H}_{eff} + \vec{H}_{ext}\right) + \alpha M_s t\hat{m}\times\frac{d\hat{m}}{dt}$$
$$+\gamma J_c\xi_{DL}(\hat{m}\times\hat{\sigma}\times\hat{m}) + \gamma J_c\xi_{FL}(\hat{m}\times\hat{\sigma}), \quad (1)$$

where $\hat{m}$ is the unit vector of magnetization, $\hat{\sigma}$ is the unit vector of current-induced spin polarization, γ is the gyromagnetic ratio, α is the Gilbert damping, t is the thickness of ferromagnetic layer, J_c is the charge current density, $\vec{H}_{eff}$ is the effective anisotropy field, and $\vec{H}_{ext}$ is the external magnetic field. The last two terms on the right-hand side of Eq. 1 arise due to absorption of spin current by the ferromagnet, which are referred to as the current-induced spin-orbit torques. In particular, these torques have a dissipative (damping-like) and a conservative (field-like) component, whose strengths are respectively parameterized by dimensionless efficiency parameters ξ_{DL} and ξ_{FL}. The origin of these spin-orbit torques can be understood in a simple microscopic picture as follows. A charge current at the heavy metal and ferromagnet interface translates into a spin density, $\rho\hat{\sigma}$, due to the finite spin-orbit interaction (for example, by SHE or Rashba-

Edelstein effect). Here ρ is the magnitude of the spin density, which is proportional to the strength of the spin-orbit interaction. This spin density interacts with the ferromagnet via exchange interaction, of the form $U_{\mathrm{ex}} \sim \rho M_{\mathrm{s}} \hat{m} \cdot \hat{\sigma}$, enabling the absorption of the spin current by the ferromagnet. In a perturbative treatment, the spin current absorbed by the ferromagnet can be obtained up to second order in the exchange interaction to yield the damping-like and field-like component of spin-orbit torques with $\xi_{\mathrm{DL}} \sim M_{\mathrm{s}}^2$ and $\xi_{\mathrm{FL}} \sim M_{\mathrm{s}}$, which we refer here as the M_{s}-effect (*117*). So far, this M_{S}-effect has not been considered in experiments despite the fact that many experiments are performed in ultrathin ferromagnetic metals, where the M_{S} could be decreased due to a reduced Curie temperature (*119*).

In this section, we experimentally demonstrate that T and thus $\xi_{\mathrm{DL}}(\xi_{\mathrm{FL}})$ are dependent on M_{S}. We study the current-induced spin-orbit torques in TIG/W structures of different TIG layer thickness (t_{TIG}). The sufficiently tensile strain induced by large lattice mismatch between TIG and underlying substrate enables robust PMA for all three TIG films with thicknesses up to 9.6 nm. We observe a significant reduction of M_{S} with decreasing film thickness from a value close to the bulk M_{S} at 9.6 nm (*120*). This thickness-dependent M_{S} in TIG thin films provides a unique platform to test the M_{S}-effect. We directly quantify both ξ_{DL} and ξ_{FL} by using second-harmonic Hall measurement (*121, 122*). We observe a dramatic increase of both ξ_{DL} and ξ_{FL} as the t_{TIG} increases, originating from the enhancement of M_{S}. Finally, we demonstrate the current-induced switching in TIG/W up to t_{TIG} = 9.6 nm with a switching current density as low as 6×10^{10} A/m^2. The current switching efficiency, defined as total magnetic angular

momentum over switching current density, enhances as t_{TIG} increases, which is consistent with the increase of ξ_{DL}. The switching current density obtained in this work is much lower than the TIG/Pt case (*112*).

Perpendicularly magnetized TIG films with three different thicknesses (3.2 nm, 6.4 nm, and 9.6 nm) were grown on $Nd_3Ga_5O_{12}$ by pulsed laser deposition (*108*). The large lattice mismatch between the TIG and the $Nd_3Ga_5O_{12}$ provides the tensile strain to generate PMA in the TIG. Figure 3-16(a) shows magnetization hysteresis loops of three TIG thin films as a function of an out-of-plane magnetic field measured by a vibrating sample magnetometer, confirming the nature of PMA in all the three samples. The TIG thin films show an atomically smooth surface with mean roughness as low as 0.1 nm in a 2×2 μm scan area as indicated by the inset of Figure 3-16(a), providing a sharp interface for efficient spin momentum transfer. We deposited a 5 nm-thick W layer on top of TIG followed by subsequent deposition of MgO(2 nm)/TaO_x(3 nm) layers to protect W from oxidization. The films were patterned into Hall bar devices by using standard photolithography and dry etching for the resistance, spin torque and switching measurements, as shown in Figure 3-16(b). The channel width is 20 μm, and the distance between two neighboring Hall contacts is 26 μm. We measured the first harmonic Hall resistance by using $I_{ac,r.m.s}$ = 0.1 mA ($J_{ac,r.m.s}$ = 10^9 A/m^2). We measured the second harmonic Hall resistance by applying a $I_{ac,r.m.s}$ = 1 mA with a frequency $\frac{\omega}{2\pi} = 195.85$ Hz. The current source used was Keithley 6221, and the voltage was read out by using SR830 lock-in amplifiers. The magnetic field and angle controls were done in a physical properties measurement system. The current-induced switching experiments were

performed by applying a pulse current with 5 ms pulse width (Keithley 2612) and reading Hall voltage subsequently (Keithley 2182).

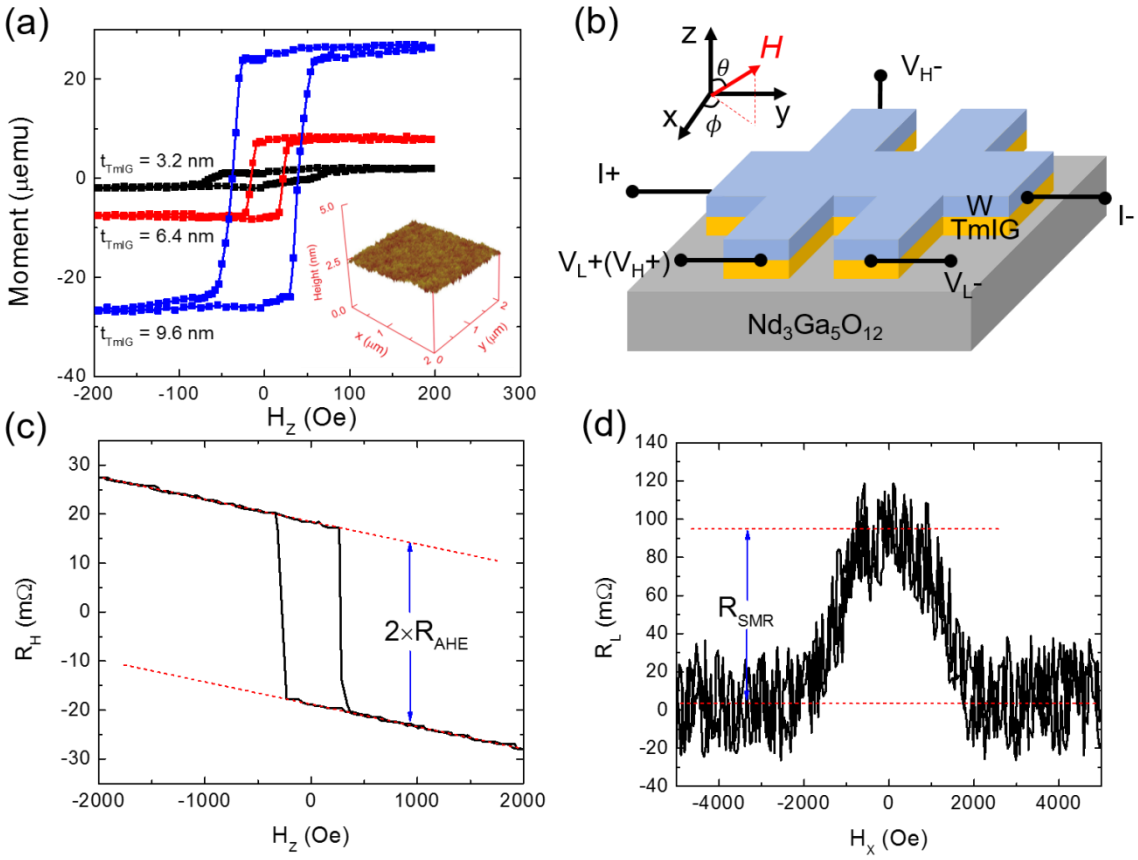

Figure 3-16. Basic properties of TIG thin films, W/TIG devices and measurement schematic. (a) Magnetic moment as a function of an out-of-plane magnetic fields for TIG thin films with different thicknesses. The inset is the AFM image of TIG film. (b) Experimental setup for measuring resistance, spin torque and current-induced switching. The Hall and longitudinal resistance are given by $R_{\mathrm{H}} = (V_{\mathrm{H}+} - V_{\mathrm{H}-})/I$ and $R_{\mathrm{L}} = (V_{\mathrm{L}+} - V_{\mathrm{L}-})/I$. (c) Hall resistance as a function of an out-of-plane magnetic field in the W (5 nm)/TIG (9.6 nm). (d) Longitudinal resistance as a function of an external magnetic field along the $\pm x$ direction in the W (5 nm)/TIG (9.6 nm).

We observe clear AHE and SMR in all three TIG/W devices, where results of W (5 nm)/TIG (9.6 nm) are shown in Figure 3-16(c) and (d). The sharp anomalous Hall hysteresis at low fields allows us to determine the AHR in the TIG/W accurately (see

Figure 3-16(c)). Since W is far away from the Stoner instability and there is no anisotropic magnetoresistance (*yz*-plane resistance change) in the TIG/W (not shown here), we attribute the observed AHE at room temperature to the spin current effect. We also observe significant SMR by rotating the magnetization in the *xz*-plane through scanning field transverse to the current direction (along the ±*x* direction) as shown in Figure 3-16(d). The observation of sizeable AHR and SMR indicates that there is a significant spin current being transmitted across the TIG/W interface (*106*).

We observe a strong t_{TIG} dependence of AHR and SMR as shown in Figure 3-17(a). Both AHR and SMR increase as t_{TIG} increases. This is different from the previous experimental observation, where AHR and SMR do not show a clear relation with the thickness of thick YIG (> 10 nm), in which the M_{S} already saturates, and is close to the bulk value (*105*). According to the SMR theory, the magnitudes of SMR and AHR are governed by an interfacial phenomenological parameter, spin mixing conductance ($G_{\uparrow\downarrow} = G_{\mathrm{r}} + iG_{\mathrm{i}}$), which does not explicitly depend on the thickness of the magnetic insulator when the magnetization is considered being saturated (*106*). However, in our ultrathin TIG films, a significant decrease in M_{S} by reducing the thickness is experimentally measured by superconducting quantum interference device and confirmed by vibration sample magnetometer (see Figure 3-17(b)). The lower M_{S} for thinner TIG films is possibly due to the finite size effect and spin-spin interaction that cause a decrease of the Curie temperature (*119*).

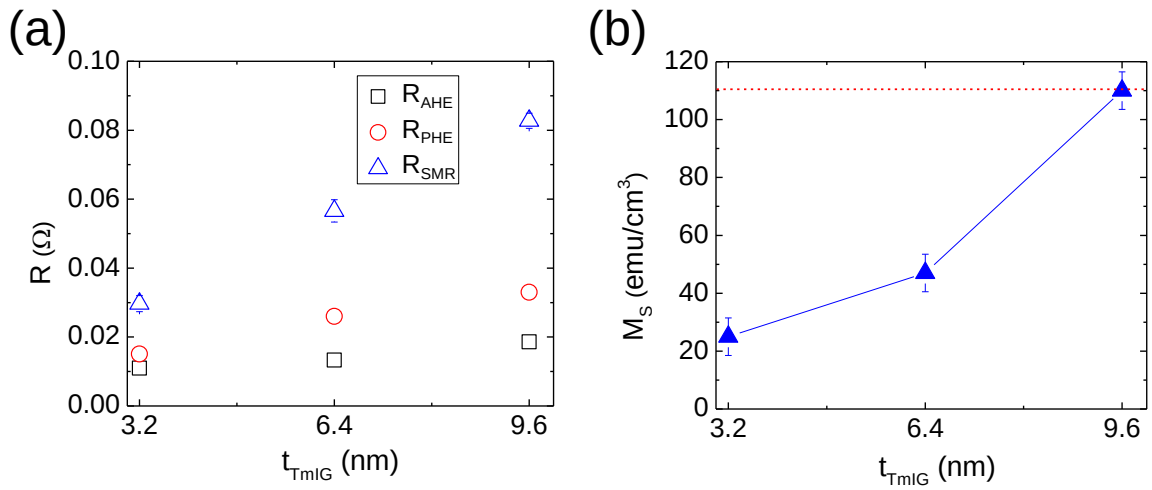

Figure 3-17. TIG thickness dependence of AHR and SMR. (a) AHR, planar Hall resistance and SMR as a function of TIG thickness. (b) Thickness dependence of saturation magnetization. The red dashed line indicates the bulk saturation magnetization value.

To examine the relation between the M_S and the spin torque efficiency, we quantify both ξ_{DL} and ξ_{FL} by using the second-harmonic analysis of both anomalous and planar Hall resistances (R_{AHE} and R_{PHE}) (*121, 122*). We determine the R_{PHE} by fitting φ-dependent Hall resistance when the magnetization is in the film plane ($\theta = 90°$). Since there is a huge thermoelectric effect for the TIG/W bilayer and the R_{PHE} is comparable with the R_{AHE} (see Figure 3-17(b), we do not employ the small field-scan method (*112, 123*). Instead, we use the large field-rotation method (*122*). The second-harmonic Hall resistance ($R_H^{2\omega}$) in a single domain subjected to a large in-plane magnetic field can be written as (*122, 124*)

$$R_H^{2\omega} = R_{FL}^{2\omega}\cos 2\varphi \sin\varphi + R_{DL}^{2\omega}\sin\varphi = R_{PHE}\frac{H_{FL}}{|H_{ext}|}\cos 2\varphi \sin\varphi +$$

$$\frac{R_{AHE}}{2}\frac{H_{DL}}{|H_{ext}|-H_K}\sin\varphi, \quad (2)$$

where $R_{\mathrm{FL}}^{2\omega}$ and $R_{\mathrm{DL}}^{2\omega}$ are the peak values of $\cos 2\varphi \sin \varphi$ and $\sin \varphi$ components in $R_{\mathrm{H}}^{2\omega}$, respectively. $H_{\mathrm{FL}}$and H_{DL} are the current-induced field-like and damping-like effective fields, respectively. We determine the anisotropy field H_{K} by fitting the in-plane hysteresis loop. Ideally, $R_{\mathrm{FL}}^{2\omega}$ and $R_{\mathrm{DL}}^{2\omega}$ are the field-like torque and damping-like torque contribution, respectively. To ensure having a single domain, we always apply an external field larger than H_{K} in the film plane. However, a field much larger than H_{K} will make the $R_{\mathrm{H}}^{2\omega}$ induced by spin-orbit torques undetectable. Therefore, we choose the field in a range between 2000 Oe and 5000 Oe. At 2500 Oe, we observe both damping-like and field-like torque contributions, as reflected by the $\cos 2\varphi \sin \varphi$ and $\sin \varphi$ angle dependencies (see Figure 3-18(a)). We plot the extracted $R_{\mathrm{DL}}^{2\omega}$ and $R_{\mathrm{FL}}^{2\omega}$ as a function of $1/(H_{\mathrm{ext}}\text{-}H_{\mathrm{K}})$ and $1/H_{\mathrm{ext}}$, as shown in Figure 3-18(b), respectively. Slopes of linear fits in Figure 3-18(b) give the information about the damping-like field, and the intercepts are the spin Seebeck resistances (or voltages) (*122*, *125*). We find that the spin Seebeck resistance increases as t_{TIG} increases. Since the spin Seebeck voltage is proportional to the temperature difference at the two sides of the magnetic insulator, the increase in spin Seebeck resistance means that the temperature difference becomes larger as the t_{TIG} increases. This is reasonable since the Joule heating due to the applied current is the same for these three samples and bottom of the TIG becomes farther as the t_{TIG} increases. Slopes of linear fits of the extracted $R_{\mathrm{FL}}^{2\omega}$ as a function of $1/H_{\mathrm{ext}}$ are used to determine the field-like effective fields, where a large

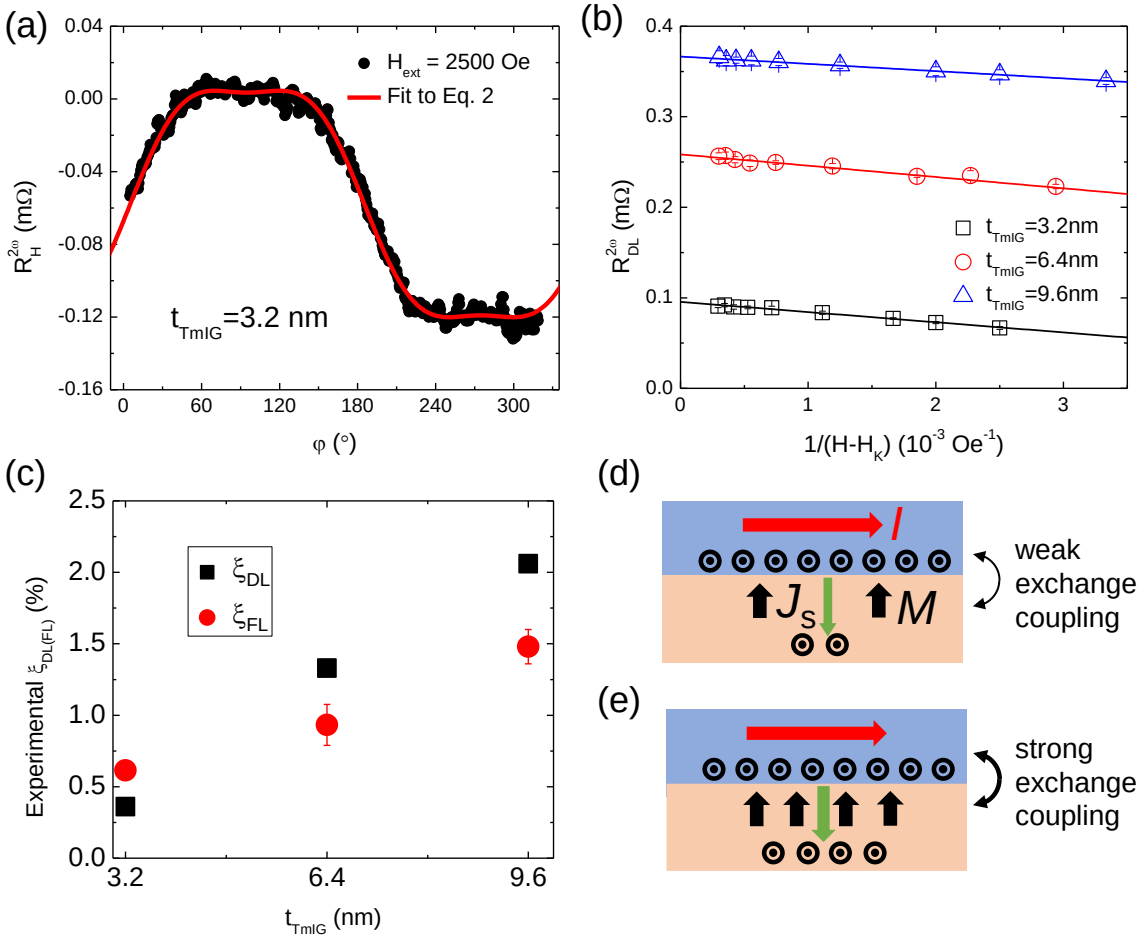

Figure 3-18. Spin torque efficiency in TIG/W with different TIG thicknesses. (a) Second-harmonic Hall resistance as a function of in-plane azimuthal angle for the external magnetic field 2500 Oe. In (a), a clear $\cos 2\varphi \sin \varphi$ angle dependence is revealed as it deviates from a $\sin \varphi$ angle dependence significantly. (b) Extracted damping-like torque contribution as a function of the inverse of external magnetic field subtracting the anisotropy field. The large intercepts are the spin Seebeck resistance. (c) Experimentally determined damping-like and field-like spin torque efficiency as a function of TIG thickness. (d-e) Schematic illustration of relation between spin transparency and M_S through exchange coupling. In (d), M_S is small, and less spin current gets through the interface. In (e), M_S is larger, and more spin current gets through the interface.

uncertainty occurs in thick TIG films due to large thermal effect. Nevertheless, the considerable values of field-like torques compared with the damping-like torques in these TIG/W bilayers are consistent with the considerable AHR compared with SMR, according to the SMR theory (*106*). Both the damping-like and field-like torque

efficiencies for three TIG/W devices with thicknesses 3.2, 6.4 and 9.6 nm are calculated by using $\xi_{\mathrm{DL(FL)}} = \frac{2eM_S t_{\mathrm{TIG}} H_{\mathrm{DL(FL)}}}{\hbar J_{\mathrm{ac\_peak}}}$ (*100*), where e is the electron charge, $\hbar$ is the reduced Planck constant and $J_{\mathrm{ac\_peak}}$ is the applied peak current density (see Figure 3-18(c)).

We observe a dramatic increase of both ξ_{DL} and ξ_{FL} as t_{TIG} increases, in sharp contrast to the heavy metal/FM case, where ξ_{DL} is almost independent of the thickness of FM, when the thickness of FM is larger than 1 nm (*123*). In our HM/MI case, the amount of spin current across the interface changes with t_{TIG}, as reflected by the thickness dependence of ξ_{DL} (see Figure 3-18(c)). Therefore, the spin transparency (T_{r}) increases as t_{TIG} increases, assuming the intrinsic spin torque ratio remains constant. We interpret this as a result of increasing M_{S} since the interfacial T_{r} is positively correlated with the M_{S} as illustrated in Figure 3-18(d) and Figure 3-18(e). When M_{S} is small and the exchange coupling is weak, only a small amount of spin current can pass through the interface (see Figure 3-18(d)). When M_{S} is large and the exchange coupling becomes stronger, more spin current can get across the interface (see Figure 3-18(e)). The theoretical foundation has been discussed in the introduction part by treating the exchange coupling perturbatively when M_{S} is small (*117*). Alternatively, as explained in ref. (*118*), the spin pumping efficiency depends on the M_{S} quadratically at a given microwave excitation. Similarly, the Onsager reciprocal process, namely spin injection efficiency, should also depend on the M_{S} quadratically. These simple pictures also agree with the first-principle calculation, where G_{r} increases as the interface magnetic moment density increases (*126*). Our observation, where ξ_{DL} increases as M_{S} increases, is in qualitative agreement with the theoretical prediction.

After quantifying the spin torque efficiency, we perform the current-induced magnetization switching experiments for TIG/Ws with different TIG thicknesses. The switching can be achieved in all three thicknesses as shown in Figs. 4a-4c. The switching direction is consistent with the sign of spin Hall angle of W and is opposite to the TIG/Pt case (*112*). We notice that the switching current is as low as 4×10^{10} A/m^2 in the TIG (3.2 nm)/W (5 nm) with the assistance of an in-plane magnetic field of only 135 Oe. This switching current is five times smaller than the TIG (8 nm)/Pt (5 nm) case (*112*), which can be attributed to smaller t_{TIG} and M_{S} in the TIG (3.2 nm)/W (5 nm) structure.

Surprisingly, the switching current is as low as 6×10^{10} A/m^2 for the TIG (9.6 nm)/W (5 nm), which is still three times smaller than the TIG (8 nm)/Pt (5 nm) case considering that the M_{S} and t_{TIG} are comparable (*112*). This can be understood from a larger ξ_{DL}(~ 0.02) in the TIG/W compared with the value (~ 0.01) in TIG/Pt. This suggests that the large spin Hall angle in W enables more energy efficient magnetization switching. To quantitatively understand the influence of ξ_{DL} on the switching behavior, we define the current switching efficiency as $\eta = \frac{2e\left(H_{\mathrm{k}} - H_{\mathrm{applied}}\right)M_{\mathrm{s}}t_{\mathrm{TIG}}}{\hbar J_{\mathrm{sw}}}$ (*100, 103*) for comparing TIG/W devices with different t_{TIG}, where $H_{\mathrm{applied}} \approx 135\mathrm{Oe}$ is the applied field during switching, and J_{sw} is the switching current density. Note that due to the large size of Hall bar devices, the magnetization switching is achieved through domain wall nucleation and motion and thus η is very different from ξ_{DL}. The plot of η versus ξ_{DL} in Figure 3-19(d) indicates that the increased ξ_{DL} helps improve the switching efficiency.

Here, we want to discuss the possible interfacial effects such as Rashba spin-orbit interaction (*127, 128*) at the TIG/W interface, while the previous work on the TIG/Pt assumes the SHE picture (*112*). Based on the SMR theory, T_{r} can also be theoretically estimated by using $T_{\mathrm{r}} = \mathrm{Re}\frac{2G_{\uparrow\downarrow}\lambda \tanh\frac{d}{2\lambda}}{\frac{1}{\rho}+2G_{\uparrow\downarrow}\lambda \coth\frac{d}{\lambda}}$ (*113, 114*), where ρ ($\sim 165 \pm 4\ \mu\Omega \cdot \mathrm{cm}$) is the resistivity, d is the thickness, and λ is the spin diffusion length of the W layer. We compare the values of T_{r} estimated by ξ_{DL} and SMR, which reveals a quantitative difference. This difference could be due to the existence of Rashba spin torques, which makes the contribution of the two spin current effects to ξ_{DL} and SMR complicated (*106, 129-131*). Nevertheless, the mechanism of the spin current generation will not change our qualitative picture that the T_{r} or ξ_{DL} is positively dependent on the M_{S}.

In this work, we use the same method to prepare W/TIG devices, and the only difference among three devices is t_{TIG}. So, the material combination at the interface is the same. This leads us to conclude that spin backflow (*45, 106*) and spin memory loss (*116*) do not play a major role here because they depend mostly on the material combination at the interface. The t_{TIG}-dependent M_{S} also cannot be explained by the dead layer scenario since $M_{\mathrm{s}}t_{\mathrm{TIG}}$ is not a linear function of t_{TIG}. In an ideal case, $\xi_{\mathrm{DL}} \propto M_{\mathrm{s}}^2$. The deviation from the quadratic dependence in this work could be because of thickness-dependent crystallinity of TIG and measurement uncertainty.

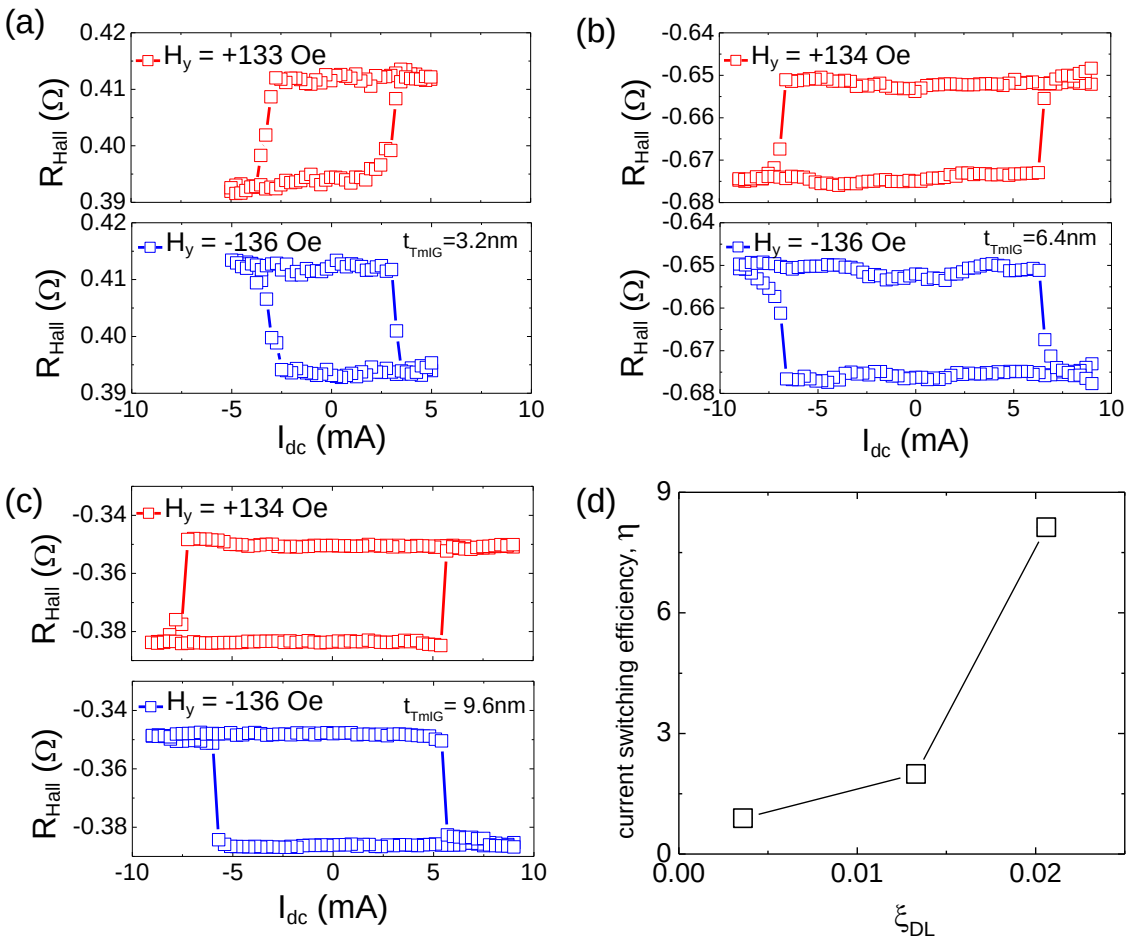

Figure 3-19. Current-induced magnetization switching in TIG/W with different TIG thicknesses. (a-c) Current-induced switching for TIG with thickness 3.2 nm (a), 6.4 nm (b) and 9.6 nm (c) in the presence of a magnetic field along and against the current direction. The switching is done by applying a 5 ms pulse with varying current amplitude. (d) Current switching efficiency estimated from the total magnetic angular momentum over switching current density versus damping-like torque efficiency.

3.3. Spintronics in Graphene and Topological Insulator

3.3.1. Introduction to Graphene and Topological Insulator

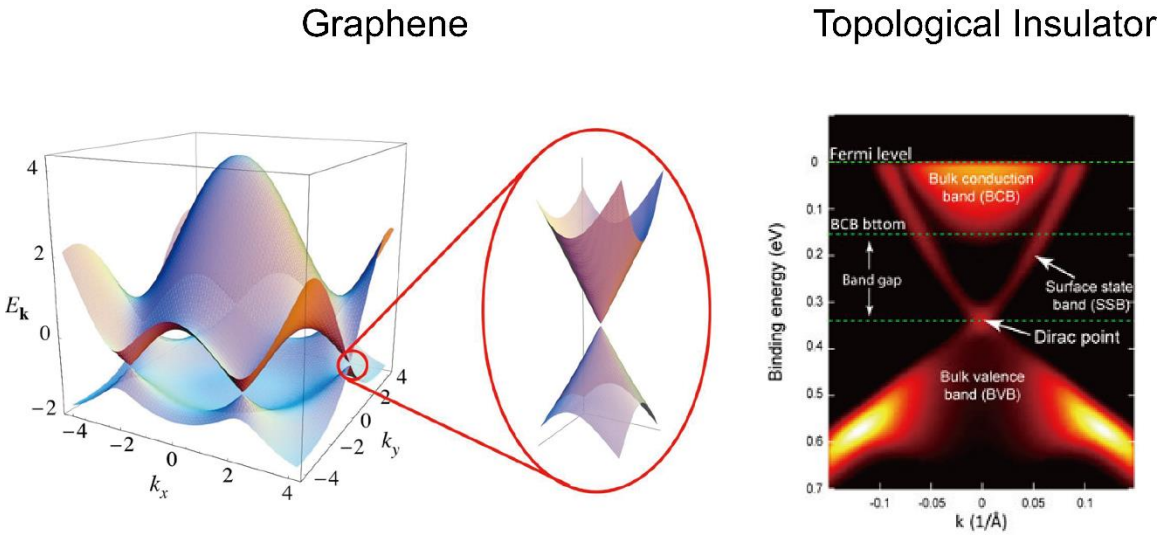

Figure 3-20. The band structure of graphene and topological insulator. Left: The electronic dispersion of graphene. Zoom in: the linear dispersion relation near the Dirac points in the honeycomb lattice. Adapted from A. Neto *et al*. Rev. Mod. Phys. 81, 109 (2009). Right: ARPES measurement of the band structure of topological insulator (here Bi_2Te_3) with an energy band gap in the bulk states and a sharp V-shape linear dispersion in the surface state band. Adapted from Y. Chen *et al*. Science 325, 5938 (2009).

Graphene and the surface states of TIs are the well-known two-dimensional (2D) electron systems described by massless Dirac equations, thus also named as 2D Dirac systems(*132*). Because of their unique band structures, both have superior electronic properties, such as the exceedingly high mobility in graphene and spin-momentum locked feature in TI surface states. Introducing the spin degree of freedom in both materials attracts a great deal of attention in recent spintronics research. The distinct difference in graphene and TI is the intrinsic SOC strength, although they share the similar

Hamiltonian. Graphene possesses long spin relaxation time due to the relative weak SOC and TI is extraordinarily efficient in terms of spin-to-charge conversion as being a superb spin current detector.

Graphene is a single layer of carbon atoms tightly packed into a 2D honeycomb lattice. From the perspective of its electronic properties, the fermions in graphene mimic the relativistic particles and are described by Dirac-like Hamiltonian(*133*):

$$\vec{H} = \hbar v_F \begin{pmatrix} 0 & k_x - ik_y \\ k_x + ik_y & 0 \end{pmatrix} = \hbar v_F \boldsymbol{\sigma} \cdot \boldsymbol{k}$$

where $\boldsymbol{k}$ is the quasiparticle momentum, $\boldsymbol{\sigma}$ the 2D Pauli matrix and $v_F \sim 1 \times 10^6\ m/s$ the *k*-independent Fermi velocity. As shown in Figure 3-20 left, the valence band and conduction band meet at K and K' points, knowns as the Dirac points (DPs). K and K' denotes two sublattices, giving rise to valley degeneracy of 2. The energy dispersion shows a linear spectrum $E = \hbar v_F k$ near the DP, considered as the essential feature of the graphene band structure. Graphene's superb quality clearly reveals itself in a pronounced ambipolar electric field effect such that charge carriers can be tuned continuously from electrons to holes with the mobility exceeding 15, 000 $cm^2V^{-1}s^{-1}$(*133*). The recent development in utilizing hexagonal boron nitride (h-BN) as an appealing substrate owing to its similar lattice structure with graphene and large electronic bandgap has elevated the mobility of graphene easily reaches the order of 100,000 $cm^2V^{-1}s^{-1}$(*134*). The hallmark of graphene as a consequence of the topologically exceptional electronic structure is the half-integer quantum Hall effect(*6, 7*). The Hall conductivity σ_{xy} persists through the DP and the sequence is shifted with respect to the conventional QHE by ½, so that $\sigma_{xy} =$

$\pm 4e^2/h(N+\frac{1}{2})$ where N is the landau level (LL) index and the factor 4 appears due to the double valley and double spin degeneracy.

Three dimensional (3D) TI is a new type of quantum matter in which bulk is insulating but the surface is conducting. In the topologically nontrivial phase, the bulk states are fully gapped, but the surface states are time-reversal symmetry protected exhibiting single massless Dirac type of dispersion relation, as indicated by the angle-resolved photoemission spectroscopy (ARPES) data in the Figure 3-20 right, analogous to graphene but differ in some essential aspects(*132*). First, the 2D massless Dirac fermions in TI is helical, in the sense that the spins of electrons are orthogonally locked to the momentum, forming a left-handed helical texture in momentum space(*135*). Second, there is only one conduction- and valence- band surface state at each 2D momentum in TI while graphene has the degeneracy of 4 from valley and spin.

The unique electronic band structure features by 2D Dirac systems in graphene and TI surface states provides them with great potential in spintronics application. Despite the fact that graphene has weak intrinsic SOC strength, introducing the Rashba SOC by breaking the inversion symmetry in graphene has already proved been possible by hydrogenation(*136*) or proximity coupling with transition metal dichalcogenides (TMD)(*40, 41*) making graphene not only suitable for spin-conserver but also spin generator or detector(*132*).

3.3.2. Proximity Induced Magnetism in Graphene

3.3.2.1. YIG/Graphene/PMMA

Although pristine graphene sheets only exhibit Laudau orbital diamagnetism, local magnetic moments can be introduced in a variety of forms, e.g. along the edges of nanoribbons (*137*) around vacancies (*138*) and adatoms (*139*). However, a long-range ferromagnetic order in graphene does not occur without exchange coupling between the local moments. In general, introducing local moments and the exchange interaction in bulk materials can be simultaneously accomplished by doping atoms with unfilled *d*- or *f*-shells (*140*). For graphene, scattering caused by random impurities could be detrimental to its high carrier mobility, a unique electronic property that should be preserved. By coupling the single atomic sheet of carbons with a magnetic insulator film, e.g. YIG, we may introduce ferromagnetism in graphene without sacrificing its excellent transport properties. The hybridization between the π-orbitals in graphene and the nearby spin-polarized *d*-orbitals in magnetic insulators gives rise to the exchange interaction required for long-range ferromagnetic ordering. On the other hand, such proximity coupling does not bring unnecessary disorder to graphene. In addition, unlike ferromagnetic metals that could in principle mediate proximity exchange coupling, the insulating material does not shunt current away from graphene. In this work, we demonstrate ferromagnetic graphene via the proximity effect and directly probe the ferromagnetism by measuring the AHE.

To bring graphene in contact with YIG substrates, we apply a previously developed transfer technique, shown in Figure 3-21, that is capable of transferring pre-fabricated functional graphene devices to any target substrates (*141*). We first fabricate

exfoliated single-layer graphene devices on 290 nm-thick SiO_2 atop highly doped Si substrates using

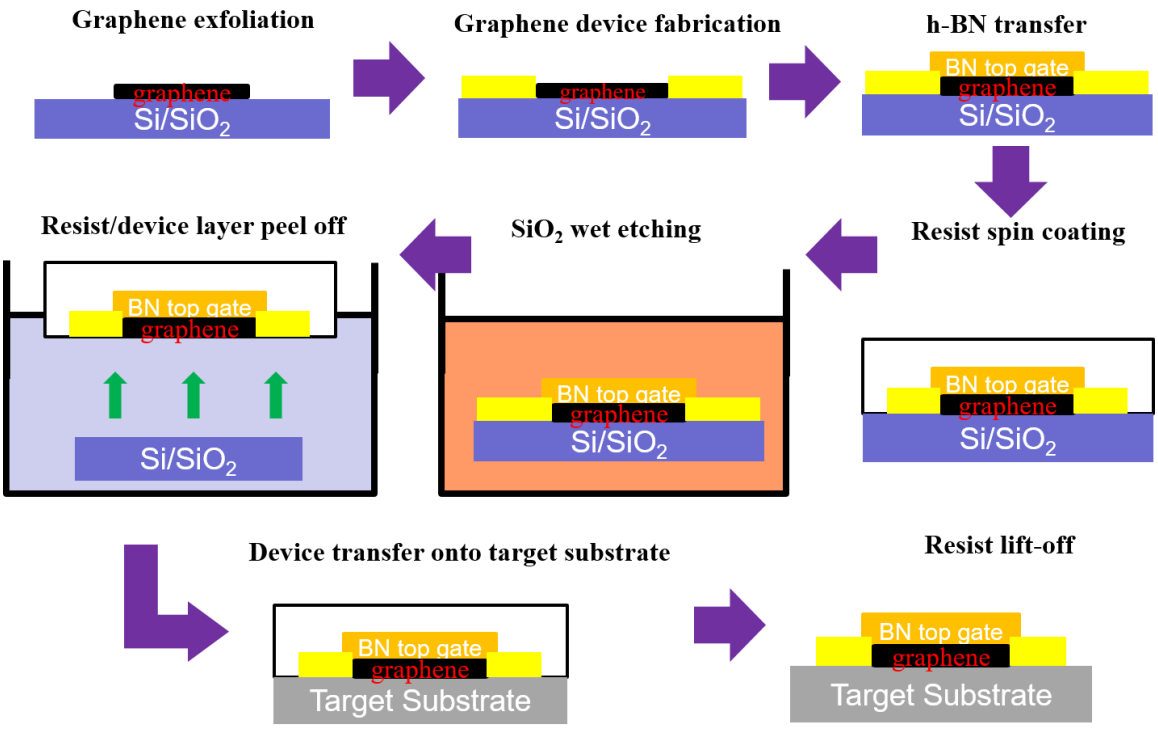

Figure 3-21. Wet transfer technique to move fabricated graphene devices to YIG.

standard electron-beam lithography and Au electron-beam evaporation. Both longitudinal and Hall resistivities are measured at room temperature to characterize the state of the pre-transferred devices. To transfer selected devices, we spin-coat the chip with poly-methyl methacrylate (PMMA) followed by a hard bake at 170 °C for 10 minutes. The entire chip is then soaked in 1 M NaOH solution for two days to etch away SiO_2 so that the device/PMMA layer is released from the substrate. The PMMA layer attached with the fully nano-fabricated graphene devices is then placed on the target substrate. Finally,

the PMMA is dissolved with acetone followed by careful rinsing and drying, and the device is ready for electrical transport and/or Raman measurements. This technique was previously applied to fabricate graphene devices on $SrTiO_3$, a high nominal dielectric constant pervoskite material (*141, 142*).

For this study, ~ 20 nm thick atomically flat YIG films are grown epitaxially on 0.5 nm-thick GGG substrates by pulsed laser deposition(*69*), which are then subsequently annealed in an oxygen-flow furnace at 850 °C for 6 hours to minimize oxygen deficiency. Magnetic hysteresis loop measurements and AFM are performed to characterize the magnetic properties and the morphology of YIG films, respectively. The hysteresis loops of a representative YIG sample are displayed in Figure 3-22(a). The YIG film clearly shows in-plane magnetic anisotropy. The in-plane coercive field and saturation field are both small (~ a few G and < 20 G, respectively), and the out-of-plane loop indicates a typical hard-axis behavior with a saturation field ~2000 G, which can vary from 1500 to 2500 G in different YIG samples. Figure 3-22(a) inset shows the AFM topographic image of a typical YIG film. The nearly parallel lines are terraces separated by steps with the atomic height and the roughness on the terrace is ~ 0.06 nm. The smoothness of the YIG surface is not only critical to a strong induced proximity effect in graphene, but also favorable for maintaining high carrier mobility (*143*).

In order to effectively tune the carrier density in YIG/graphene, we fabricate a thin methyl methacrylate (MMA) or PMMA top gate. Figure 3-22(b) shows a false-colored optical image of a graphene device on GGG/YIG before the top gate is fabricated. Room-temperature Raman spectroscopy is performed at different stages of the

device fabrication. Representative spectra are shown in Figure 3-22(c) for the same graphene device on SiO_2 (before transfer) and YIG (after transfer), and for GGG/YIG only. YIG/graphene shows both the characteristic E_{2g} (~1580 cm^{-1}) and *2D* peaks (~2700 cm^{-1}) of single-layer graphene as well as YIG's own peaks, suggesting successful transfer. We also note that the transfer process does not produce any measurable *D* peak (~1350 cm^{-1}) associated with defects (*144*). Figure 3-22(d) is a schematic drawing of a top-gated transferred device on GGG/YIG.

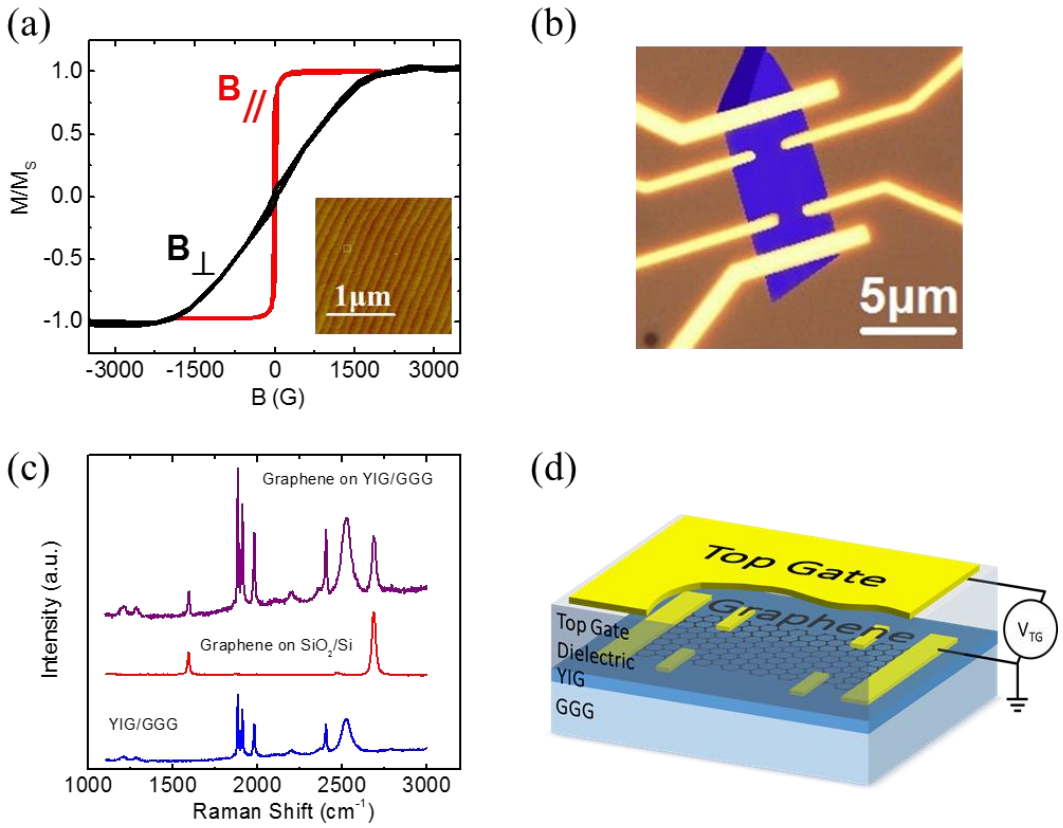

Figure 3-22. **The characterization and schematic illustration of YIG/Graphene.** (a) Magnetic hysteresis loops in perpendicular and in-plane magnetic fields. Inset is the AFM topographic image of YIG thin film surface. (b) Optical image (without top gate) and (d) schematic drawing (with top gate) of the devices after transferred to GGG/YIG substrate (false color). (c) Room temperature Raman spectra of YIG/graphene (purple), SiO_2/graphene (red), and GGG/YIG substrate only (blue).

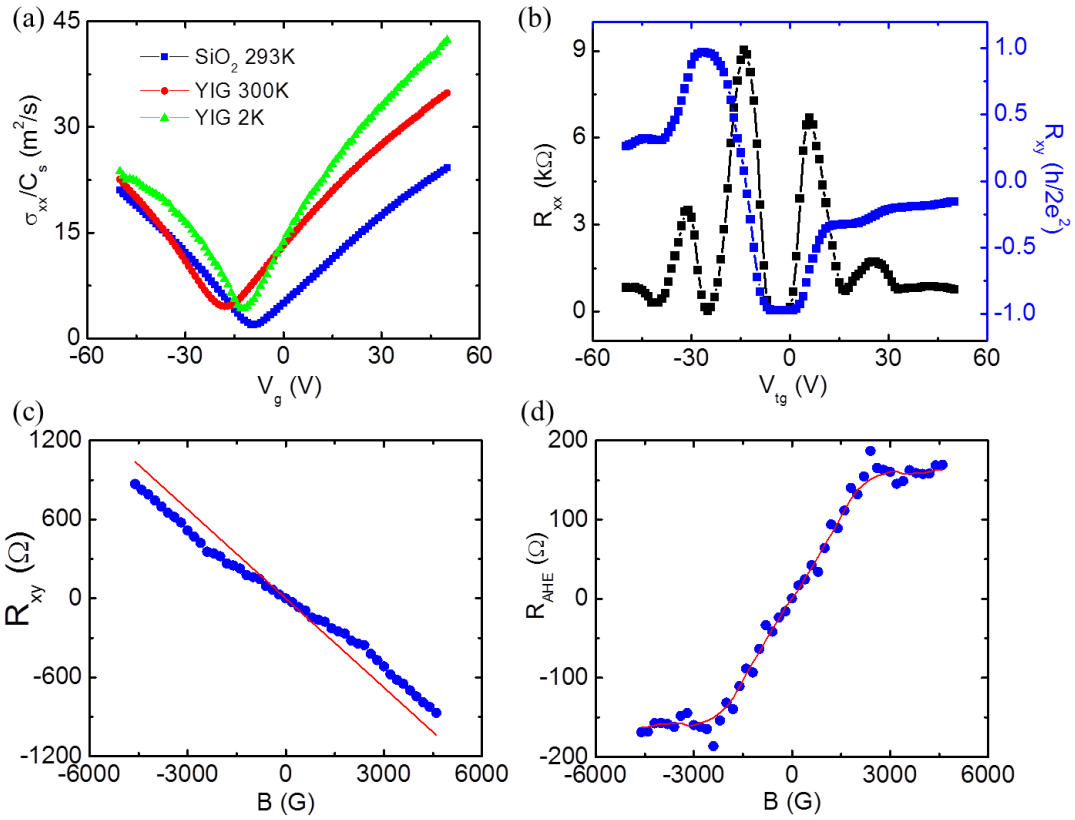

Figure 3-23. **The transport signatures of YIG/Graphene.** (a) The gate voltage dependence of the device conductivity scaled by the capacitance per unit area for the pre-transfer (293 K, black) and transferred devices (300 K, red; 2 K, green) with the same graphene sheet. (b) Quantum Hall effect of transferred YIG/graphene device in an 8 T perpendicular magnetic field at 2 K. (c) The measured total Hall resistivity data at 2 K with a straight line indicating the ordinary Hall background. (d) The nonlinear Hall resistivity after the linear background is removed from the data in (c).

Low-temperature transport measurements are performed in Quantum Design's Physical Property Measurement System. Figure 3-23(a) is a plot of the gate voltage dependence of the four-terminal electrical conductivity scaled by the effective capacitance per unit area, C_s. Since different gate dielectrics are used in the back- and top-gated graphene devices, C_s is calculated based on the quantum Hall data which agrees with the calculated value using the nominal dielectric constant and the measured

dielectric film thickness. Before transfer, the Dirac point is at ~ -9 V and the field-effect mobility is ~ 6000 $cm^2/V{\cdot}s$. After transfer, the Dirac point is shifted to ~ -18 V. The slope of the σ_{xx}/C_s vs. V_g curve increases somewhat, indicating slightly higher mobility, which suggests that the transfer process, the YIG substrate, and the top-gate dielectric do not cause any adverse effect on graphene mobility. At 2 K, the mobility improves further, exceeding 10000 $cm^2/V{\cdot}s$ on the electron side. Well-defined longitudinal resistance peaks and quantum Hall plateaus are both present at 8 T as shown in Figure 3-23(b), another indication of uncompromised device quality after transfer. In approximately 8 devices studied, we find that the mobility of YIG/graphene is either comparable with or better than that of graphene/SiO_2.

To study the proximity-induced magnetism in graphene, we perform the Hall effect measurements in the field range where the magnetization of YIG rotates out of plane over a wide range of temperatures. Nearly all YIG/graphene devices exhibit similar nonlinear behavior at low temperatures as shown in Figure 3-23(c). Figure 3-23(d) only shows the Hall data after the linear ordinary Hall background (the straight line in Figure 3-23(c)) is subtracted. In ferromagnets, the Hall resistivity generally consists of two parts: from the ordinary Hall effect and the AHE, i.e. $R_{xy} = R_H(B) + R_{AHE}(M) = \alpha B + \beta M$, here B being the external magnetic field, M being the magnetization component in the perpendicular direction, and α and β are two B- and M-independent parameters respectively. The B-linear term results from the Lorentz force on one type of carriers. Higher order terms can appear if there are two or more types of carriers present. The M-linear term is due to the spin-orbit coupling in ferromagnets. The observed non-linearity

in R_{xy} suggests the following three possible scenarios: the ordinary Hall effect arising from more than one type of carriers in response to the external magnetic field, the same Lorentz force related ordinary Hall effect but due to the stray magnetic field from the underlying YIG film, and AHE from spin-polarized carriers. The nonlinear Hall curves saturate at B_s ~ 2300 G, which is approximately correlated with the saturation of the YIG magnetization in Figure 3-22(a). This behavior is characteristic of AHE, i.e. $R_{AHE} \propto M_G$, where M_G is the induced magnetization of graphene. Since M_G results from the proximity coupling with the magnetization of YIG, M_{YIG}, both M_G and M_{YIG} should saturate when the external field exceeds some value. The saturation field of YIG is primarily determined by its shape anisotropy, i.e. $4\pi M_{\mathrm{YIG}}$, which should not change significantly far below the Curie temperature (550 K) of YIG. On the other hand, if it is caused by the Lorentz force on two types of carriers, the nonlinear feature would not have any correlation with M_{YIG}. These experimental facts do not support the first scenario. To further exclude the ordinary Hall effect due to the Lorentz force from stray fields from YIG, we fabricate graphene devices on Al_2O_3/YIG, in which the 5 nm thick continuous Al_2O_3 layer should have little effect on the strength of the stray field but effectively cut off the proximity coupling. We do not observe any measurable nonlinear Hall signal similar to those in companion YIG/graphene devices (Figs. S-6 and S-7 in SM). It excludes the effect of the stray field. Therefore, we attribute the nonlinear Hall signal in YIG/graphene to AHE which is due to spin-polarized carriers in ferromagnetic graphene. Further evidence will be presented when the gate voltage dependence is discussed below.

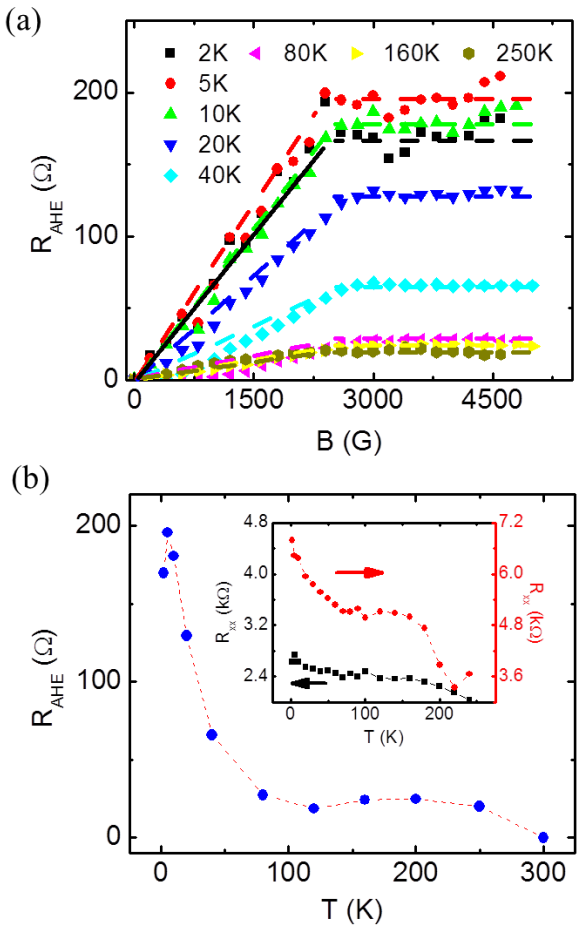

Figure 3-24. **The temperature dependence of the AHE in YIG/Graphene.** (a) AHE resistance at different temperatures. (b) The temperature dependence of AHE resistance. Inset is the longitudinal resistance at the Dirac point with no magnetic field (black) and a 1 T perpendicular magnetic field (red).

Figure 3-24(a) shows the AHE resistance, R_{AHE}, vs. the positive out-of-plane magnetic field taken from 5 to 250 K. All linear background has been removed. Figure 3-24 (b) is the extracted temperature dependence of the saturated AHE resistance. The AHE signal decreases as the temperature is increased, but it stays finite up to nearly 300 K. We note that the AHE magnitude changes sharply in the temperature range of 2 – 80 K, and then stays relatively constant above 80 K before it approaches ~ 300 K, which defines the Curie temperature of M_G. In conducting ferromagnets, the AHE resistance, R_{AHE}, scales

with the longitudinal resistance, R_{xx}, in the power-law fashion (*8*), i.e. $R_{AHE} \propto M_G R_{xx}^n$. Thus the temperature dependence of R_{AHE} could originate from M_G and/or R_{xx}. Here M_G should be a slow-varying function of the temperature below 80 K; however, the temperature dependence of R_{xx} in 1T field (inset of Figure 3-24(b)) cannot account for the steep temperature dependence of R_{AHE} either. Therefore, we attribute the discrepancy to possible physical distance change between the graphene sheet and YIG either due to an increase in the vibrational amplitude or different thermal expansion coefficients between the top-gate dielectric and GGG/YIG. We have observed variations in both the Curie temperature T_{c} for M_G and the maximum R_{AHE}. Among all 8 devices studied, the highest T_{c} is ~ 300 K and the largest R_{AHE} at 2 K is ~ 200 Ω.

With a top gate, we can control the position of the Fermi level in graphene at a fixed temperature, not possible in ferromagnetic metals. By sweeping the top-gate voltage, V_{tg}, we systematically vary both R_{AHE} and R_{xx} and keep the induced magnetization and exchange coupling strength unchanged. More importantly, by changing the carrier type, a sign reversal occurs in the ordinary Hall, i.e. the slope of the linear background signal. We remove this carrier density dependent linear background for each gate voltage and obtain the AHE signal. Figure 3-25(a) is the AHE resistivity of a device measured at 20 K for several V_{tg}*'s*: 60 V (red squares), 0 V (green circles), and -20 V (blue triangles), respectively. The inset shows the V_{tg}-dependence of the resistivity. The Dirac point is at ~35 V; therefore, carriers are predominately electrons at 60 V with a density ~ 2.5×10^{11} cm^{-2}, but predominately holes at both 0 and -20 V. We deliberately avoid the region close to the Dirac point where both electrons and holes coexist and the

ordinary Hall signal acquires high-order terms in *B*. In the gate dependence data, it is important to note that the AHE sign remains unchanged regardless of the carrier type. This is strong evidence that the observed nonlinear Hall signal is not due to the ordinary Hall effect from two types of carriers, either from the external or stray field, but due to the AHE contribution from spin-polarized carriers in ferromagnetic sample. In addition, the resistance at 60 V is the highest among the three, followed by that at 0 V, and then -20 V, and the corresponding R_{AHE} magnitude follows the same order.

To further reveal the physical origin of AHE, we now focus on the relationship between R_{AHE} and R_{xx} as V_{tg} is tuned. Figure 3-25(b) shows more gate-tuned AHE data in another top-gated device measured at 2 K. We also exclude the data close to the Dirac point (-14 V for this device) for the reason mentioned above. Starting from -10 V, R_{AHE} is the largest. As V_{tg} is increased, the electron density increases, and R_{xx} decreases accordingly, which is accompanied by a steady decrease in R_{AHE}. Due to the negatively biased Dirac point, we cannot reach the completely hole-dominated region within the safe V_{tg} range (gate leakage current < 10 nA). On the hole side where the background is still influenced by the two-band transport, we do not observe any evidence of a sign change in R_{AHE}. In the inset we plot R_{AHE} vs. R_{xx} as V_{tg} is varied. From the slope of the straight line in the log-log plot, we obtain the exponent of the power-law: $n = 1.9 \pm 0.2$. As in many ferromagnetic conductors, the quadratic relationship indicates a scattering-independent AHE mechanism, which is different from the skew scattering induced AHE.

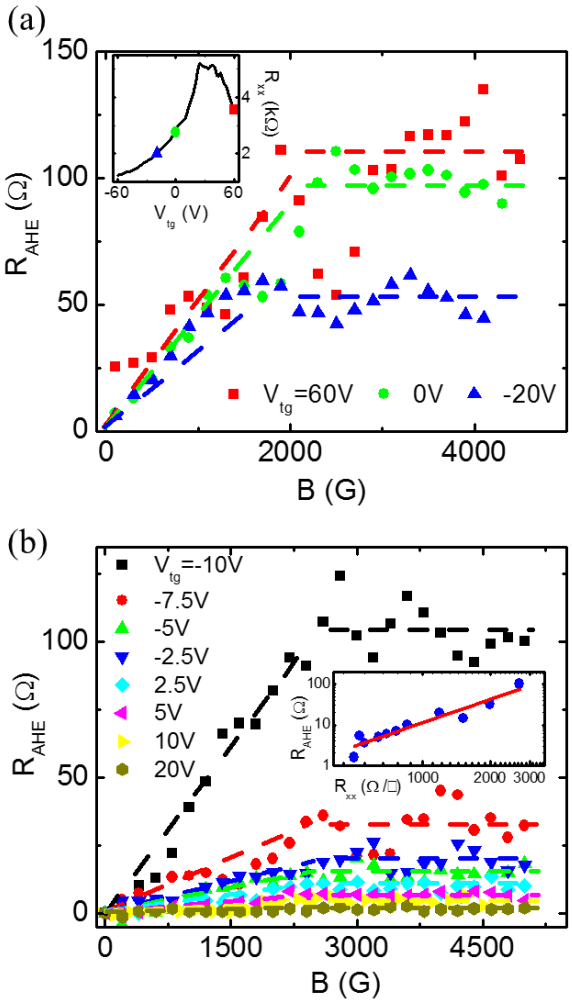

Figure 3-25. **The gate voltage dependence of the AHE in YIG/Graphene.** (a) AHE resistance with different carrier types and concentrations at 20 K. Inset, gate voltage dependence at 20 K. Red squares, green circles, and blue triangles represent 60 V, 0 V, -20 V top gate voltages, respectively. The sharp noise-like field-dependent features are reproducible. (b) Top gate voltage dependence of the AHE resistance at 2 K. Inset is the log-log plot of R_{AHE} vs. R_{xx}. Red curve is a linear fit with a slope of 1.9 ± 0.2

It is understood that a necessary ingredient for AHE is the presence of SOC along with broken time reversal symmetry (*8*). AHE can result from either intrinsic (band structure effect) or extrinsic (impurity scattering) mechanisms. Haldane showed that for a honeycomb lattice (graphene) the presence of intrinsic SOC (which breaks time reversal symmetry) can lead to quantized AHE for spin-less electrons (*145*). Since intrinsic SOC

in graphene is very weak (~10 μeV) (*146*), this effect has not been observed experimentally.

However, an enhanced Rashba SOC is possible when graphene is placed on substrates (*147, 148*) or subjected to hydrogenation (*149*) due to broken inversion symmetry. Recently, Qiao *et al.* predicted that ferromagnetic graphene with Rashba SOC should exhibit QAHE (*150, 151*). In this case, the Dirac spectrum opens up a topological gap with magnitude smaller than twice the minimum of exchange and SOC energy scale (see SM). As the Fermi level is turned into the gap, a decrease in the four-terminal resistance is expected along with a simultaneous quantization of the AHE conductivity approaching $2e^2/h$. In devices exhibiting AHE, the largest AHE at 2 K is ~ 200 Ω. Using the corresponding R_{xx} of 5230 Ω, we calculate the AHE contribution and obtain $\sigma_{AHE} \approx 7$ μS $\approx 0.09(2e^2/h)$, nearly one order of magnitude smaller than the predicted QAHE conductivity $2e^2/h$. Clearly we have not reached the QAHE regime due to the intrinsic band structure effect, indicating that the Rashba SOC strength λ_R is smaller than the disorder energy scale. From the minimum conductivity plateau, we estimate the energy scale associated with the disorder $\Delta_{dis} = \hbar/\tau \approx 12$ meV, assuming long-ranged Coulomb scattering (*152*). Therefore our experimental results suggest that $\lambda_R < 12$ meV. To observe QAHE, it is important to further improve the quality of the devices or to strengthen the Rashba SOC to fulfill $\lambda_R > \Delta_{dis}$, both of which are highly possible.

In order to understand the physical origin of the observed unquantized AHE in our devices, we calculate the intrinsic AHE (see SM) at the relevant densities for $\lambda_R < 12$ meV. Our results show that the intrinsic AHE conductivity at these densities is an order

of magnitude smaller than the observed value, which argues against the intrinsic mechanism. Since charged impurity screening in graphene becomes extremely weak as the Dirac point is approached, it is likely that the extrinsic mechanisms play a more important role here. We would like to point out that gate tunability in ferromagnetic graphene allows for the observation of Fermi energy dependence of the AHE conductivity, which cannot be achieved in ordinary ferromagnet metals. If the carrier density can be modulated by gating, besides the exponent, the Fermi energy dependence of the AHE conductivity can be experimentally determined over a broad range of energy. This additional information can help further pinpoint the physical origin of AHE in 2D Dirac fermion systems.

3.3.2.2. YIG/Graphene/h-BN

The magnetic proximity exchange coupling induced ferromagnetism in graphene has been revealed by the anomalous Hall effect described in previous section. An important and key issue is to tune the fermi level of graphene by electrical gating into the nontrivial band gap, which is determined coherently by the exchange fields and SOC strength, to achieve the QAHE. However, using PMMA as a top gate dielectric is not the best option, since the organic layer will make the surface of graphene junky, bringing additional scattering source. Recently, the 2D van der Waals heterostructures attract a great deal of attention. By stacking multiple 2D electronic materials, it introduces new properties into the system without disturbing the quality. Among them, h-BN has made graphene advance to a new level with even more pronouncing properties, such as the

extraordinary high mobility reaching 100, 000 cm^2/Vs (*134, 153*). Since h-BN has very similar lattice structure with graphene, the graphene that sandwiched between two h-BN sheets can reach mobility at the order of 100, 000 cm^2/Vs at room temperature. Because h-BN also has a large electronic bandgap, it can serve as a dielectric material to gate the graphene devices. By taking advantage of these two unique properties of h-BN, we followed the similar method described in previous section to wet transfer graphene/h-BN device on YIG with top gating electrodes on top of h-BN.

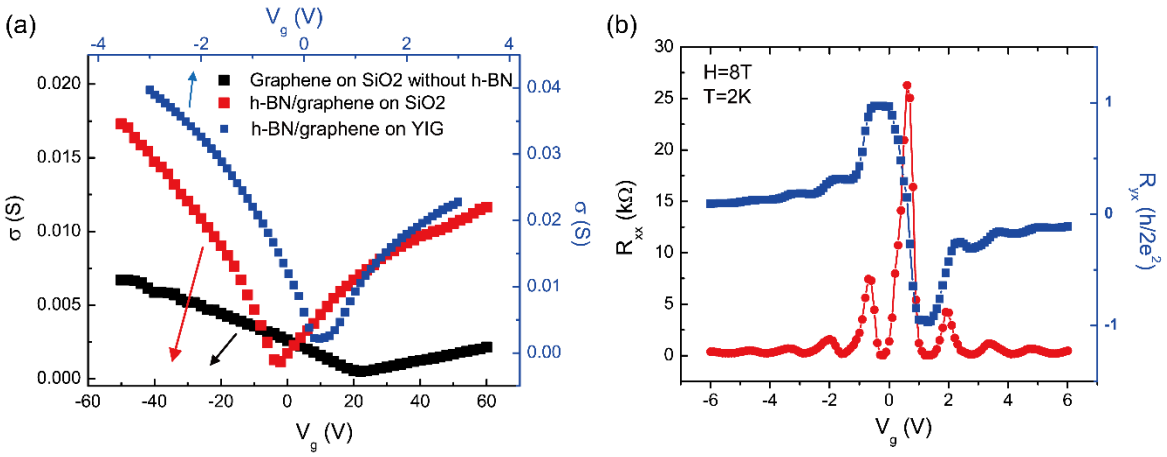

Figure 3-26. The transport signatures of YIG/Graphene/h-BN. (a) The gate voltage dependence of the device conductivity with the same graphene sheet on SiO_2 prior to h-BN top gate dielectric sheet transfer (black), after BN transfer (red) and on YIG film (blue) (b) Quantum Hall effect of transferred YIG/graphene/h-BN device in an 8 T perpendicular magnetic field at 2 K.

As shown in the Figure 3-26(a), the graphene mobility on SiO_2 prior to the transfer of h-BN is usually around 5, 000 cm^2/Vs at room temperature. By transferring h-BN sheet with thickness ranging from 10 ~ 30 nm, the graphene/h-BN devices on the same SiO_2 substrate shows 6 times increase of mobility, reaching 30, 000 cm^2/Vs, characterized by the slope of gate dependence of sheet conductance. The graphene/h-BN

on YIG after wet transfer has a similar mobility as it on SiO_2. Note that the gating efficiency is also greatly improved with h-BN as a top gate dielectric. Much smaller applied gate voltage (decreased by a factor of 15) is needed to tune the carrier density over a wide range, due to the thin h-BN sheet. The YIG/graphene/h-BN quality is further confirmed by reproducing the half-integer QHE at 2 K under an 8 T magnetic field. Well-defined quantum Hall plateaus are resolved following the exact filling factors $\pm 2, \pm 4, \pm 6$ and the longitudinal sheet resistance drops to 0 with negligible residue resistance, indicating the high quality of graphene devices without being disturbed by the wet transfer process.

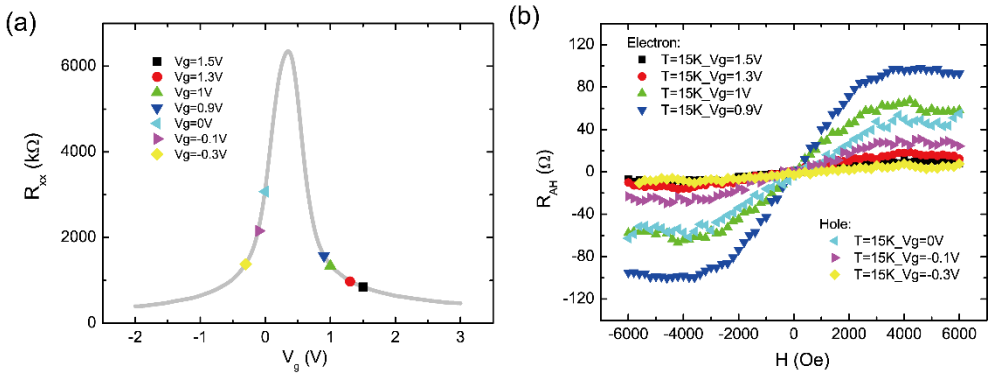

Figure 3-27. **The anomalous Hall effects of YIG/Graphene/h-BN.** (a) The gate dependence of the longitudinal sheet resistance of graphene sandwiched between YIG and h-BN. (b) The anomalous Hall effect at 15 K under different top gate voltages. (c) The anomalous Hall effects of YIG/Graphene/h-BN at different temperatures under the same V_g = 0V. (d) The temperature dependence of anomalous Hall resistance indicating a Curie temperature of 308 K.

Figure 3-27 (a) shows the top gate dependence of the graphene sheet resistance R_{xx} with DP around 0.5 V. In order to check the anomalous Hall characteristic on both electron and hole carrier type, gate voltages are selected away from the two-band region near the DP and distributed on both sides of DP. Figure 3-27 (b) shows the anomalous

Hall effects observed in YIG/graphene/h-BN for the chosen gate voltages. Two points should be emphasized. First, the AHE remains the same sign when carrier type is tuned from hole to electron, immediately ruled out the stray field or two band induced nonlinear curvature. Second, the anomalous Hall resistance R_{AH} increases when the fermi level approaches the DP. As discussed in previous section, R_{AH} scales with the sheet resistance. To further explore the nature of fermi level dependent anomalous Hal conductance, the anomalous Hall conductance σ_{AH} at various gate voltages is plotted in Figure 3-28. The maximum σ_{AH} reaches ¼ of quantum anomalous Hall conductance $2e^2/h$, 5 orders enhancement compared with previous devices, possibly indicating a larger gap opening at the DP of graphene by a stronger exchange fields between graphene and YIG or an enhanced Rashba SOC in the heterostructure.

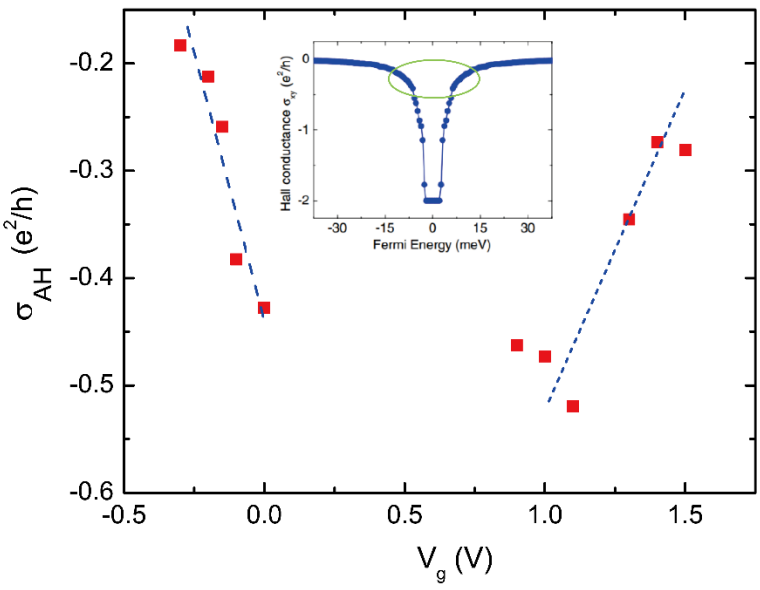

Figure 3-28. The calculated anomalous Hall resistance as a function of gate dependence. Inset: The quantum Hall conductance predicted in graphene. Inset figure adapted from Z. Qiao *et al*. Phys. Rev. Lett. 112, 116404 (2014).

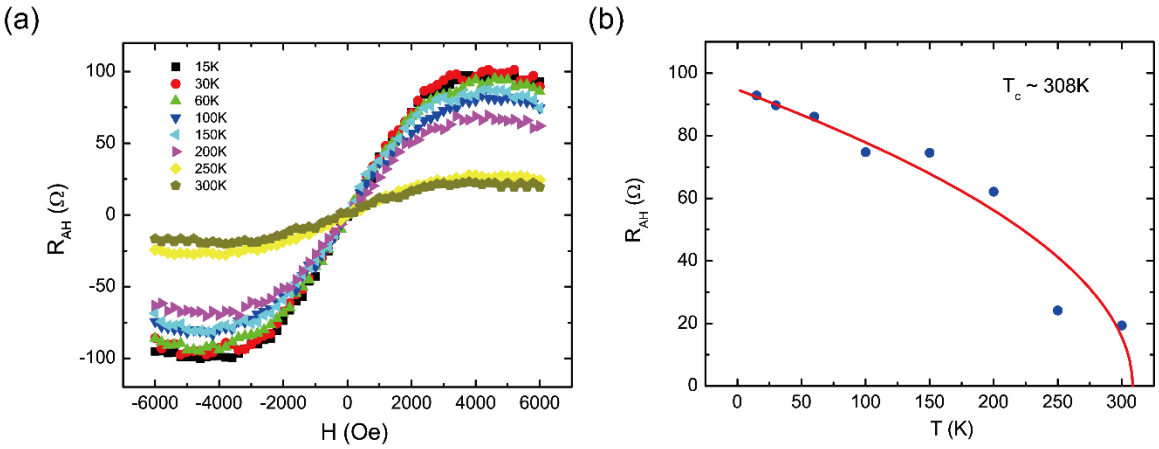

Figure 3-29. **The anomalous Hall effects of YIG/Graphene/h-BN.** (a) The gate dependence of the longitudinal sheet resistance of graphene sandwiched between YIG and h-BN. (b) The anomalous Hall effect at 15 K under different top gate voltages. (c) The anomalous Hall effects of YIG/Graphene/h-BN at different temperatures under the same V_g = 0V. (d) The temperature dependence of anomalous Hall resistance indicating a Curie temperature of 308 K.

To further quantitatively characterize the exchange coupling strength in YIG/graphene/h-BN, AHE in graphene is studied over a wide temperature range from 15 K to 300 K. The AHE resistance drops when temperature increases but still persists up to 300 K. By fitting the AHE resistance in function of temperature in a naive model of Curie-Weiss, one can extract the Curie temperature of proximity induced magnetism in graphene is near 308 K, around 27 meV in terms of exchange coupling energy.

Since the AHE in the YIG/graphene with in-plane magnetic anisotropy, nonlinear curvature of Hall effect caused by two band carriers prevent accurate determination of the AHE in this system. Further investigation includes replacing YIG with TIG, a high *Tc*-ferrimagnetic insulator with strong PMA, and inserting a TMD layer such as WSe_2 to further improve the Rashba SOC in graphene. Both directions aim to open up a nontrivial topological bandgap in the DP of graphene and realize the QAHE in graphene.

3.3.3. Above 400 K Perpendicular Ferromagnetic Phase in Topological Insulator

The discovery of the QAHE in magnetically-doped TI has spurred a great deal of excitement in the study of the topological state of matter (*10, 11, 154*). Unlike the well-known quantum Hall effect or regular AHE, the remarkable QAHE state is characterized by the quantized Hall conductance $\pm e^2/h$ and dissipation-less chiral edge-current transport in the absence of any external magnetic field. Furthermore, in the QAHE state the chiral edge-charge current simultaneously carries a large and electrically tunable spin polarization due to strong spin-orbit coupling in TI (*155*). These attractive properties make QAHE materials strong candidates for next generation spintronic applications at the nanoscale.

An essential pre-requisite for the QAHE to occur is an exchange interaction that breaks the time-reversal symmetry in TI (*10, 156*). In magnetically-doped TI, exchange interaction originates from the long-range ferromagnetic order of magnetic moments carried by transition metal dopants such as Cr, V and Mn (*11, 154, 157*). The spontaneous magnetic order leads to an exchange gap at the Dirac point of TI, which consequently gives rise to the QAHE. Hence, the ultimate upper temperature limit of the QAHE is dictated by the Curie temperature (T_c) of the magnetic TI. In the optimal Cr- or V-doped TI samples that exhibit QAHE, T_c can be as high as 30 K, but the QAHE only occurs at much lower temperature, i.e. at or well below 2 K (*11, 154, 158-160*). While the origin of this large discrepancy is an interesting topic for further investigation, it is imperative to drastically raise the T_c and therefore greatly increase the exchange-induced gap, to ultimately realize QAHE at elevated temperatures.

One possible route to higher T_c is to continue optimizing the transition-metal doping approach, similar to previous efforts in dilute magnetic semiconductor research (*161*). However, raising T_c requires increasing the doping level, which inevitably lowers sample quality with the presence of extensive disorder, or even destroys the nontrivial surface states due to weakened spin-orbit coupling (*39*). An alternative route is to leverage the proximity effect to couple the TI surface states directly to a high-T_c magnetic insulator without introducing spin disorder due to randomly doped magnetic moments to either bulk or surface states. The latter approach has an obvious advantage of independent optimization of both electronic and magnetic properties (*162*), which is impossible in the first approach. Recent progress in this direction, including TI/EuS (*163-166*), YIG/TI (*162*, *167-169*) and CrSb/TI (*170*) heterostructures, indicates its feasibility. However, while induced exchange interaction is necessary for QAHE, the in-plane magnetization in a system such as YIG/TI does not open an exchange gap in the TI surface electronic states unless reflection symmetry is broken (*171*). In this *Report*, we demonstrate induced ferromagnetism in TI with perpendicular magnetic anisotropy, as manifested by sharp and squared AHE hysteresis loops, using a high-T_c (~ 560 K) ferrimagnetic insulator, namely, $Tm_3Fe_5O_{12}$ or TIG. In addition, the perpendicular ferromagnetic phase in TI persists well above 400 K, which is more than one order of magnitude higher than the T_c of the optimal magnetically-doped TI exhibiting QAHE. These unique features entail a much larger exchange gap in TI without requiring any external magnetic field.

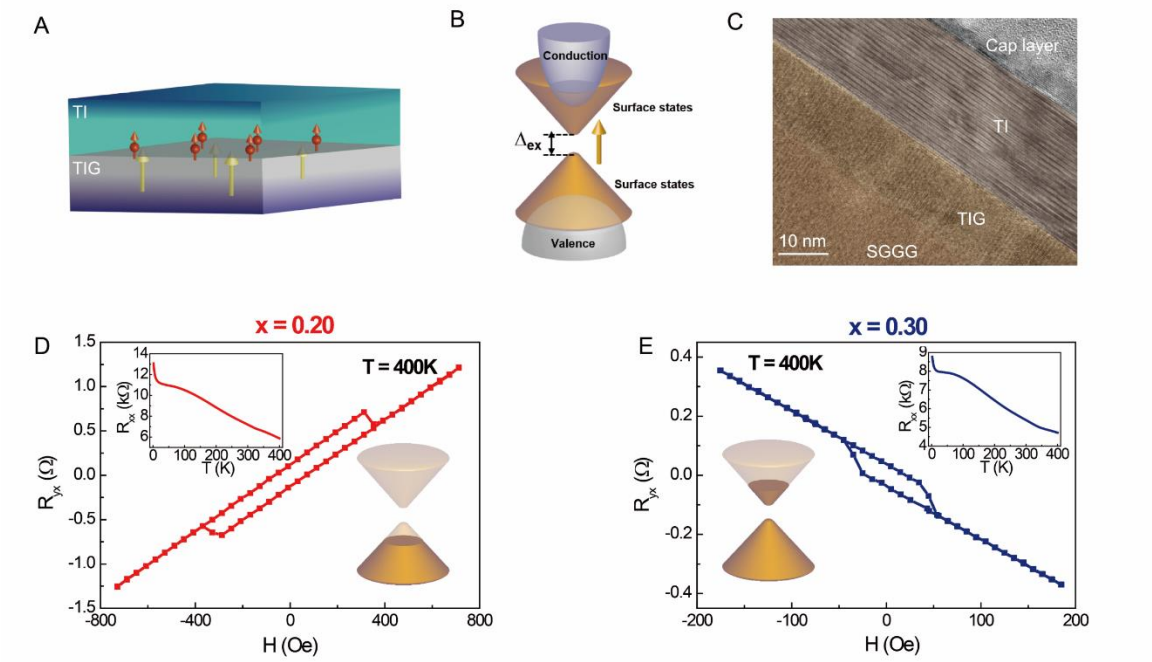

Figure 3-30. Proximity-induced ferromagnetism and anomalous Hall effect at 400 K in TIG/TI heterostructure. A. Schematic drawing of proximity coupling between TI and TIG. B. Exchange gap at the charge neutral point of TI surface states induced by broken time reversal symmetry. C. HRTEM image of a TIG/TI (20 QL) bilayer structure. D & E. Hall traces of TIG/$(Bi_xSb_{1-x})_2Te_3$ (5 QL) for x = 0.20 and x = 0.30, respectively. The upper insets show the corresponding temperature dependence of R_{xx}. The lower insets show schematic drawings of the corresponding chemical potential position.

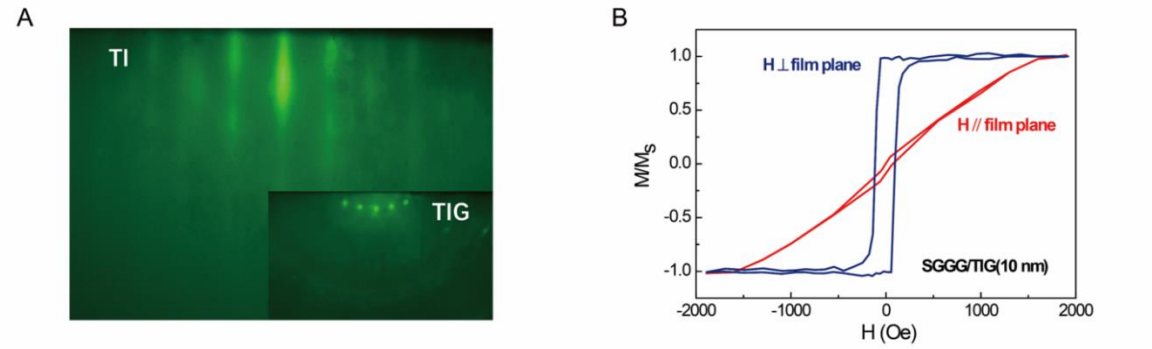

Figure 3-31. A. RHEED pattern of a typical TI film grown on TIG. Inset: RHEED pattern for 10 nm TIG on SGGG. B. Magnetic hysteresis of a 10 nm TIG film for both field perpendicular and parallel to the film plane at 300 K, indicating a strong perpendicular magnetic anisotropy.

Similar to the YIG films in previous studies (*162, 167*), TIG is a rare-earth garnet with ferrimagnetism originating from the anti-ferromagnetically coupled iron magnetic moments via super-exchange interaction. To ensure high heterostructure quality, we first prepare atomically flat TIG surfaces while engineering the needed perpendicular magnetic anisotropy. This is accomplished by epitaxial growth of TIG films on (111)-oriented SGGG substrates with pulsed laser deposition (*47, 58*). Due to the negative magnetostriction constant of TIG, the interface tensile strain exerted by SGGG produces perpendicular magnetic anisotropy (*58*). The root-mean-square surface roughness in 10-nm-thick TIG films can be as low as ~ 1.2 Å. Meanwhile, the resulting perpendicular anisotropy is sufficiently strong to drive the magnetization in the direction normal to the film plane without any external magnetic field. TIG/TI heterostructures are subsequently fabricated by growing a five quintuple-layer (QL) thick $(Bi_xSb_{1-x})_2Te_3$ TI film atop TIG using molecular beam epitaxy (MBE) (*162, 167, 172*). These TI films show excellent structural quality, as confirmed by *in situ* RHEED patterns (see Figure 3-31A). *Ex situ* HRTEM does not show any visible interfacial defects or additional phases (Figure 3-30C).

The chemical potential of the TI films can be controlled by varying the Bi:Sb ratio, as demonstrated previously (*173*). To study the effect of carrier type on interface ferromagnetism, we deliberately choose two ratios, x=0.20 and x=0.30, in order to place the chemical potential just below and above the Dirac point, respectively. Both films behave as bulk semiconductors with the chemical potential inside the bulk gap, as indicated by the typical temperature dependence of the longitudinal sheet resistance (R_{xx})

(*173*), as shown in the insets of Figure 3-30 D and E. Figure 3-30 D and E show Hall traces of these two samples measured at 400 K. Besides the clear hysteresis loops, which are further discussed below, the linear ordinary Hall background indicates opposite carrier types in these two samples, with hole carrier density (n_{2D}) of 3.3×10^{13} cm^{-2} for x=0.20 and electron n_{2D} of 3.5×10^{13} cm^{-2} for x=0.30 at T=400 K. In consideration of the carrier densities below 1×10^{13} cm^{-2} at T=2 K and the thermally excited additional carriers at higher temperatures, the chemical potential is indeed located on either side of the Dirac point of the surface states but still within the bulk gap.

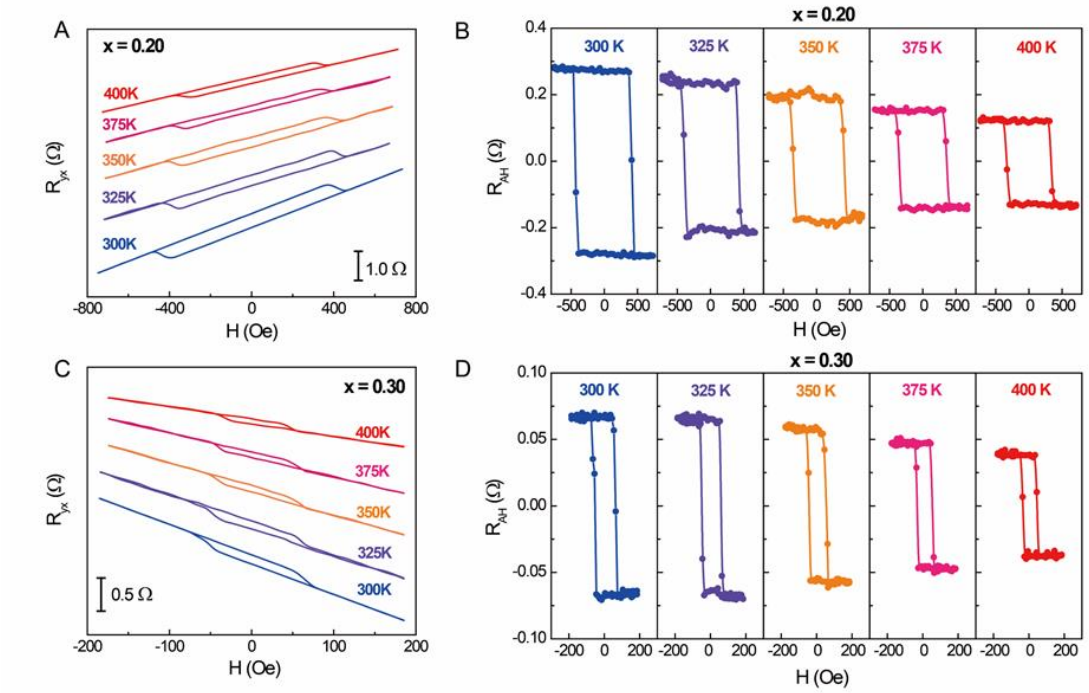

Figure 3-32. Temperature dependence of AHE response up to 400 K. A. Hall resistance of TIG/$(Bi_xSb_{1-x})_2Te_3$ (5 QL) for x = 0.20 (*p*-type) between 300 and 400 K. B. Temperature dependence of AHE loops in in A after subtracting the linear ordinary Hall background. C. Hall resistance of TIG/$(Bi_xSb_{1-x})_2Te_3$ (5 QL) for x = 0.30 (*n*-type) between 300 and 400 K. D. Temperature dependence of AHE loops in C after subtracting the linear ordinary Hall background.

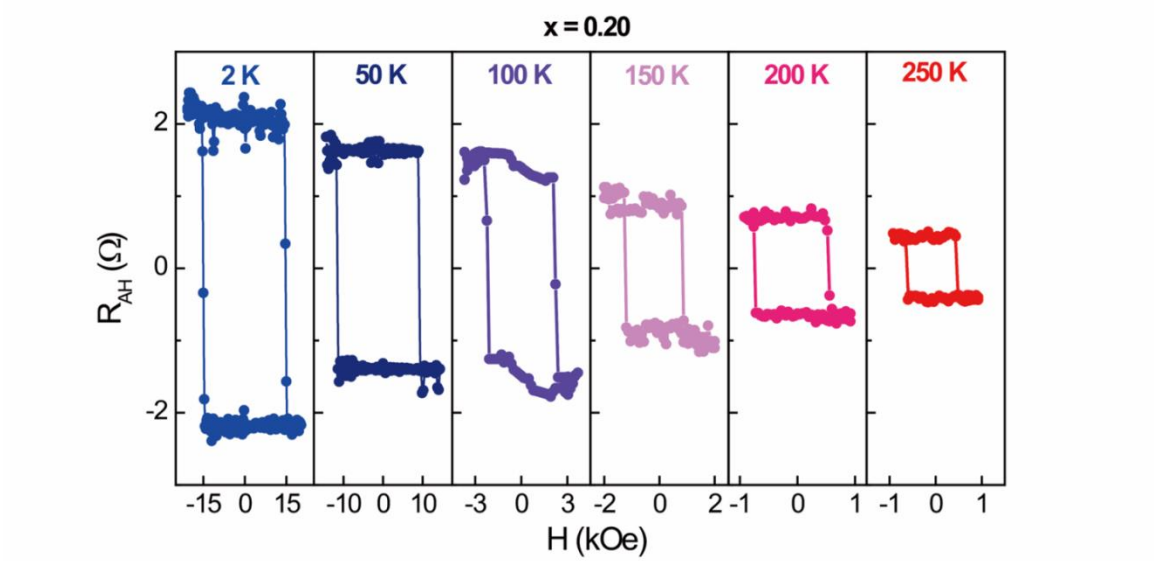

Figure 3-33. Representative low-temperature anomalous Hall resistance loops of TIG/$(Bi_xSb_{1-x})_2Te_3$ (5 QL) for x = 0.20 from 2 to 250 K.

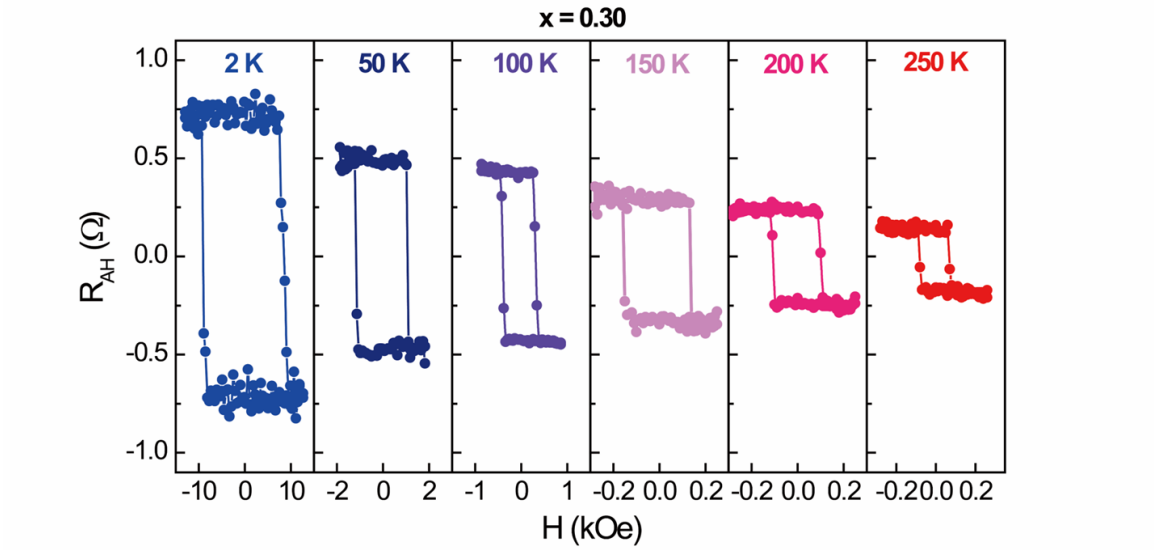

Figure 3-34. Representative low-temperature anomalous Hall resistance loops of TIG/$(Bi_xSb_{1-x})_2Te_3$ (5 QL) for x = 0.30 from 2 to 250 K.

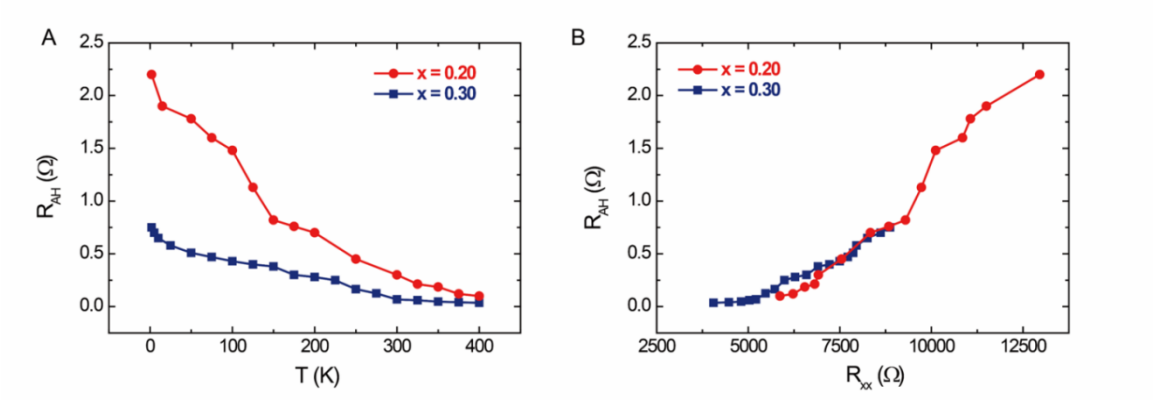

Figure 3-35. Temperature dependence of anomalous Hall resistance in TI. A. Temperature dependence of the anomalous Hall resistance R_{AH} of TIG/$(Bi_xSb_{1-x})_2Te_3$ (5 QL) for x = 0.20 and x = 0.30. B. R_{AH} vs. R_{xx} for the same samples as in A.

A squared Hall hysteresis loop, which resembles the TIG magnetic hysteresis loop taken with an out-of-plane magnetic field (Figure 3-31B), is superimposed on the linear background. In a normal ferro- or ferri-magnetic conductor, this type of loop would be the standard anomalous Hall signal characteristic of the ferromagnetism of the conductor (*174*). However, the ferrimagnet here is an insulator, and the Hall response can only come from the TI film. The hysteresis must be acquired by the bottom surface of the TI which is in direct contact with the TIG. More representative Hall loops above room temperature are presented in Figure 3-32 (low-temperature data are shown in Figure 3-33 and 3-34). The slight enhancement of the linear Hall slope at lower temperature displayed in Figs. 2A and 2C is probably caused by a shift of the chemical potential or narrowing of the Fermi-Dirac distribution function which changes the carrier density. After the linear ordinary Hall background is subtracted, the corresponding AHE hysteretic loops are displayed in Figs. 2B and 2D, respectively. The remarkable presence

of sharp and squared loops indicates a strongly preferred perpendicular magnetization direction. Clearly, such strong perpendicular anisotropy exists throughout the entire temperature range up to 400 K, the highest temperature in our measurements. It is apparent from the high temperature trend that the hysteresis extends well above 400 K, which is more than an order of magnitude higher than the record achieved in modulation-doped TI films exhibiting the QAHE (*11, 154, 158-160*). As the temperature decreases, the magnitude of the AHE resistance steadily increases but the sign remains unchanged, as shown in Figure 3-35, which is accompanied by an increase in R_{xx}. This temperature dependence is presumably due to the reduction of bulk carriers when the temperature is lowered. It is interesting to note that the coercive fields of the two samples are different. This difference was also observed in TIG/Pt samples and attributed to the coercive field variations due to the local strain variation at the SGGG/TIG interface (*58*). The increased coercive field at lower temperatures results from the magnetic anisotropy increase in TIG, likely due to an enhanced magneto-elastic coefficient at low temperatures (*175*). Importantly, the AHE loops have the same sign in these two samples despite the different carrier types. This feature immediately excludes the possibility of any Lorentz force-induced responses arising either from TIG stray fields or contributions from two types of carriers in TI.

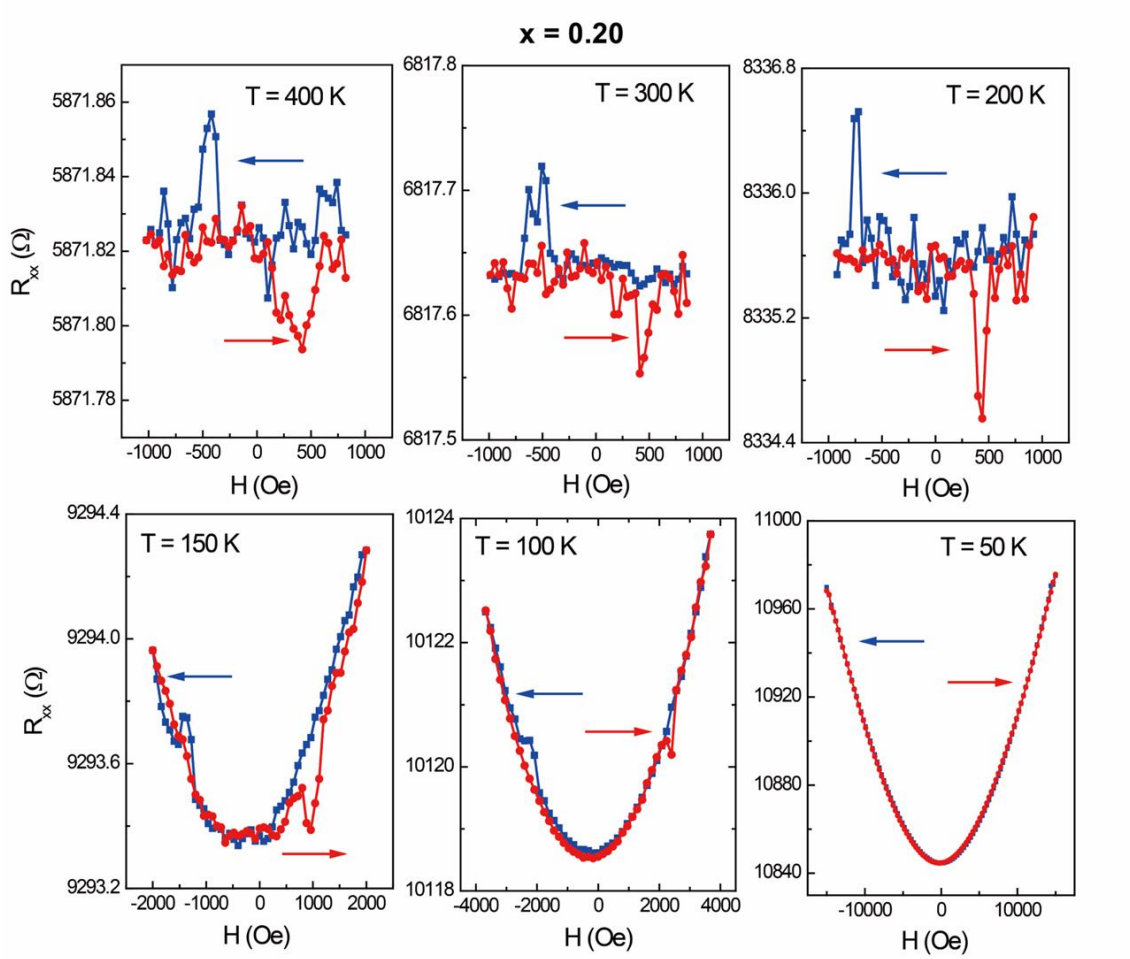

Figure 3-36. Longitudinal resistance of TIG/TI(x=0.20) sample as a function of the out-of-plane magnetic field strength at selected temperatures between 50 to 400 K. Small but reproducible features at the coercive fields appear at temperatures above 50 K. The asymmetric magnetoresistance is unlikely caused by a spin current effect but rather than by domain wall motion during the magnetization reversal, which can only be possible if the TI surface layer is magnetized by proximity coupling.

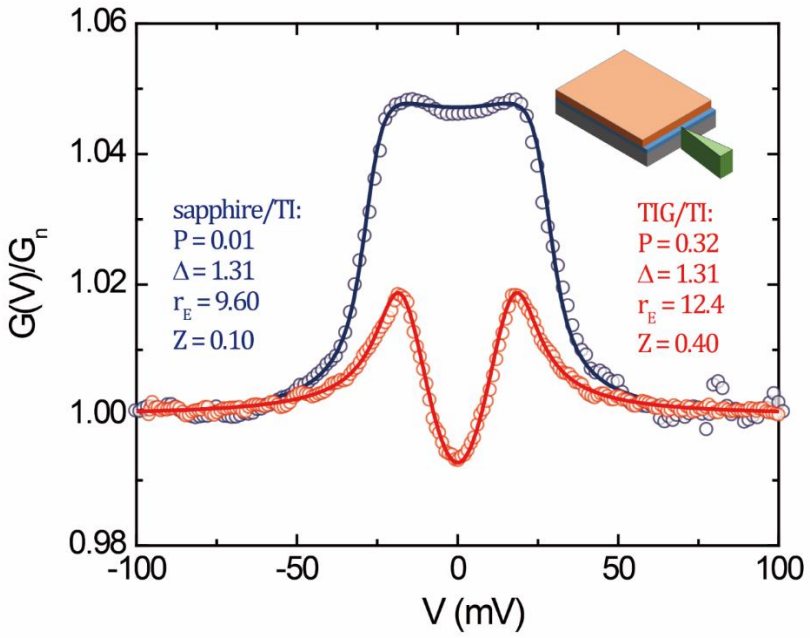

Figure 3-37. Representative Andreev reflection spectra for $(Bi_{0.20}Sb_{0.80})_2Te_3$(20 QL) on TIG and sapphire substrate. Fitting the normalized differential conductance to the modified BTK model yields *P* of 32% for TI on TIG and near-zero *P* for TI on sapphire. All measurements were taken at 1.5 K. The circles are raw data and solid curves are the best fits. The inset is a schematic drawing of PCAR experiments.

A straightforward mechanism for the squared AHE hysteresis loops is induced ferromagnetism due to proximity coupling with TIG. Alternatively, since TI has strong spin-orbit coupling, the spin Hall effect could in principle give rise to similar AHE loops (*58*), and this scenario does not require any induced ferromagnetism in TI. However, it is only the first mechanism that produces the exchange gap relevant to the QAHE. Magnetoresistance measurements can shed some light on the relative importance of the spin Hall effect. We have performed those measurements with both rotating and sweeping magnetic fields and the results point towards the first mechanism (Figure 3-36). However, unambiguously confirming the exact mechanism with magneto-transport

remains a major challenge. To directly verify the existence of induced ferromagnetism in TI surface, we employ point-contact Andreev reflection spectroscopy (PCAR), a well-established probe for quantitatively measuring spin polarization in ferromagnetic materials (*176*, *177*). Since the current only flows in the TI part of the heterostructures, it exclusively detects spin polarization in the TI. To perform the measurements, the heterostructure sample was first cleaved. The superconducting tip then locates and approaches the interface from the cleaved side. Because of a limitation on tip size, the tip-sample contact is across the entire TI thickness, as illustrated by the inset of Figure 3-37. Consequently, both the top and bottom surfaces of the TI layer contribute to the Andreev spectrum. Due to the spin-momentum locking, electrons on both TI surfaces have opposite spins in the film plane; thus, zero spin polarization is expected if both surfaces contribute equally. This is indeed observed in the 20 QL sapphire/TI reference sample, as shown by the dark blue curve in Figure 3-37. An analysis using the modified BTK model (*178*) shows spin polarization (*P*) as small as 1%, which suggests slight asymmetry between two surfaces. In contrast, in TIG/$(Bi_{0.20}Sb_{0.80})_2Te_3$(20 QL), *P* is found to be over 30% with a large interfacial factor or *Z*-factor (*Z* = 0.4), much greater than that in the reference sample. As shown in Figure 3-37, the Andreev peak of the TIG/TI sample is much lower than that of the sapphire/TI, also indicating higher *P*. In PCAR, *P* is often significantly reduced by having a finite interfacial scattering *Z*-factor. The observed *P* of 30% at a large *Z*-factor of 0.4 is therefore underestimated. Due to the difficulty in making transparent side contacts, we are unable to realize low *Z*-factor contacts. However, from several relatively large *Z*-factor contacts, we can extrapolate to

an intrinsic *P* value of 70% at *Z* = 0 (see Figure 3-38), unequivocally demonstrating the induced ferromagnetism in TI surface electronic states.

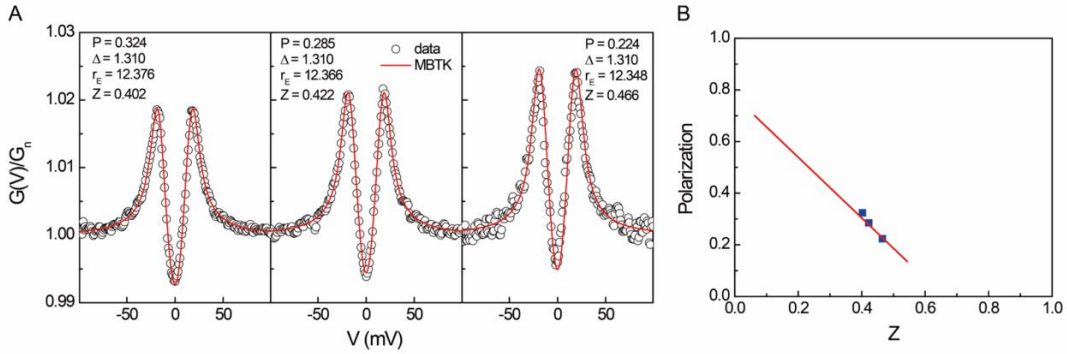

Figure 3-38. A. Representative Andreev reflection spectra for TIG/(Bi_xSb_{1-x})$_2Te_3$ (20 QL) taken at 1.5 K with different *Z*-factors. Black circles are the raw data and red curves are the best fits using the modified BTK model with parameters shown in each panel. B. Spin polarization *P* as a function of the *Z*-factor extracted from the fitting in A. Red dash line is a guide to the eye which extrapolates to ~70% at *Z*=0.

In conclusion, we have demonstrated robust above 400 K proximity-induced ferromagnetism with strong perpendicular magnetic anisotropy in TI surface states of the TIG/TI heterostructures. Similar proximity-induced exchange interaction has been observed in ferromagnet/TI and anti-ferromagnet/TI heterostructures (*162-170*), the effect in our heterostructures extends at much higher temperatures. The proximity approach offers a powerful yet flexible method to tailor both electronic and magnetic properties to realize the QAHE much above room temperatures for potential applications. The TIG/TI heterostructure also provides an ideal platform to explore other topological magneto-electric effects (*156, 179*), such as quantized Faraday and Kerr rotation (*180-182*) and image magnetic monopole (*183*).

3.3.4. Dramatically Modulated Spin Dynamics in YIG by Topological Insulator Surface States

Topological insulators are a new type of quantum matter with unusual spin and charge properties owing to the non-trivial band topology and strong spin-orbit coupling(*184*). These properties can lead to a variety of exotic phenomena including topological magneto-electric effects(*185, 186*), quantum anomalous Hall effect(*10, 11, 187*), image magnetic monopoles(*188*), etc. A remarkable feature that profoundly affects spin and charge transport in TI is that electron spins are locked orthogonally to the momenta in the Dirac surface states(*189, 190*). Experimental consequences of such spin-momentum locking have been observed in spin valves with TI as detector(*191-194*), spin Seebeck effect(*172*), spin pumping(*195-197*) and spin torque ferromagnetic resonance(*198, 199*). Clearly, the strong coupling between electron spin and translational degrees of freedom can be exploited as an efficient way for manipulating spins and vice versa, which is the objective of spintronics.

The devices revealing the aforementioned effects are often constructed from heterostructures containing TI and a magnetic layer which serves as either a spin current source or a detector. The transport properties in the surface metallic states are conveniently measured electrically. In the same heterostructures, the reverse effect, i.e. the effect of the spin-momentum locked surface states on the spin dynamics of the magnetic layer, has not yet been systematically studied. It is known that a thin heavy metal such as Pt or W can cause broadening in FMR linewidth when it is put on a magnetic metal, which is mainly attributed to the spin pumping effect(*200, 201*). However, this broadening is usually insignificant (a few Oe). In this regime, the FMR

linewidth broadening is quantitatively described by the spin-mixing conductance at the interface. In this work, we investigate spin dynamics of YIG, a ferrimagnetic insulator, in heterostructures with $(Bi_xSb_{1-x})_2Te_3$, a TI layer. By systematically tuning the chemical potential through varying Bi composition *x*, we control the relative weight of the surface electrons(*173*). We report a dramatically enhanced (a factor of 15) Gilbert damping constant of YIG when the chemical potential of the TI is tuned to the vicinity of the Dirac point of the surface states. In the meantime, we observe a large increase (~ 80%) in the in-plane anisotropy of the YIG layer. Such strong interaction between the TI surface states with YIG spins may even call the validity of the spin-mixing conductance description into question(*202*).

We choose YIG for the magnetic constituent in our heterostructures for several reasons. First, YIG crystals have an extremely low Gilbert damping constant ($\alpha \sim 3 \times 10^{-5}$), and thus a very narrow FMR linewidth. In high-quality 10 nm thick YIG thin films, α is ~ 10^{-3}, which is at least one order of magnitude lower than that in ferromagnetic metals. Even a small change in FMR linewidth can be easily detected. Second, YIG films are grown at high temperatures (~ 800 ℃) before the TI layers are grown at much lower temperatures (~230 ℃). This growth sequence prevents any serious intermixing at the interface which may occur in samples grown differently. It is well known that less ideal interface can significantly alter the properties of TI surface states. Third, similar to our previous spin Seebeck effect study, here we conduct FMR measurements at room temperature which is below YIG's Curie temperature T_c (~550 K) but well above the T_c

of the induced ferromagnetism in the TI surface(*172*). Consequently, YIG's damping should not be affected by any induced ferromagnetism in TI.

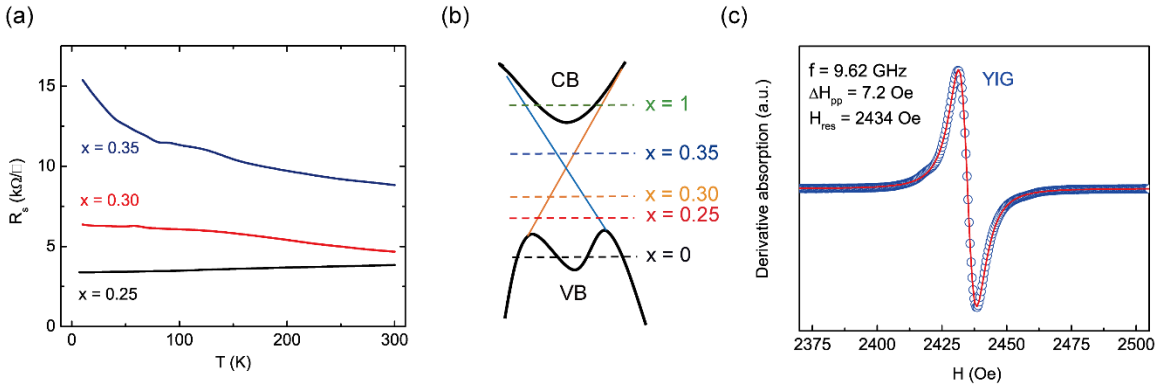

Figure 3-39. Characterization of YIG/TI heterostructures. (a) Temperature dependence of the sheet resistance of three (or five) YIG (10 nm)/5 QL-$(Bi_xSb_{1-x})_2Te_3$ heterostructures. (b) Schematic electronic band structure for five YIG/$(Bi_xSb_{1-x})_2Te_3$ heterostructures. Dashed lines indicate the position of the chemical potential. (c) FMR derivative absorption spectrum of a typical 10 nm thick bare YIG film measured with a frequency of 9.62 GHz.

10 nm thick atomically flat YIG films are grown on (111)-oriented GGG by pulsed laser deposition(*203*) first. 5 QL thick $(Bi_xSb_{1-x})_2Te_3$ films are subsequently grown atop YIG in an ultra-high vacuum molecular epitaxy beam chamber(*172*). Figure 3-39 (a) shows the temperature dependence of the sheet resistance for the three TI samples with different Bi compositions x = 0.25, 0.30 and 0.35. Among five samples including Bi_2Te_3 (x = 1) and Sb_2Te_3 (x = 0), x = 0.35 sample is most insulating as indicated by the largest negative slope due to depletion of bulk carriers at low temperatures, suggesting close proximity of the chemical potential to the Dirac point. With x deviating from 0.35, the chemical potential is tuned away from the Dirac point. In Bi_2Te_3 (x = 1) and Sb_2Te_3 (x = 0), the chemical potential is located in the bulk bands(*173*). As illustrated in Figure 3-39 (a), the resistivity data confirm that the chemical potential of $(Bi_xSb_{1-x})_2Te_3$ are

systematically tuned across the Dirac point by varying Bi composition which was demonstrated previously(*173*).

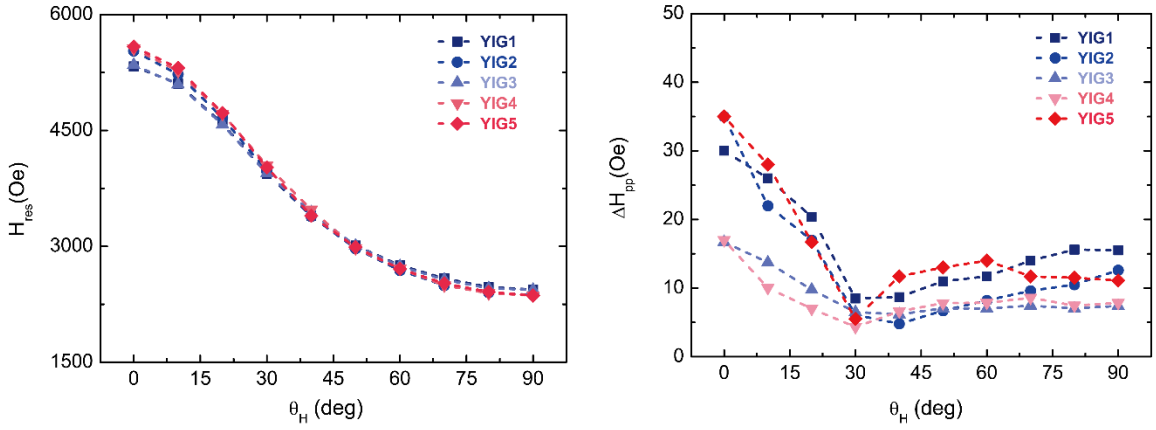

Figure 3-40. FMR properties of five bare YIG samples showing negligible variation in the YIG film qualities. (a) The resonance field of bare YIG films. (b) The polar angle dependent FMR linewidth in bare YIG films.

FMR is a powerful technique for probing spin dynamics in ferromagnets in the frequency domain. We measure FMR spectra with both cavity and broad-brand co-planar waveguide FMR setups. Prior to the deposition of TI layers, cavity FMR measurements are performed on all bare YIG samples at room temperature using a Bruker 9.6 GHz X-band EMX EPR spectrometer. Figure 3-39 (c) shows a FMR spectrum of a typical 10 nm thick bare YIG film with an in-plane magnetic field. The FMR derivative absorption signal shows a single Lorentzian feature with the peak-to-peak linewidth ΔH_{pp} of 7.2 Oe at the resonance field H_{res} = 2434 Oe. The single Lorentzian absorption with such a narrow linewidth indicates high uniformity of the bare YIG films. The average in-plane FMR linewidth ΔH_{pp} and resonance field H_{res} for all five samples used in this experiment are 10.3 ± 2.5 Oe and 2394.2 ± 39.7 Oe, respectively. When FMR is performed with

different polar angles θ_H's (defined below), the θ_H dependence of both quantities for all five bare YIG samples also show very small variations (Figure 3-40), indicating a tight control over the YIG quality. These results serve as the baseline for all bare YIG samples.

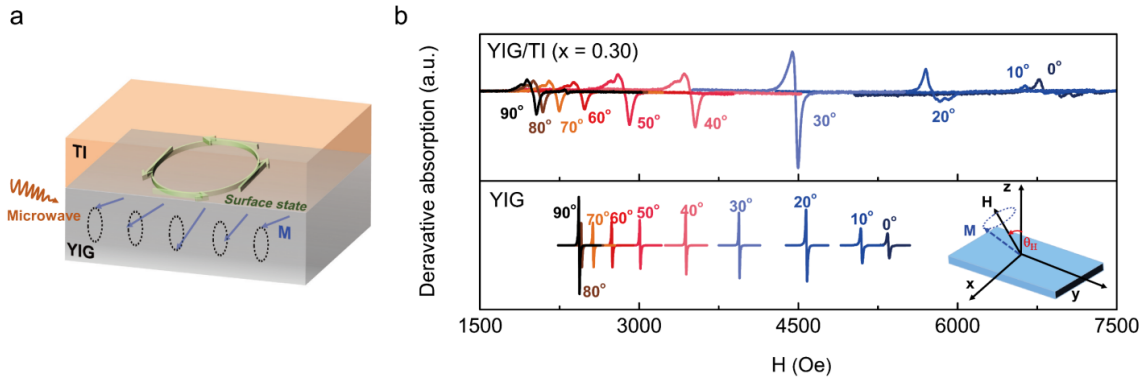

Figure 3-41. The FMR spectrum of YIG and YIG/TI samples. (a) Schematic drawing of magnetization dynamics in YIG interfaced with TI in which the surface state spins are locked with momenta as indicated by the horizontal circle. (b) FMR derivative absorption spectra of YIG/$(Bi_{0.30}Sb_{0.70})_2Te_3$ and bare YIG film at a frequency of 9.62 GHz with the polar angle θ_H ranging from 0˚(out-of-plane) to 90˚ (in-plane) at 300 K. Inset: schematic drawing showing the measurement geometry.

To study the effect of the TI on YIG spin dynamics in YIG/TI heterostructures, we first measure the polar angle dependent FMR. An external static magnetic field is applied at an angle θ_H with respect to the normal direction of the sample (inset of Figure 3-41 (b)). As illustrated in the schematic of Figure 3-41 (a), microwave is sent to initiate magnetization dynamics of the underlying YIG layer. The uniform precession or k=0 spin wave mode is excited at the resonance field to generate a magnon population. In typical bilayer structures, the presence of a heavy metal layer serves as a drain to the spin angular momentum in the magnon reservoir known as spin pumping(*204*). The outward flow of spin continues as a pure electronic spin current in the heavy metal which decays

over the spin diffusion length. This process results in additional damping to the magnetization which can be quantitatively measured by the FMR linewidth increase. In bilayers of YIG/Pt, for example, the FMR linewidth increase due to spin pumping is 10 - 15 Oe at 9.6 GHz. On the other hand, the polar angle dependence of the FMR resonance field H_{res} contains information of magnetic anisotropy in the magnetic materials(*205*). With Pt on YIG, for example, the θ_H dependence of H_{res} only shows a small change which translates to a magnetic anisotropy increase of 5%, consistent with previous studies(*200, 201*).

Detailed derivative absorption spectra as a function of θ_H are shown in Figure 3-41 (b) as the magnetic field H rotates from in-plane (θ_H = 90˚) to out-of-plane orientations (θ_H = 0˚) for a bare YIG film and a YIG/$(Bi_{0.30}Sb_{0.70})_2Te_3$ heterostructure as two representative samples. Obviously, the bare YIG sample has relatively narrow FMR linewidth (data for all five bare YIG samples are displayed in Figure 3-40 (b)). In the meantime, H_{res} decreases monotonically from ~5560 Oe at H out-of-plane to ~ 2389 Oe at H in-plane, consistent with the behaviors of nanometer thick YIG films with in-plane magnetic anisotropy(*58*). Stark contrast becomes immediately clear when the bare YIG results are compared with the counterparts of the YIG/TI sample. After 5 QL TI is grown on top, as shown in top figure of Figure 3-41 (b), two dramatic differences can be readily identified: broadening of the FMR linewidth and shift in resonance field. In YIG/$(Bi_{0.30}Sb_{0.70})_2Te_3$, the linewidth is broadened by one order of magnitude compared with the bare YIG film! In the meantime, the resonance field range is significantly expanded, i.e. 1990 Oe - 6906 Oe. The magnitude of both the linewidth broadening and

the resonance field shift in YIG/TI have not been seen in any bilayers of YIG with a heavy metal, suggesting an extraordinary role of TI.

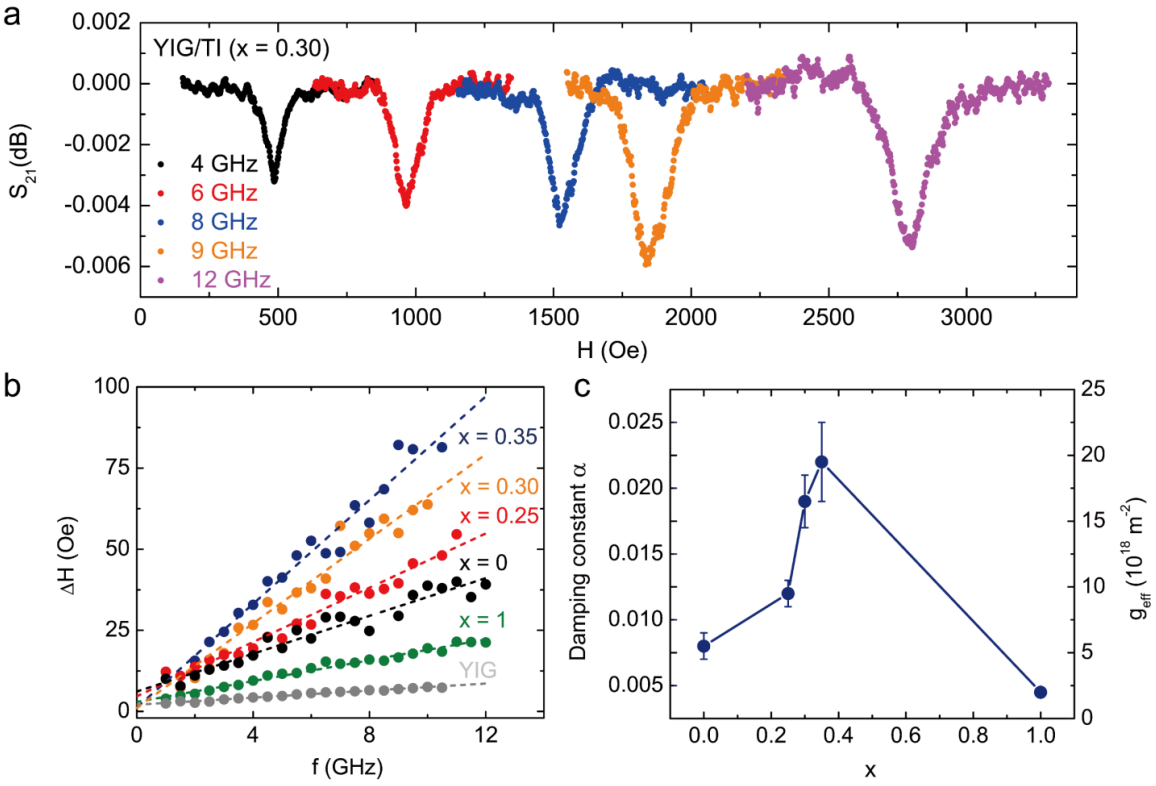

Figure 3-42. The damping characteristic of $(Bi_xSb_{1-x})_2Te_3$ with different Bi doping. (a) FMR absorption spectra S_{21} for YIG/$(Bi_{0.30}Sb_{0.70})_2Te_3$ for different frequencies: 4, 6, 8, 9, 12 GHz at 300 K after background subtraction. (b) Frequency dependence of FMR linewidth for all five YIG/TI samples and the bare YIG film. (c) Bi composition x dependence of the Gilbert damping constant α and effective spin-mixing conductance extracted from the slope of the straight lines in (b).

To extract the Gilbert damping constant, we perform a broad-band FMR using coplanar waveguide setup for all YIG/TI samples. Representative S_{21} data measured by a vector network analyzer-FMR apparatus as shown in Figure 3-42 (a) are the absorption spectra of YIG/$(Bi_{0.30}Sb_{0.70})_2Te_3$ with a few chosen frequencies. The full width at half maximum $\Delta H = \sqrt{3}\Delta H_{pp}/2$ for all samples is extracted by fitting a Lorentzian function to each S_{21} absorption spectrum up to 12 GHz in frequency. ΔH is then plotted in Figure

3-42 (a) for all samples. Clearly, ΔH can be described by Eq. 1 below and the Gilbert damping constant α can be calculated by(*201*)

$$\Delta H = \frac{\alpha f}{\gamma} + \Delta H_0 , \qquad (1)$$

where γ and ΔH_0 are the gyromagnetic ratio and the inhomogeneity linewidth broadening, respectively. Interestingly, α peaks at x = 0.35, i.e. in the most insulating sample. Compared with the two metallic samples with $\alpha = 8.0 \times 10^{-3}$ for x = 0 or Sb_2Te_3 and $\alpha = 4.5 \times 10^{-3}$ for x = 1 or Bi_2Te_3, α in x = 0.35 sample is a factor of 3 - 5 larger, reaching 2.2×10^{-2}. As discussed earlier, α is generally enhanced in YIG/heavy metal due to spin pumping. For the same reason, it is expected that all YIG/TI samples have larger □ than bare YIG films (average value of value of 1.5×10^{-3}), since Bi, Sb, and Te have strong SOC and consequently a large spin pumping effect. Apparently, α in both YIG/Sb_2Te_3 and YIG/Bi_2Te_3 is indeed larger than that of the bare YIG films by at least a factor of 3, so is the YIG/Pt which is about twice larger. However, the three insulating samples in which the chemical potential lies in the bulk band gap even have larger enhancement in α, as summarized in Figure 3-42 (c). If we adopt the standard spin pumping model, the additional damping due to spin pumping is related to the spin-mixing conductance(*204*),

$$\alpha_{sp} = \alpha_{YIG/TI} - \alpha_{YIG} = \frac{g\mu_B}{4\pi M_s} g_{\uparrow\downarrow} \frac{1}{t_{YIG}}, \qquad (2)$$

where g, μ_B, $g_{\uparrow\downarrow}$ and t_{YIG} are the Landé-factor, Bohr magneton, spin-mixing conductance, and the YIG thickness. $g_{\uparrow\downarrow}$ in our YIG/Bi_2Te_3 or YIG/Sb_2Te_3 is consistent with the value reported by H. Wang *et al*. in a similar heterostructure YIG/Bi_2Se_3 on the order of 10^{18} m^{-2}. However, the surface state dominated samples have even larger $g_{\uparrow\downarrow}$ values surpassing

10^{19} m^{-2}, which is nearly an order of magnitude larger than that of the bulk state dominated YIG/TI samples. Such a large deduced spin-mixing conductance itself may call the model into question since the spin ceases to be a good quantum number in the spin-momentum locked TI surface states.

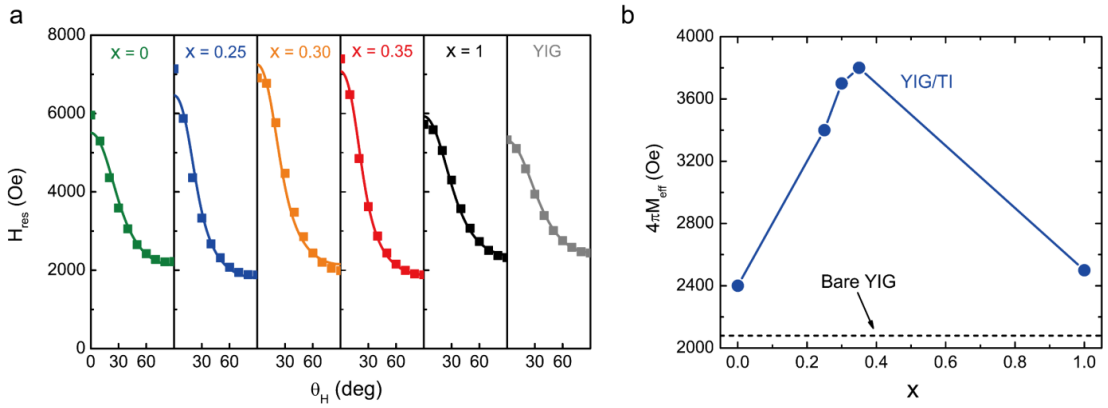

Figure 3-43. The enhancement of the in-plane magnetic anisotropy with the presence of $(Bi_xSb_{1-x})_2Te_3$ on YIG with different Bi doping. (a) Polar angle θ_H dependence of FMR resonance field H_{res} for all five YIG/TI samples and one bare YIG sample. (b) Bi composition dependence of the extracted $4\pi M_{eff}$ for all five YIG/TI samples. The black dash line is the $4\pi M_{eff}$ value for the bare YIG films.

FMR resonance field H_{res} is determined by magnetic anisotropy of the magnetic material. Through angular dependence of H_{res}, the anisotropy field can be quantitatively obtained. Figure 3-43 (a) shows the polar angle θ_H dependence of H_{res} for five YIG/$(Bi_xSb_{1-x})_2Te_3$ samples with different Bi compositions plus one bare YIG sample. In these films, the angular dependence curves can be fitted with a combination of shape anisotropy and a uni-axial anisotropy term which could arise from interfacial and/or crystal-field anisotropy, represented by $4\pi M_{eff} = 4\pi M_s - H_\perp$, where $4\pi M_s$ and $H_\perp$ denote the demagnetizing field and perpendicular magnetic anisotropy field, respectively(*58*,

205). It is known that in YIG the crystal-field anisotropy is much smaller than its shape anisotropy. In addition, YIG has close lattice matching when grown on GGG and therefore the strain-induced interfacial anisotropy is also expected to be very small(*206*). Indeed, $4\pi M_{eff}$ in bare YIG film is found to be 2100 ± 90 Oe, which is clearly dominated by the demagnetizing field $4\pi M_s$. However, upon addition of a 5 QL thick TI layer, $4\pi M_{eff}$ of YIG is increased by 15% and 20% in two metallic YIG/TI samples. In YIG/Pt, the increase is only 5%. More strikingly, $4\pi M_{eff}$ of the most insulating sample (x = 0.35) approaches 3800 Oe which is increased by as much as 80%! We do not expect this dramatic increase to originate from an increased $4\pi M_s$ due to the magnetic proximity effect for two reasons. First, such a proximity effect only occurs at much lower temperatures (< 150 K) as demonstrated by the magneto-transport measurements in YIG/TI(*162*, *194*). Second, the magnetic proximity effect has been shown to be independent of the chemical potential in TI(*162*). However, the increase of $4\pi M_{eff}$ over the bare YIG value is the largest for x = 0.35, 6 times larger than that for x = 0. Therefore, the change in $4\pi M_{eff}$ can only derive from $H_\perp$. $H_\perp$ is negative in all samples, indicating a stronger tendency for the magnetization to remain in the film plane. In the most insulating sample, its magnitude reaches ~1700 Oe. It is interesting to note that the x-dependence in $4\pi M_{eff}$ shows the same trend as the fect damping constant, suggesting a predominant role of the spin-momentum locked surface states.

In summary, we have observed dramatic modifications of YIG spin dynamics by spin-momentum locked surfaces of a thin TI layer in high-quality YIG/TI heterostructures. The strong spin-orbit coupling in TI provides not only a sensitive

detection of the magnetic state in magnetic materials served as a spin current source, but also an active way of manipulating ultrafast magnetization dynamics and preferred magnetization orientation with TI, which has great potential for spintronics.

References:

1. I. Zutic, J. Fabian, S. Das Sarma, Spintronics: Fundamentals and Applications. *Rev. Mod. Phys.* **76**, 323 (2004).

2. S. D. Bader, S. S. P. Parkin, Spintronics. *Annu Rev Conden Ma P* **1**, 71 (2010).

3. Y. Kajiwara *et al.*, Transmission of Electrical Signals by Spin-Wave Interconversion in a Magnetic Insulator. *Nature* **464**, 262 (2010).

4. E. H. Hall, On a New Action of the Magnet on Electric Currents *American Journal of Mathematics* **2**, 287 (1879).

5. K. Vonklitzing, G. Dorda, M. Pepper, New Method for High-Accuracy Determination of the Fine-Structure Constant Based on Quantized Hall Resistance. *Phys. Rev. Lett.* **45**, 494 (1980).

6. K. S. Novoselov *et al.*, Two-Dimensional Gas of Massless Dirac Fermions in Graphene. *Nature* **438**, 197 (2005).

7. Y. B. Zhang, Y. W. Tan, H. L. Stormer, P. Kim, Experimental Observation of the Quantum Hall Effect and Berry's Phase in Graphene. *Nature* **438**, 201 (2005).

8. N. Nagaosa, J. Sinova, S. Onoda, A. H. MacDonald, N. P. Ong, Anomalous Hall Effect. *Rev. Mod. Phys.* **82**, 1539 (2010).

9. F. D. M. Haldane, Model for a Quantum Hall-Effect without Landau-Levels - Condensed-Matter Realization of the Parity Anomaly. *Phys. Rev. Lett.* **61**, 2015 (1988).

10. R. Yu *et al.*, Quantized Anomalous Hall Effect in Magnetic Topological Insulators. *Science* **329**, 61 (2010).

11. C. Z. Chang *et al.*, Experimental Observation of the Quantum Anomalous Hall Effect in a Magnetic Topological Insulator. *Science* **340**, 167 (2013).

12. J. Sinova, S. O. Valenzuela, J. Wunderlich, C. H. Back, T. Jungwirth, Spin Hall Effects. *Rev. Mod. Phys.* **87**, 1213 (2015).

13. M. I. Dyakonov, V. I. Perel, Current-Induced Spin Orientation of Electrons in Semiconductors. *Phys. Lett. A* **A 35**, 459 (1971).

14. Y. K. Kato, R. C. Myers, A. C. Gossard, D. D. Awschalom, Observation of the Spin Hall Effect in Semiconductors. *Science* **306**, 1910 (2004).

15. C. L. Kane, E. J. Mele, Quantum Spin Hall Effect in Graphene. *Phys. Rev. Lett.* **95**, 226801 (2005).

16. M. Konig *et al.*, Quantum Spin Hall Insulator State in Hgte Quantum Wells. *Science* **318**, 766 (2007).

17. B. A. Bernevig, T. L. Hughes, S. C. Zhang, Quantum Spin Hall Effect and Topological Phase Transition in Hgte Quantum Wells. *Science* **314**, 1757 (2006).

18. M. Johnson, R. H. Silsbee, Interfacial Charge-Spin Coupling - Injection and Detection of Spin Magnetization in Metals. *Phys. Rev. Lett.* **55**, 1790 (1985).

19. G. Binasch, P. Grunberg, F. Saurenbach, W. Zinn, Enhanced Magnetoresistance in Layered Magnetic-Structures with Antiferromagnetic Interlayer Exchange. *Phys. Rev. B* **39**, 4828 (1989).

20. M. N. Baibich *et al.*, Giant Magnetoresistance of (001)Fe/(001) Cr Magnetic Superlattices. *Phys. Rev. Lett.* **61**, 2472 (1988).

21. G. E. W. Bauer, E. Saitoh, B. J. van Wees, Spin Caloritronics. *Nat. Mater.* **11**, 391 (2012).

22. K. Uchida *et al.*, Observation of the Spin Seebeck Effect. *Nature* **455**, 778 (2008).

23. C. M. Jaworski *et al.*, Observation of the Spin-Seebeck Effect in a Ferromagnetic Semiconductor. *Nat. Mater.* **9**, 898 (2010).

24. K. Uchida *et al.*, Spin Seebeck Insulator. *Nat. Mater.* **9**, 894 (2010).

25. S. Y. Huang, W. G. Wang, S. F. Lee, J. Kwo, C. L. Chien, Intrinsic Spin-Dependent Thermal Transport. *Phys. Rev. Lett.* **107**, 216604 (2011).

26. S. Y. Huang *et al.*, Transport Magnetic Proximity Effects in Platinum. *Phys. Rev. Lett.* **109**, 107204 (2012).

27. T. Kikkawa *et al.*, Longitudinal Spin Seebeck Effect Free from the Proximity Nernst Effect. *Phys. Rev. Lett.* **110**, 067207 (2013).

28. J. Flipse *et al.*, Observation of the Spin Peltier Effect for Magnetic Insulators. *Phys. Rev. Lett.* **113**, 027601 (2014).

29. S. R. Boona, J. P. Heremans, Magnon Thermal Mean Free Path in Yttrium Iron Garnet. *Phys. Rev. B* **90**, 064421 (2014).

30. H. M. Yu, S. Granville, D. P. Yu, J. P. Ansermet, Evidence for Thermal Spin-Transfer Torque. *Phys. Rev. Lett.* **104**, 146601 (2010).

31. G. M. Choi, C. H. Moon, B. C. Min, K. J. Lee, D. G. Cahill, Thermal Spin-Transfer Torque Driven by the Spin-Dependent Seebeck Effect in Metallic Spin-Valves. *Nat. Phys.* **11**, 576 (2015).

32. H. Meissner, Superconductivity of Contacts with Interposed Barriers. *Phys. Rev.* **117**, 672 (1960).

33. L. Fu, C. L. Kane, Superconducting Proximity Effect and Majorana Fermions at the Surface of a Topological Insulator. *Phys. Rev. Lett.* **100**, 096407 (2008).

34. J. J. Hauser, Magnetic Proximity Effect. *Phys. Rev.* **187**, 580 (1969).

35. W. J. Antel, M. M. Schwickert, T. Lin, W. L. O'Brien, G. R. Harp, Induced Ferromagnetism and Anisotropy of Pt Layers in Fe/Pt(001) Multilayers. *Phys. Rev. B* **60**, 12933 (1999).

36. F. Wilhelm *et al.*, Layer-Resolved Magnetic Moments in Ni/Pt Multilayers. *Phys. Rev. Lett.* **85**, 413 (2000).

37. S. Ruegg *et al.*, Spin-Dependent X-Ray Absorption in Co/Pt Multilayers. *J. Appl. Phys.* **69**, 5655 (1991).

38. Y. S. Hor *et al.*, Development of Ferromagnetism in the Doped Topological Insulator Bi2-Xmnxte3. *Phys. Rev. B* **81**, 195203 (2010).

39. J. S. Zhang *et al.*, Topology-Driven Magnetic Quantum Phase Transition in Topological Insulators. *Science* **339**, 1582 (2013).

40. Z. Wang *et al.*, Strong Interface-Induced Spin-Orbit Interaction in Graphene on Ws2. *Nat. Commun.* **6**, 8339 (2015).

41. B. W. Yang *et al.*, Tunable Spin-Orbit Coupling and Symmetry-Protected Edge States in Graphene/Ws2. *2d Mater* **3**, 031012 (2016).

42. Y. Tserkovnyak, A. Brataas, G. E. W. Bauer, Spin Pumping and Magnetization Dynamics in Metallic Multilayers. *Phys. Rev. B* **66**, 224403 (2002).

43. Y. Y. Sun *et al.*, Damping in Yttrium Iron Garnet Nanoscale Films Capped by Platinum. *Phys. Rev. Lett.* **111**, 106601 (2013).

44. Y. Ohnuma, H. Adachi, E. Saitoh, S. Maekawa, Enhanced Dc Spin Pumping into a Fluctuating Ferromagnet near T-C. *Phys. Rev. B* **89**, 174417 (2014).

45. H. Nakayama *et al.*, Spin Hall Magnetoresistance Induced by a Nonequilibrium Proximity Effect. *Phys. Rev. Lett.* **110**, 206601 (2013).

46. P. Li *et al.*, Spin-Orbit Torque-Assisted Switching in Magnetic Insulator Thin Films with Perpendicular Magnetic Anisotropy. *Nat. Commun.* **7**, 12688 (2016).

47. C. O. Avci *et al.*, Current-Induced Switching in a Magnetic Insulator. *Nat. Mater.*, doi:10.1038/nmat4812 (2016).

48. X. T. Jia, K. Liu, K. Xia, G. E. W. Bauer, Spin Transfer Torque on Magnetic Insulators. *Epl-Europhys Lett* **96**, 17005 (2011).

49. A. Paoletti, Physics of Magnetic Garnets. *Elsevier, Amsterdam*, (1978).

50. C. Tang *et al.*, Exquisite Growth Control and Magnetic Properties of Yttrium Iron Garnet Thin Films. *Appl. Phys. Lett.* **108**, 102403 (2016).

51. M. Aldosary *et al.*, Platinum/Yttrium Iron Garnet Inverted Structures for Spin Current Transport. *Appl. Phys. Lett.* **108**, 242401 (2016).

52. Y. Krockenberger *et al.*, Layer-by-Layer Growth and Magnetic Properties of Y3fe5o12 Thin Films on Gd3ga5o12. *J. Appl. Phys.* **106**, 123911 (2009).

53. A. Ichimiya, Reflection High-Energy Electron Diffraction, Rheed. *J Jpn Soc Tribologis* **50**, 731 (2005).

54. W. Yuan *et al.*, Epitaxial Growth and Properties of La0.7sr0.3mno3 Thin Films with Micrometer Wide Atomic Terraces. *Appl. Phys. Lett.* **107**, 022404 (2015).

55. M. C. Onbasli *et al.*, Pulsed Laser Deposition of Epitaxial Yttrium Iron Garnet Films with Low Gilbert Damping and Bulk-Like Magnetization. *Apl Mater* **2**, 106102 (2014).

56. A. Rosencwaig, W. J. Tabor, F. B. Hagedorn, Vanuiter.Lg, Noncubic Magnetic Anisotropies in Flux-Grown Rare-Earth Iron Garnets. *Phys. Rev. Lett.* **26**, 775 (1971).

57. H. L. Wang, C. H. Du, P. C. Hammel, F. Y. Yang, Strain-Tunable Magnetocrystalline Anisotropy in Epitaxial Y3fe5o12 Thin Films. *Phys. Rev. B* **89**, 134404 (2014).

58. C. Tang *et al.*, Anomalous Hall Hysteresis in $Tm_3fe_5o_{12}$/Pt with Strain-Induced Perpendicular Magnetic Anisotropy. *Phys. Rev. B* **94**, 140403(R) (2016).

59. P. Pirro *et al.*, Spin-Wave Excitation and Propagation in Microstructured Waveguides of Yttrium Iron Garnet/Pt Bilayers. *Appl. Phys. Lett.* **104**, 012402 (2014).

60. J. X. Li *et al.*, Observation of Magnon-Mediated Current Drag in Pt/Yttrium Iron Garnet/Pt(Ta) Trilayers. *Nat. Commun.* **7**, 10858 (2016).

61. M. Duan, A. M. Grishin, K. V. Rao, T. Suzuki, Laser-Deposited Bismuth Doped Iron-Garnet Films with Perpendicular Anisotropy. *IEEE Trans. Magn.* **31**, 3245 (1995).

62. E. Popova *et al.*, Perpendicular Magnetic Anisotropy in Ultrathin Yttrium Iron Garnet Films Prepared by Pulsed Laser Deposition Technique. *Journal of Vacuum Science & Technology a-Vacuum Surfaces and Films* **19**, 2567 (2001).

63. D. M. Heinz, P. J. Besser, J. M. Owens, J. E. Mee, G. R. Pulliam, Mobile Cylindrical Magnetic Domains in Epitaxial Garnet Films. *J. Appl. Phys.* **42**, 1243 (1971).

64. E. Anastassakis, Strained Superlattices and Heterostructures - Elastic Considerations. *J. Appl. Phys.* **68**, 4561 (1990).

65. P. Sellappan, C. Tang, J. Shi, J. E. Garay, An Integrated Approach to Doped Thin Films with Strain-Tunable Magnetic Anisotropy: Powder Synthesis, Target Preparation and Pulsed Laser Deposition of Bi:Yig. *Materials Research Letters* **5**, 41 (2017).

66. S. Geller, J. P. Remeika, R. C. Sherwood, H. J. Williams, G. P. Espinosa, Magnetic Study of the Heavier Rare-Earth Iron Garnets. *Phys. Rev.* **137**, A1034 (1965).

67. T. Miyadai, Ferrimagnetic Resonance in a Single Crystal of Thulium-Iron Garnet - (Tm3fe5o12). *J. Phys. Soc. Jpn.* **17**, 1899 (1962).

68. M. Y. Chern, J. S. Liaw, Study of Bixy3-Xfe5o12 Thin Films Grown by Pulsed Laser Deposition. *Jpn J Appl Phys 1* **36**, 1049 (1997).

69. T. Lin, C. Tang, J. Shi, Induced Magneto-Transport Properties at Palladium/Yttrium Iron Garnet Interface. *Applied Physics Letters* **103**, 132407 (2013).

70. Y. M. Yang *et al.*, Investigation of Magnetic Proximity Effect in Ta/Yig Bilayer Hall Bar Structure. *J. Appl. Phys.* **115**, 17C509 (2014).

71. Y. T. Chen *et al.*, Theory of Spin Hall Magnetoresistance. *Phys. Rev. B* **87**, 144411 (2013).

72. T. Seki *et al.*, Giant Spin Hall Effect in Perpendicularly Spin-Polarized Fept/Au Devices. *Nat. Mater.* **7**, 125 (2008).

73. E. Saitoh, M. Ueda, H. Miyajima, G. Tatara, Conversion of Spin Current into Charge Current at Room Temperature: Inverse Spin-Hall Effect. *Appl. Phys. Lett.* **88**, 182509 (2006).

74. J. Vogel *et al.*, Structure and Magnetism of Pd in Pd/Fe Multilayers Studied by X-Ray Magnetic Circular Dichroism at the Pd L(2,3) Edges. *Phys. Rev. B* **55**, 3663 (1997).

75. G. Y. Guo, Ab Initio Calculation of Intrinsic Spin Hall Conductivity of Pd and Au. *J. Appl. Phys.* **105**, 07C701 (2009).

76. G. Bergmann, Magnetic-Behavior of Fe Atoms on the Surface of Palladium. *Phys. Rev. B* **23**, 3805 (1981).

77. A. J. Manuel, M. McDougald, The Magnetic Properties of Dilute Palladium-Iron Alloys. *Journal of Physics C: Solid State Physics* **3**, 147 (1970).

78. A. Fert, O. Jaoul, Left-Right Asymmetry in the Scattering of Electrons by Magnetic Impurities, and a Hall Effect. *Phys. Rev. Lett.* **28**, 303 (1972).

79. A. Hamzic, S. Senoussi, I. A. Campbell, A. Fert, Orbital Magnetism of Transition-Metal Impurities in Platinum. *J Magn Magn Mater* **15-8**, 921 (1980).

80. A. Hamzic, S. Senoussi, I. A. Campbell, A. Fert, Extraordinary Hall-Effect in Dilute Pd Based Alloys. *Solid State Commun.* **26**, 617 (1978).

81. M. T. Béal-Monod, R. A. Weiner, Field Dependence of the Anomalous Hall Coefficient in Dilute Magnetic Alloys. *Phys. Rev. B* **3**, 3056 (1971).

82. A. Fert, A. Friederich, A. Hamzic, Hall-Effect in Dilute Magnetic-Alloys. *J Magn Magn Mater* **24**, 231 (1981).

83. T. R. Mcguire, R. I. Potter, Anisotropic Magnetoresistance in Ferromagnetic 3d Alloys. *IEEE Trans. Magn.* **11**, 1018 (1975).

84. Y. M. Lu *et al.*, Hybrid Magnetoresistance in the Proximity of a Ferromagnet. *Phys. Rev. B* **87**, 220409 (2013).

85. M. Althammer *et al.*, Quantitative Study of the Spin Hall Magnetoresistance in Ferromagnetic Insulator/Normal Metal Hybrids. *Phys. Rev. B* **87**, 224401 (2013).

86. J. Foros, G. Woltersdorf, B. Heinrich, A. Brataas, Scattering of Spin Current Injected in Pd(001). *J. Appl. Phys.* **97**, 10A714 (2005).

87. V. Vlaminck, J. E. Pearson, S. D. Bader, A. Hoffmann, Dependence of Spin-Pumping Spin Hall Effect Measurements on Layer Thicknesses and Stacking Order. *Phys. Rev. B* **88**, 064414 (2013).

88. H. Kurt, R. Loloee, K. Eid, W. P. Pratt, J. Bass, Spin-Memory Loss at 4.2 K in Sputtered Pd and Pt and at Pd/Cu and Pt/Cu Interfaces. *Appl. Phys. Lett.* **81**, 4787 (2002).

89. T. Lin, C. Tang, H. M. Alyahayaei, J. Shi, Experimental Investigation of the Nature of the Magnetoresistance Effects in Pd-Yig Hybrid Structures. *Phys. Rev. Lett.* **113**, 037203 (2014).

90. S. Meyer *et al.*, Anomalous Hall Effect in Yig Vertical Bar Pt Bilayers. *Appl. Phys. Lett.* **106**, 132402 (2015).

91. N. Vlietstra *et al.*, Exchange Magnetic Field Torques in Yig/Pt Bilayers Observed by the Spin-Hall Magnetoresistance. *Appl. Phys. Lett.* **103**, 032401 (2013).

92. Y. M. Lu *et al.*, Pt Magnetic Polarization on Y3fe5o12 and Magnetotransport Characteristics. *Phys. Rev. Lett.* **110**, 147207 (2013).

93. X. Zhou *et al.*, Magnetotransport in Metal/Insulating-Ferromagnet Heterostructures: Spin Hall Magnetoresistance or Magnetic Proximity Effect. *Phys. Rev. B* **92**, 060402 (2015).

94. Z. L. Jiang *et al.*, A Comparative Transport Study of Bi2se3 and Bi2se3/Yttrium Iron Garnet. *Appl. Phys. Lett.* **104**, 222409 (2014).

95. R. W. Cochrane, J. Destry, M. Trudeau, Sign Reversal of the Hall-Coefficient in Amorphous Ni-Zr Alloys. *Phys. Rev. B* **27**, 5955 (1983).

96. B. L. Gallagher, D. Greig, M. A. Howson, A. A. M. Croxon, The Positive Hall-Coefficients of Amorphous Transition-Metal Alloys. *J Phys F Met Phys* **13**, 119 (1983).

97. G. E. Bauer, E. Saitoh, B. J. van Wees, Spin Caloritronics. *Nature materials* **11**, 391 (2012).

98. A. V. Chumak, V. I. Vasyuchka, A. A. Serga, B. Hillebrands, Magnon Spintronics. *Nature Physics* **11**, 453 (2015).

99. I. M. Miron *et al.*, Perpendicular Switching of a Single Ferromagnetic Layer Induced by in-Plane Current Injection. *Nature* **476**, 189 (2011).

100. L. Liu *et al.*, Spin-Torque Switching with the Giant Spin Hall Effect of Tantalum. *Science* **336**, 555 (2012).

101. L. Liu, O. J. Lee, T. J. Gudmundsen, D. C. Ralph, R. A. Buhrman, Current-Induced Switching of Perpendicularly Magnetized Magnetic Layers Using Spin Torque from the Spin Hall Effect. *Physical review letters* **109**, (2012).

102. G. Yu *et al.*, Switching of Perpendicular Magnetization by Spin-Orbit Torques in the Absence of External Magnetic Fields. *Nature nanotechnology* **9**, 548 (2014).

103. X. Qiu *et al.*, Spin-Orbit-Torque Engineering Via Oxygen Manipulation. *Nature nanotechnology* **10**, 333 (2015).

104. K. Ando *et al.*, Electric Manipulation of Spin Relaxation Using the Spin Hall Effect. *Physical review letters* **101**, (2008).

105. M. Althammer *et al.*, Quantitative Study of the Spin Hall Magnetoresistance in Ferromagnetic Insulator/Normal Metal Hybrids. *Physical Review B* **87**, (2013).

106. Y.-T. Chen *et al.*, Theory of Spin Hall Magnetoresistance. *Physical Review B* **87**, (2013).

107. C. Hahn *et al.*, Comparative Measurements of Inverse Spin Hall Effects and Magnetoresistance in Yig/Pt and Yig/Ta. *Physical Review B* **87**, (2013).

108. C. Tang *et al.*, Anomalous Hall Hysteresis Intm3fe5o12/Ptwith Strain-Induced Perpendicular Magnetic Anisotropy. *Physical Review B* **94**, (2016).

109. M. Schreier *et al.*, Current-Induced Spin Torque Resonance of a Magnetic Insulator. *Physical Review B* **92**, (2015).

110. J. Sklenar *et al.*, Driving and Detecting Ferromagnetic Resonance in Insulators with the Spin Hall Effect. *Physical Review B* **92**, (2015).

111. P. Li *et al.*, Spin-Orbit Torque-Assisted Switching in Magnetic Insulator Thin Films with Perpendicular Magnetic Anisotropy. *Nat Commun* **7**, 12688 (2016).

112. C. O. Avci *et al.*, Current-Induced Switching in a Magnetic Insulator. *Nature materials*, (2016).

113. W. Zhang, W. Han, X. Jiang, S.-H. Yang, S. S. P. Parkin, Role of Transparency of Platinum–Ferromagnet Interfaces in Determining the Intrinsic Magnitude of the Spin Hall Effect. *Nature Physics* **11**, 496 (2015).

114. C.-F. Pai, Y. Ou, L. H. Vilela-Leão, D. C. Ralph, R. A. Buhrman, Dependence of the Efficiency of Spin Hall Torque on the Transparency of Pt/Ferromagnetic Layer Interfaces. *Physical Review B* **92**, (2015).

115. C.-F. Pai *et al.*, Spin Transfer Torque Devices Utilizing the Giant Spin Hall Effect of Tungsten. *Appl Phys Lett* **101**, 122404 (2012).

116. J. C. Rojas-Sanchez *et al.*, Spin Pumping and Inverse Spin Hall Effect in Platinum: The Essential Role of Spin-Memory Loss at Metallic Interfaces. *Physical review letters* **112**, 106602 (2014).

117. S. A. Bender, Y. Tserkovnyak, Interfacial Spin and Heat Transfer between Metals and Magnetic Insulators. *Physical Review B* **91**, (2015).

118. Y. Ohnuma, H. Adachi, E. Saitoh, S. Maekawa, Enhanced Dc Spin Pumping into a Fluctuating Ferromagnet Neartc. *Physical Review B* **89**, (2014).

119. R. Zhang, R. F. Willis, Thickness-Dependent Curie Temperatures of Ultrathin Magnetic Films: Effect of the Range of Spin-Spin Interactions. *Physical review letters* **86**, 2665 (2001).

120. A. Paoletti, *Physics of Magnetic Garnets*. (1978).

121. K. Garello *et al.*, Symmetry and Magnitude of Spin-Orbit Torques in Ferromagnetic Heterostructures. *Nature nanotechnology* **8**, 587 (2013).

122. C. O. Avci *et al.*, Interplay of Spin-Orbit Torque and Thermoelectric Effects in Ferromagnet/Normal-Metal Bilayers. *Physical Review B* **90**, (2014).

123. J. Kim *et al.*, Layer Thickness Dependence of the Current-Induced Effective Field Vector in Ta|Cofeb|Mgo. *Nature materials* **12**, 240 (2013).

124. Q. Shao *et al.*, Strong Rashba-Edelstein Effect-Induced Spin-Orbit Torques in Monolayer Transition Metal Dichalcogenide/Ferromagnet Bilayers. *Nano letters* **16**, 7514 (2016).

125. K.-i. Uchida *et al.*, Observation of Longitudinal Spin-Seebeck Effect in Magnetic Insulators. *Appl Phys Lett* **97**, 172505 (2010).

126. X. Jia, K. Liu, K. Xia, G. E. W. Bauer, Spin Transfer Torque on Magnetic Insulators. *EPL (Europhysics Letters)* **96**, 17005 (2011).

127. A. Manchon, H. C. Koo, J. Nitta, S. M. Frolov, R. A. Duine, New Perspectives for Rashba Spin-Orbit Coupling. *Nature materials* **14**, 871 (2015).

128. A. Soumyanarayanan, N. Reyren, A. Fert, C. Panagopoulos, Emergent Phenomena Induced by Spin-Orbit Coupling at Surfaces and Interfaces. *Nature* **539**, 509 (2016).

129. V. L. Grigoryan, W. Guo, G. E. W. Bauer, J. Xiao, Intrinsic Magnetoresistance in Metal Films on Ferromagnetic Insulators. *Physical Review B* **90**, (2014).

130. M. Q. Sui *et al.*, Gate-Tunable Topological Valley Transport in Bilayer Graphene. *Nat. Phys.* **11**, 1027 (2015).

131. H. Nakayama *et al.*, Rashba-Edelstein Magnetoresistance in Metallic Heterostructures. *Physical review letters* **117**, 116602 (2016).

132. D. Pesin, A. H. MacDonald, Spintronics and Pseudospintronics in Graphene and Topological Insulators. *Nat. Mater.* **11**, 409 (2012).

133. A. K. Geim, K. S. Novoselov, The Rise of Graphene. *Nat. Mater.* **6**, 183 (2007).

134. C. R. Dean *et al.*, Boron Nitride Substrates for High-Quality Graphene Electronics. *Nat. Nanotechnol.* **5**, 722 (2010).

135. X. L. Qi, S. C. Zhang, Topological Insulators and Superconductors. *Rev. Mod. Phys.* **83**, 1057 (2011).

136. J. Balakrishnan, G. K. W. Koon, M. Jaiswal, A. H. C. Neto, B. Ozyilmaz, Colossal Enhancement of Spin-Orbit Coupling in Weakly Hydrogenated Graphene. *Nat. Phys.* **9**, 284 (2013).

137. Y.-W. Son, M. L. Cohen, S. G. Louie, Half-Metallic Graphene Nanoribbons. *Nature* **444**, 347 (2006).

138. J.-H. Chen, L. Li, W. G. Cullen, E. D. Williams, M. S. Fuhrer, Tunable Kondo Effect in Graphene with Defects. *Nat Phys* **7**, 535 (2011).

139. B. Uchoa, V. N. Kotov, N. M. R. Peres, A. H. Castro Neto, Localized Magnetic States in Graphene. *Physical Review Letters* **101**, 026805 (2008).

140. T. Dietl, A Ten-Year Perspective on Dilute Magnetic Semiconductors and Oxides. *Nat Mater* **9**, 965 (2010).

141. R. Sachs, Z. Lin, P. Odenthal, R. Kawakami, J. Shi, Direct Comparison of Graphene Devices before and after Transfer to Different Substrates. *Applied Physics Letters* **104**, 033103 (2014).

142. R. Sachs, Z. Lin, J. Shi, Ferroelectric-Like $Srtio_3$ Surface Dipoles Probed by Graphene. *Sci. Rep.* **4**, 3657 (2014).

143. C. R. Dean *et al.*, Boron Nitride Substrates for High-Quality Graphene Electronics. *Nat Nano* **5**, 722 (2010).

144. A. C. Ferrari *et al.*, Raman Spectrum of Graphene and Graphene Layers. *Physical Review Letters* **97**, 187401 (2006).

145. F. D. M. Haldane, Model for a Quantum Hall Effect without Landau Levels: Condensed-Matter Realization of the "Parity Anomaly". *Physical Review Letters* **61**, 2015 (1988).

146. S. Konschuh, M. Gmitra, J. Fabian, Tight-Binding Theory of the Spin-Orbit Coupling in Graphene. *Physical Review B* **82**, 245412 (2010).

147. D. Xiao, W. Yao, Q. Niu, Valley-Contrasting Physics in Graphene: Magnetic Moment and Topological Transport. *Physical Review Letters* **99**, 236809 (2007).

148. Y. S. Dedkov, M. Fonin, U. Rüdiger, C. Laubschat, Rashba Effect in the Graphene/Ni(111) System. *Physical Review Letters* **100**, 107602 (2008).

149. J. Balakrishnan, G. Kok Wai Koon, M. Jaiswal, A. H. Castro Neto, B. Ozyilmaz, Colossal Enhancement of Spin-Orbit Coupling in Weakly Hydrogenated Graphene. *Nat Phys* **9**, 284 (2013).

150. Z. Qiao *et al.*, Quantum Anomalous Hall Effect in Graphene from Rashba and Exchange Effects. *Physical Review B* **82**, 161414 (2010).

151. Z. Qiao *et al.*, Quantum Anomalous Hall Effect in Graphene Proximity Coupled to an Antiferromagnetic Insulator. *Physical Review Letters* **112**, 116404 (2014).

152. K. Nomura, A. H. MacDonald, Quantum Transport of Massless Dirac Fermions. *Physical Review Letters* **98**, 076602 (2007).

153. L. Wang *et al.*, One-Dimensional Electrical Contact to a Two-Dimensional Material. *Science* **342**, 614 (2013).

154. C. Z. Chang *et al.*, High-Precision Realization of Robust Quantum Anomalous Hall State in a Hard Ferromagnetic Topological Insulator. *Nat. Mater.* **14**, 473 (2015).

155. R. X. Zhang, H. C. Hsu, C. X. Liu, Electrically Tunable Spin Polarization of Chiral Edge Modes in a Quantum Anomalous Hall Insulator. *Phys. Rev. B* **93**, 235315 (2016).

156. X. L. Qi, T. L. Hughes, S. C. Zhang, Topological Field Theory of Time-Reversal Invariant Insulators. *Phys. Rev. B* **78**, 195424 (2008).

157. Y. S. Hor *et al.*, Development of Ferromagnetism in the Doped Topological Insulator $Bi_{2-X}mn_xte_3$. *Phys. Rev. B* **81**, 195203 (2010).

158. M. Mogi *et al.*, Magnetic Modulation Doping in Topological Insulators toward Higher-Temperature Quantum Anomalous Hall Effect. *Appl. Phys. Lett.* **107**, 182401 (2015).

159. J. G. Checkelsky *et al.*, Trajectory of the Anomalous Hall Effect Towards the Quantized State in a Ferromagnetic Topological Insulator. *Nat. Phys.* **10**, 731 (2014).

160. X. F. Kou *et al.*, Metal-to-Insulator Switching in Quantum Anomalous Hall States. *Nat. Commun.* **6**, 8474 (2015).

161. T. Dietl, H. Ohno, Dilute Ferromagnetic Semiconductors: Physics and Spintronic Structures. *Rev. Mod. Phys.* **86**, 187 (2014).

162. Z. L. Jiang *et al.*, Independent Tuning of Electronic Properties and Induced Ferromagnetism in Topological Insulators with Heterostructure Approach. *Nano Lett.* **15**, 5835 (2015).

163. M. D. Li *et al.*, Proximity-Driven Enhanced Magnetic Order at Ferromagnetic-Insulator-Magnetic-Topological-Insulator Interface. *Phys. Rev. Lett.* **115**, 087201 (2015).

164. C. Lee, F. Katmis, P. Jarillo-Herrero, J. S. Moodera, N. Gedik, Direct Measurement of Proximity-Induced Magnetism at the Interface between a Topological Insulator and a Ferromagnet. *Nat. Commun.* **7**, 12014 (2016).

165. F. Katmis *et al.*, A High-Temperature Ferromagnetic Topological Insulating Phase by Proximity Coupling. *Nature* **533**, 513 (2016).

166. P. Wei *et al.*, Exchange-Coupling-Induced Symmetry Breaking in Topological Insulators. *Phys. Rev. Lett.* **110**, 186807 (2013).

167. Z. L. Jiang *et al.*, Structural and Proximity-Induced Ferromagnetic Properties of Topological Insulator-Magnetic Insulator Heterostructures. *Aip Adv.* **6**, 055809 (2016).

168. M. R. Lang *et al.*, Proximity Induced High-Temperature Magnetic Order in Topological Insulator - Ferrimagnetic Insulator Heterostructure. *Nano Lett.* **14**, 3459 (2014).

169. W. Q. Liu *et al.*, Enhancing Magnetic Ordering in Cr-Doped Bi2se3 Using High-T-C Ferrimagnetic Insulator. *Nano Lett.* **15**, 764 (2015).

170. Q. L. He *et al.*, Tailoring Exchange Couplings in Magnetic Topological-Insulator/Antiferromagnet Heterostructures. *Nat. Mater.* **16**, 94 (2017).

171. X. Liu, H. C. Hsu, C. X. Liu, In-Plane Magnetization-Induced Quantum Anomalous Hall Effect. *Phys. Rev. Lett.* **111**, 086802 (2013).

172. Z. L. Jiang *et al.*, Enhanced Spin Seebeck Effect Signal Due to Spin-Momentum Locked Topological Surface States. *Nat. Commun.* **7**, 11458 (2016).

173. J. S. Zhang *et al.*, Band Structure Engineering in (Bi1-Xsbx)(2)Te-3 Ternary Topological Insulators. *Nat. Commun.* **2**, 574 (2011).

174. N. Nagaosa, J. Sinova, S. Onoda, A. H. MacDonald, N. P. Ong, Anomalous Hall Effect. *Rev. Mod. Phys.* **82**, 1539 (2010).

175. S. Iida, Magnetostriction Constants of Rare Earth Iron Garnets. *J. Phys. Soc. Jpn.* **22**, 1201 (1967).

176. R. J. Soulen *et al.*, Measuring the Spin Polarization of a Metal with a Superconducting Point Contact. *Science* **282**, 85 (1998).

177. L. Wang *et al.*, $Co_{1-X}fe_xS_2$: A Tunable Source of Highly Spin-Polarized Electrons. *Phys. Rev. Lett.* **94**, 056602 (2005).

178. T. Y. Chen, S. X. Huang, C. L. Chien, Pronounced Effects of Additional Resistance in Andreev Reflection Spectroscopy. *Phys. Rev. B* **81**, 214444 (2010).

179. A. M. Essin, J. E. Moore, D. Vanderbilt, Magnetoelectric Polarizability and Axion Electrodynamics in Crystalline Insulators. *Phys. Rev. Lett.* **102**, 146805 (2009).

180. L. Wu *et al.*, Quantized Faraday and Kerr Rotation and Axion Electrodynamics of a 3d Topological Insulator. *Science* **354**, 1124 (2016).

181. W. K. Tse, A. H. MacDonald, Giant Magneto-Optical Kerr Effect and Universal Faraday Effect in Thin-Film Topological Insulators. *Phys. Rev. Lett.* **105**, 057401 (2010).

182. J. Maciejko, X. L. Qi, H. D. Drew, S. C. Zhang, Topological Quantization in Units of the Fine Structure Constant. *Phys. Rev. Lett.* **105**, 166803 (2010).

183. X. L. Qi, R. D. Li, J. D. Zang, S. C. Zhang, Inducing a Magnetic Monopole with Topological Surface States. *Science* **323**, 1184 (2009).

184. X. L. Qi, S. C. Zhang, Topological Insulators and Superconductors. *Rev. Mod. Phys.* **83**, 1057 (2011).

185. X. L. Qi, T. L. Hughes, S. C. Zhang, Topological Field Theory of Time-Reversal Invariant Insulators. *Phys. Rev. B* **78**, 195424 (2008).

186. A. M. Essin, J. E. Moore, D. Vanderbilt, Magnetoelectric Polarizability and Axion Electrodynamics in Crystalline Insulators. *Phys. Rev. Lett.* **102**, 146805 (2009).

187. C. Z. Chang *et al.*, High-Precision Realization of Robust Quantum Anomalous Hall State in a Hard Ferromagnetic Topological Insulator. *Nat. Mater.* **14**, 473 (2015).

188. X. L. Qi, R. D. Li, J. D. Zang, S. C. Zhang, Inducing a Magnetic Monopole with Topological Surface States. *Science* **323**, 1184 (2009).

189. D. Hsieh *et al.*, A Tunable Topological Insulator in the Spin Helical Dirac Transport Regime. *Nature* **460**, 1101 (2009).

190. Z. H. Pan *et al.*, Electronic Structure of the Topological Insulator Bi2se3 Using Angle-Resolved Photoemission Spectroscopy: Evidence for a Nearly Full Surface Spin Polarization. *Phys. Rev. Lett.* **106**, 257004 (2011).

191. C. H. Li *et al.*, Electrical Detection of Charge-Current-Induced Spin Polarization Due to Spin-Momentum Locking in Bi2se3. *Nat. Nanotechnol.* **9**, 218 (2014).

192. L. Q. Liu *et al.*, Spin-Polarized Tunneling Study of Spin-Momentum Locking in Topological Insulators. *Phys. Rev. B* **91**, 235437 (2015).

193. Y. B. Fan *et al.*, Electric-Field Control of Spin-Orbit Torque in a Magnetically Doped Topological Insulator. *Nat. Nanotechnol.* **11**, 352 (2016).

194. Z. L. Jiang *et al.*, Enhanced Spin Seebeck Effect Signal Due to Spin-Momentum Locked Topological Surface States. *Nat. Commun.* **7**, 11458 (2016).

195. Y. Shiomi *et al.*, Spin-Electricity Conversion Induced by Spin Injection into Topological Insulators. *Phys. Rev. Lett.* **113**, 196601 (2014).

196. M. Jamali *et al.*, Giant Spin Pumping and Inverse Spin Hall Effect in the Presence of Surface and Bulk Spin-Orbit Coupling of Topological Insulator Bi2se3. *Nano Lett.* **15**, 7126 (2015).

197. H. L. Wang *et al.*, Surface-State-Dominated Spin-Charge Current Conversion in Topological-Insulator-Ferromagnetic-Insulator Heterostructures. *Phys. Rev. Lett.* **117**, 076601 (2016).

198. Y. B. Fan *et al.*, Magnetization Switching through Giant Spin-Orbit Torque in a Magnetically Doped Topological Insulator Heterostructure. *Nat. Mater.* **13**, 699 (2014).

199. A. R. Mellnik *et al.*, Spin-Transfer Torque Generated by a Topological Insulator. *Nature* **511**, 449 (2014).

200. Y. Y. Sun *et al.*, Damping in Yttrium Iron Garnet Nanoscale Films Capped by Platinum. *Phys. Rev. Lett.* **111**, 106601 (2013).

201. K. Kondou *et al.*, Fermi-Level-Dependent Charge-to-Spin Current Conversion by Dirac Surface States of Topological Insulators. *Nat. Phys.* **12**, 1027 (2016).

202. C. H. Du, H. L. Wang, F. Y. Yang, P. C. Hammel, Enhancement of Pure Spin Currents in Spin Pumping Y3fe5o12/Cu/Metal Trilayers through Spin Conductance Matching. *Phys. Rev. Applied* **1**, 044004 (2014).

203. D. Pesin, A. H. MacDonald, Spintronics and Pseudospintronics in Graphene and Topological Insulators. *Nat. Mater.* **11**, 409 (2012).

204. C. Tang *et al.*, Exquisite Growth Control and Magnetic Properties of Yttrium Iron Garnet Thin Films. *Appl. Phys. Lett.* **108**, 102403 (2016).

205. Y. Tserkovnyak, A. Brataas, G. E. W. Bauer, Spin Pumping and Magnetization Dynamics in Metallic Multilayers. *Phys. Rev. B* **66**, 224403 (2002).

206. X. Liu *et al.*, Perpendicular Magnetization Reversal, Magnetic Anisotropy, Multistep Spin Switching, and Domain Nucleation and Expansion in Ga1-Xmnxas Films. *J. Appl. Phys.* **98**, 063904 (2005).